Double Photoionization of Water and Dissociative Electron Attachment to CF_4

by

Dylan Reedy

A dissertation submitted to the Graduate Faculty of
Auburn University
in partial fulfillment of the
requirements for the Degree of
Doctor of Philosophy

Auburn, Alabama
December 10, 2016

Keywords: Photodissociation, Dissociative Electron Attachment

Copyright 2016 by Dylan Reedy

Approved by

Dr. Allen L Landers, Howard Carr Professor of Physics, Experimental AMO Physics
Dr. Mike Fogle, Associate Professor of Physics, Experimental AMO Physics
Dr. Dave Maurer, Associate Professor of Physics, Experimental Plasma Physics
Dr. Konrad Patkowski, Associate Professor of Chemistry and Biochemistry, Physical Chemistry

Abstract

This thesis is an amalgam of two largely different experiments. While the experimental apparatus are similar, the incident particles, fundamental interactions, and dissociation dynamics of the two systems are entirely different. They are tied together via momentum spectroscopy, occasionally called the "momentum microscope". The two experiments each represent a fundamental pillar of the modern scientific regime. For one, it is an observational first, producing an experiment that no other research group has produced before. For the other, it is a check on reproducibility, an effort by the scientific community to validate its efforts.

0.1 Water Experiment

The first of the two experiments included in this thesis is the double photoionization of water by 57 eV linearly polarized photons. A 57 eV photon collides with a water molecule and excites two molecular bonding electrons into the continuum. The remaining dication, H_2O^{2+}, is generally considered unstable and has not been observed in the laboratory. The unstable dication breaks apart, according to the multi-dimensional potential energy surface(s) available to it. The momentum for each of the charged particles - two protons and two electrons - are measured in coincidence. The measurement of the two protons allows for the full orientation of the water molecule prior to dissociation. Prior to the writing of this thesis, this has only

been achieved in a ”recoil axis” frame, aligning two fragments of a complex molecule that breaks apart upon one bond, including the simplest case of a diatomic molecule. The full three dimensional momentum resolution of the entire molecule, and its photoelectrons, is new terrain in momentum spectroscopy. The energies of the recoil ions and electrons, as well as their angular distributions, are measured and analyzed in an attempt to match the repulsive dication states of the water molecule to the asymptotic fragment configurations in both two- and three-body reaction pathways.

The water experiment was conducted at the ALS with other members of the COLTRIMS collaboration from Kansas State University, University of Frankfurt, and Auburn University. The data was given to the author of this thesis as a training exercise in data analysis - training on the actual acquisition of data using COLTRIMS came later, in the second experiment of this thesis.

The details of the experimental apparatus, the excitation of the dication, and its subsequent decay are the focus of the first two chapters of this thesis.

0.2 $\mathbf{CF_4}$ Experiment

The second experiment is dissociative electron attachment to CF_4. Electron attachment is an electron scattering interaction wherein a low energy electron, typically from 0-15 eV in energy, collides with a molecule and is trapped in a local potential minimum, a so-called Shape Resonance. Alternately, the electron can collide with the molecule and couple with some internal degree of freedom, forming a negative ion, a so-called Feshbach Resonance. These thesis chapters focus on the situation in which the electron attachment leads to a dissociative negative ion state, with incident electron energies ranging from 5.5 eV to 9 eV. The angular distributions found match, at least qualitatively, those of previous experiments, although the precise partial wave analysis of those distributions disagree slightly with the literature. The most interesting data, those taken as the primary motivation for the experiment, are the KER measured as a function of the incident electron energy for the reaction pathway leading to CF_3^-. These results disagree with the most recent results in the literature which, on their own, disagreed with all the previous results in measurement of this quantity.

The maintenance, repair, and troubleshooting of a COLTRIMS experiment are rigorous endeavors, and the CF_4 experiment gave the author of this dissertation the opportunity to learn the minutiae of the complex experimental procedure. This process took place, chronologically speaking, well after the analysis of the water experiment was under way. While this ordering of training may initially appear backwards, it was an invaluable layering of technical training, granting the author many opportunities to revisit the skills required as a physicist, from deep literature searches to vacuum pump maintenance to data analysis.

Acknowledgments

There are an impossibly large number of people that deserve thanks for their help, guidance, and patience leading up to the writing of this thesis. As an unfortunate consequence of how many people deserve recognition, this list may well be incomplete. For anyone who deserves my thanks for their help that did not make this list: I apologize for my lousy memory, and thank you for your assistance, whatever the form!

Allen L. Landers, Mike Fogle, Joshua B. Williams, C. William McCurdy, Thomas N. Rescigno, Frank Yip, Averell Gatton, Markus Schoeffler, Thorsten Weber, Dave Maurer, Konrad Patkowski, Chris Rodger, Zachary Streeter, J.A. Edmunds, Ahmed Nemer, Ricky Strom, James Sartor, Spencer LeBlanc, Jonathan Pearce

Table of Contents

List of Figures

List of Tables

Chapter 1

Water Experiment - Apparatus and Motivation

1.1 Overview

Despite its long history, investigation of molecular decay dynamics is as rich and rewarding as ever. The difficulty in this field of research can be traced to both experimental and theoretical complexity. Due to the almost entirely unsolvable equations that most accurately describe molecular systems, theoretical treatments of molecules have long been bottlenecked by the effectiveness of numerical techniques. These techniques, in turn, are bottlenecked by how efficiently analysis algorithms can be implemented in computers. On the other hand, experiments measuring molecular breakup can be be best described using typical experimentalist jargon: they are "really hard." Not until the 1990's did experimental techniques advance enough to collect the entire 4π solid angle of molecular fragments, the analysis of which itself is exceedingly complex. The necessity of timing electronics, coincidence measurements, and the presence of unmeasureable neutral fragments all add to the difficulty of measuring molecular decay dynamics.

1.2 An Introduction to Photoionization

Modern scientific endeavors are heaped with highly specialized techniques and theories due to their ever increasing complexities. Any attempt to discuss advanced research topics must walk a fine line: on one hand, an accurate representation of the physical system is crucial to understanding; on the other, the language used to describe fundamental scientific endeavors is unlikely to be known to external readers, even ones with proximal fields of study. The goal of this section is to familiarize readers with some of the basic concepts to be discussed regarding the water experiment of this thesis.

1.2.1 Franck-Condon Principle

The Franck-Condon principle is a staple of spectroscopy and quantum chemistry. It is a rule that governs the intensity of vibronic transitions in molecules, e.g., the changes of electronic and vibrational energies due to the absorption of a photon. The principle states, qualitatively, that electronic transitions are most likely to occur without changes in the positions of the nuclei. A classical, or at least quasi-classical, justification of this rule is that electrons move significantly more quickly than nuclei and therefore their transitions happen long before the simultaneous vibrational transitions have an opportunity to move the nuclei. From a quantum mechanical standpoint, the principle states that a transition is more likely to happen when the initial and final vibrational wave functions overlap more significantly. The excitation of a neutral molecule from its ground state to a cationic state will most often occur with a transition to a state with a strongly overlapping wavefunction, with no preference for transition to cation ground states. A transition of this kind, wherein the nuclear coordinates are assumed to be fixed, is often called a Franck-Condon transition, or a vertical transition. The region of the potential energy curves involved in the transition, or the fixed nuclear frame for the transition generally, is called the Franck-Condon region.

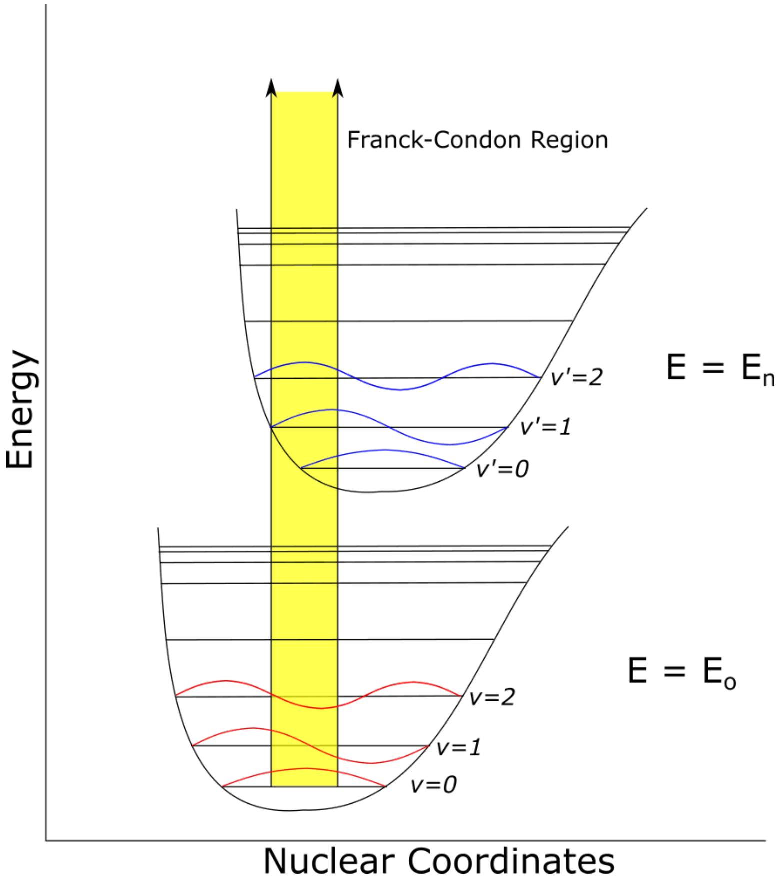

Figure 1.1: Illustration of a Franck-Condon (vertical) transition. According to the Franck-Condon principle, the $\nu = 0 \rightarrow \nu^{'} = 2$ transition is the most probable.

1.2.2 Ionization Threshold

The ionization threshold of a molecule is the energy required to remove an electron entirely from that parent molecule. There is ambiguity involved, however. The photon energy required to ionize a molecule directly is typically *larger* than the calculable energy difference between the neutral molecule in its ground state and the ionized molecular fragments. This disconnect can be attributed in part to the Franck-Condon principle. The likeliest vibronic transitions between molecular states correspond to vertical ones, i.e., transitions where the molecular nuclei do not move. Molecular ions do not possess the same nuclear geometry as their neutral cousins due to the difference of electronic charge. The result is that transitions from the ground state of a neutral molecule to the ground state of the molecular ion (the ionization energy) are unlikely to occur in one step. For clarity, the energy required for a direct transition between molecular states is called the vertical ionization energy, while the energy difference between the molecular ground state and a cationic final state is called the adiabatic ionization energy.

1.2.3 Multi-Step Processes and Autoionization

In the section above, the ambiguity of ionization thresholds suggests that different processes can govern the path a molecule takes following the absorption of a photon. Indeed, the post-absorption excited molecule may undergo multiple transitions before reaching its final resting state, either as a stable cation or as molecular fragments. When a molecule undergoes a photonic excitation, it may fall on a potential energy surface with a local minimum or, at least, a very shallow potential

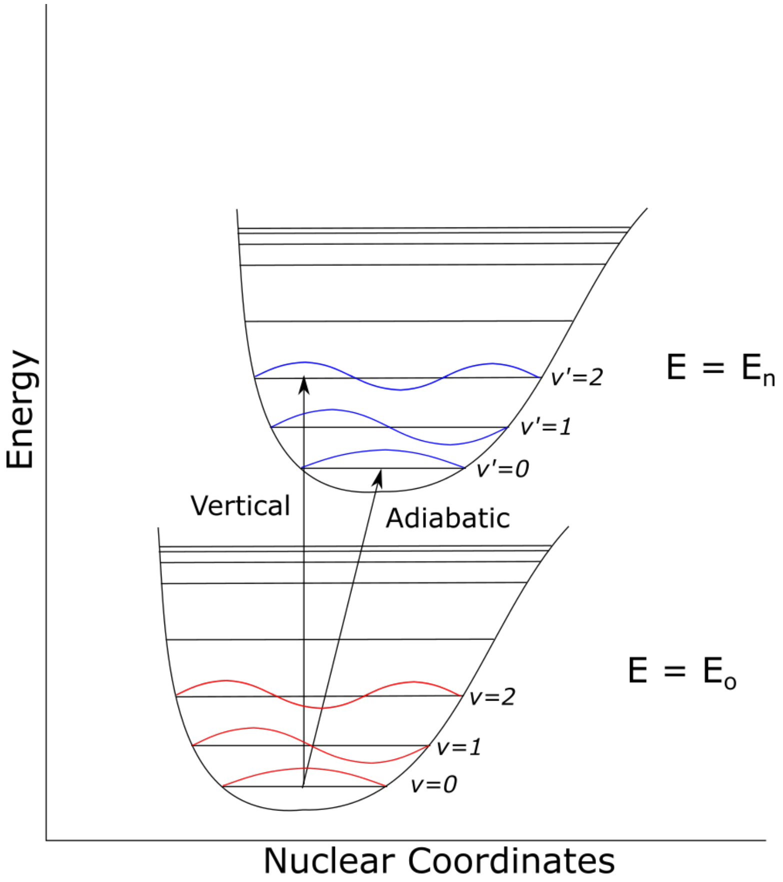

Figure 1.2: The vertical ionization threshold is the energy required to ionized within the Franck-Condon region. The adiabatic threshold is the minimum energy required to transition between states.

gradient. In such a state, the absorbing electron may find itself temporarily bound or with relatively low kinetic energy, respectively. In such a case, the molecular nuclei have time to rearrange themselves - precisely the situation that is ignored under the Franck-Condon principle. Such a scenario corresponds to molecular metastability. The excited electron is bound in the neutral molecular geometry, but as the nuclear vibrational states have time to move the nuclei, the binding potential vanishes. When this happens, the electron follows the unbound potential energy curve and leaves the molecule. Such ionization is referred to as autoionization, and such processes are referred to as multi-step processes.

1.3 Experimental History and Motivation

Any scientific endeavor would be remiss without a careful study of previous work in the field. A thorough exploration of the history in any research field can save invaluable time and effort. Furthermore, the landscape of a research field can change dramatically over the course of a few essential publications.

The historical background for the water experiment will begin in 1986 with P.J. Richardson and J. H. D. Eland [1]. Richardson *et al* conducted a double photoionization experiment using 40.8 eV photons and a Photo-Ion Photo-Ion COincidence measurement (PIPICO) apparatus. PIPICO techniques of the 1980's and 1990's typically involved continuous irradiation of a molecular beam to create the desired reaction.

A time sensitive mass spectrometer array was used to measure time-of-flight (TOF) spectra. The technique is outdated enough that a rigorous discussion of it is not useful. It is sufficient to note that these experiments were incapable of measuring positions, therefore only the molecular fragment kinetic energies could be measured.

Richardson *et al* performed *ab initio* calculations of the low lying water dication energies. They found the direct double ionization threshold to be 39.2 eV. Their PIPICO experiments recorded the energetics for two reaction pathways:

$$\gamma + H_2O \rightarrow H^+ + H^+ + O$$

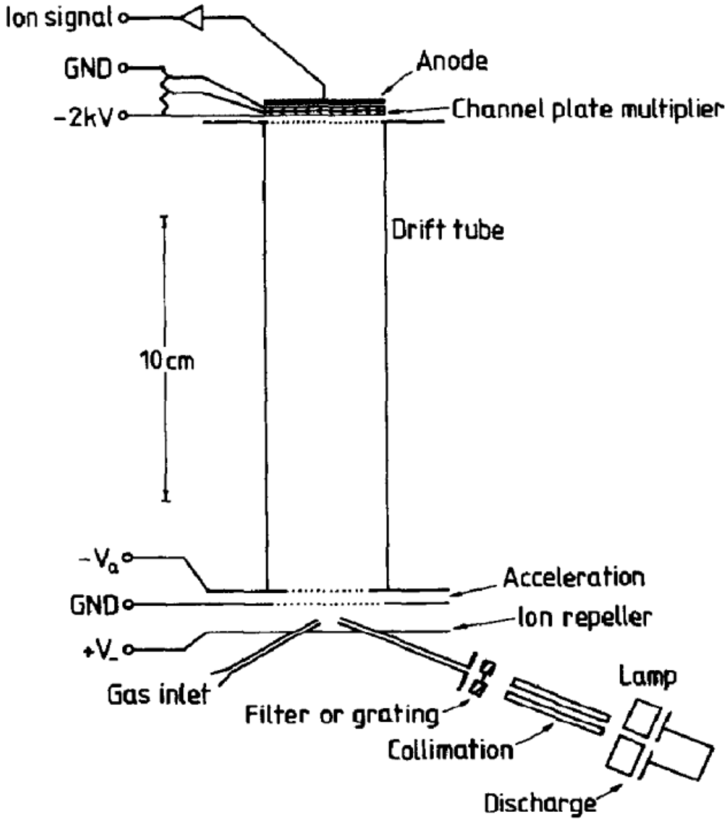

Figure 1.3: An example of a typical PIPICO experimental apparatus. Borrowed from Curtis *et al* [2]

$$\gamma + H_2O \rightarrow H^+ + OH^+$$

while observing small amounts of the third channel:

$$\gamma + H_2O \rightarrow H^+ + O^+ + H$$

The group also targeted D_2O and HDO to investigate any difference between HO and DO bond breakage and to overcome some of the challenges in temporal resolution inherent in their PIPICO apparatus. A summary of their experimental results is shown in table 1.1, and their calculations in table 1.2.

Table 1.1: Experimental Results from Richardson *et al*

Reaction Fragments	**Kinetic Energy Release**	**Dissociation Limit**	**Sum**
H^+OH^+	4.5 ± 0.5	31.7	36.2
$H^+O^+ + H$	5.0 ± 1	36.8	41.8
$H^+ + D^+$	4.5 ± 1	36.7	41.2
$D^+ + D^+$	4.3 ± 1	36.7	41.0

Table 1.2: Energies of Dication States

Dication State	**Excitation Energy Hartree Fock(eV)**	**Excitation Energy MRDCI (eV)**
$(2)^1A_1$	–	45.3
$^1A_1$	39.0	40.7
$^3B_1$	37.0	39.2
$^1B_1$	39.8	42.0
H_2O	0.0	0.0

Richardson *et al* sought to map the energetically available dication states to the different reaction pathways observed in the dissociation. Consequently they assigned the low energy $H^+ + OH^+$ pathway to their calculated $^3B_1$ dication ground state, while assigning the high energy states leading to different reaction pathways to an unresolved mixing of $^1A_1$ and $^1B_1$ excited dication states.

In 1988, Winkoun *et al* [3] performed a PIPICO study using a variable energy photon source. They suggested the water dication could decay via both one- and two-step reaction pathways. Their experiment resolved the Richardson $H^+ + OH^+$ channel with kinetic energy release 4.5±1 into two separate channels with KERs of 3.0 and 5.5 eV. These two channels correspond to the reaction that Richardson mapped to the $^3B_1$ ground state of the dication. Winkoun speculated that these reactions correspond to highly excited H_2O^+ states that later autoionize into $OH^+ + H^+$.

Further investigations using double charge transfer spectroscopy were made by Severs *et al* [4] in 1993. Charge transfer experiments typically involve striking the target molecule with a positively charged ion with high electronegativity. The charged ion "strips" electronic charge from the target molecule, leaving it in a cationic excited state. A mass spectrometer is used to measure the cation, or fragments left over from molecular dissociation. Severs *et al* used OH^+ and F^+ projectile ions to excite the water molecule to the double dication. A summary of their calculations and experimental results are shown in table 1.3. Severs' results are interesting in particular due to their assignment of all the dication energy levels to triplet states.

Table 1.3: Experimental Results from Severs *et al*

Dication Term	**Predicted/Calculated Energy (eV)**	**Experimental Results (eV)**
$^3B_1$	39.3	40.0 ± 0.6
$^3A_1$	43.0	43.2 ± 0.8
$^3B_2$	44.9	45.5 ± 0.6

A rigorous theoretical treatment of the water dication problem was published by Van Huis *et al* [5] in 1999. The group employed several high level *ab initio* techniques and a range of basis sets to investigate several of the lowest energy levels of the water dication. In contrast with Severs' results and in agreement with Richardson and Winkoun, Van Huis assigned the lowest state to the triplet B_1, and the next three states to singlets, as shown in table 1.4.

Table 1.4: Theoretical Results from Van Huis *et al*

$\widetilde{X}^3B_1$	1^1A_1	$\widetilde{b}^1B_1$	2^1A_1
40.10	41.16	42.64	46.08

In 2006, J.H.D. Eland [6] used a TOF-PEPECO (Time Of Flight PhotoElectron-PhotoElectron COincidence) technique to investigate the one- and two-step double ionization processes available to water. By collecting the photoelectrons, Eland was able to identify two separate auto-ionization processes for the breakup of the water dication. Typically, electrons liberated from a molecule in an auto-ionizing process have nearly 0 kinetic energy, a detail that can be exploited in data analysis to isolate such multi-step reaction pathways. Furthermore, it was found that direct one step double ionization process was dominant above the vertical double ionization threshold, as predicted by the Franck-Condon principle.

An important step forward in theoretical treatments of the water dication was taken by Gervais *et al* in 2009 [7]. The group employed an *ab initio* multireference configuration interaction method to generate dication potential energy surfaces for bending angles above 80^o and OH bond distances above 1.0 a.u. They investigated the eight lowest lying potential surfaces and found the lowest triplet and three lowest singlet dication states primarily lead to the formation of a bound residual fragment, i.e., the two-body breakup to $H^+ + OH^+$. The four states situated at higher energies primarily lead to the three-body breakup.

The final stop in this brief, and far from complete, historical section is the experimental paper by Truong *et al* in 2009 [8]. They used a Threshold Photo-Electrons COincidence spectroscopy method, measuring double photoelectron coincidence yields for a distribution of energies between 30-53 eV. They isolated the low lying triplet and three lowest-lying singlet states of the water dication and paired those states to *ab initio* calculations of those state thresholds.

1.3.1 Historical Summary

Early experiments worked to identify the double ionization threshold of water, and found several different states in the 38-45 eV range. There is general consensus that the vertical double ionization threshold of water is very nearly 39 eV. Higher thresholds, from 40-45 eV, yield different kinetic energy releases among the fragments of the decay. These different kinetic energy releases correspond to different excited states of the water dication. Thus far in the literature, considerations of the fragments after dissociation have not been thoroughly discussed. The exception to this is [7], which attempted to map dication states to particular states of the OH^+ fragment in the two step process. The task of this thesis (and, perhaps, parallel or future journal contributions) is to advance the understanding of the decay dynamics of the water dication beyond this historical framework.

1.4 Experimental Apparatus

1.4.1 Overview - COLTRIMS Experiments

The data presented in this thesis was collected using COLd Target Recoil Ion Momentum Spectroscopy (COLTRIMS) [9]. The COLTRIMS technique consists, at least in name, of two parts. First, "cold target" refers to molecular target preparation in ground or near-ground states via adiabatic expansion through a small hole. The cold beam is then collimated to ensure its lab-frame velocity is well known and to minimize the spatial footprint of the molecular target beam. Second, "recoil ion momentum spectroscopy" refers to the collection of the various charged particles released in whatever molecular physics interaction is being studied. The technique is uniquely effective in two ways: it collects *all* charged particles in coincidence, within the dead-time limits of the detectors, and it collects particles for the entire 4π solid angle (Ω). A detailed discussion of each of the constituent pieces that make this experimental apparatus work follows in several sections.

1.4.2 Light Source

The experiment was conducted at beamline 10.0.3.1 at the Advanced Light Source (ALS) synchrotron located on the campus of Lawrence Berkeley National Laboratory (LBNL) in Berkeley, CA. The ALS is a so-called "third-generation" synchrotron light source funded by the US Department of Energy and operated by the University of California.

In extremely brief summary, a synchrotron operates by accelerating bunches of electrons to 99.999996% the speed of light and steering them along an approximately circular storage ring via bending magnets. The storage ring is lined with straight segments consisting of wigglers and/or undulators, devices used to perturb the electrons path resulting in light production at a variety of energies, depending on the particular beamline and its experimental requirements. The light at each undulator or wiggler station is directed down a beam dump, where the experimentalists can further treat the beam with standard optics devices such as mirrors, filters, diffraction gratings, and so on. A typical beamline schematic is shown in 1.4.

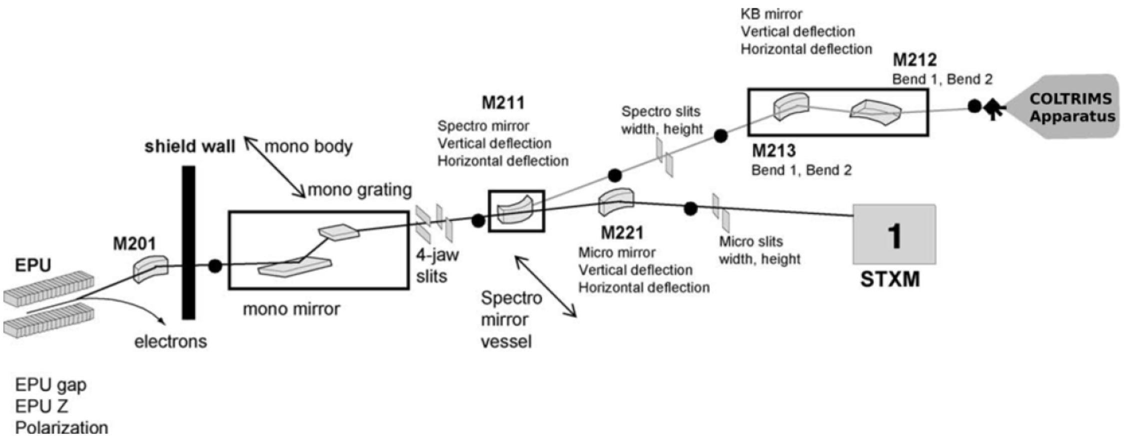

Figure 1.4: Schematic of ALS Beamline

The undulator leading to the experimental beamline used to collect this thesis' data allowed for energy selection and polarization before treatment by beamline-specific optics. Further treatment by a monochromator sharpens the energy distribution of the incoming photon. The monochrometer has several diffraction gratings available for energy selection, as illustrated by 1.5.

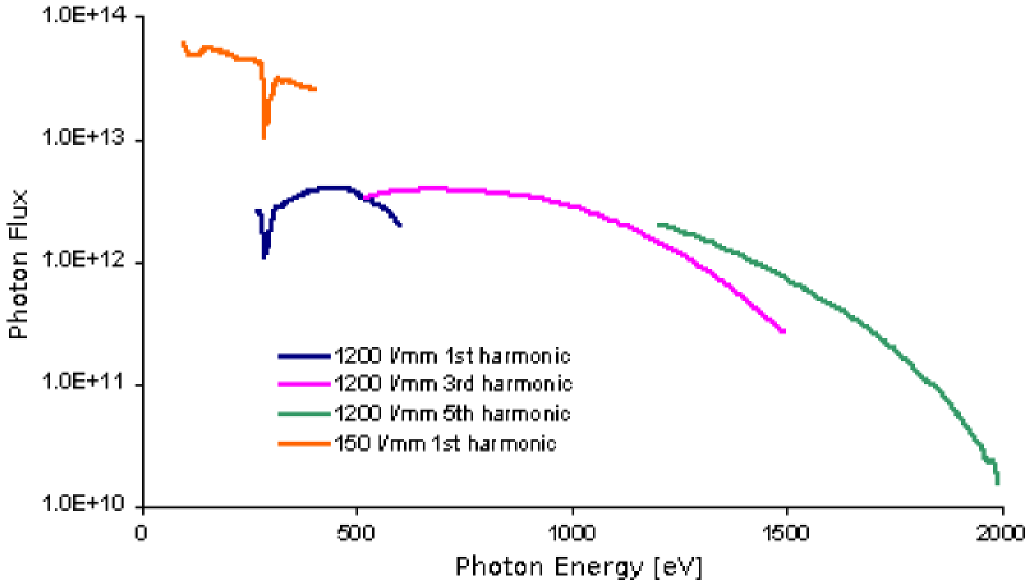

Figure 1.5: Plot of monochromator behavior

As a final tool for incident photon energy resolution, exit slits are available. These slits allow the experimentalist to exchange photon flux for energy resolution, or vice-versa, per the requirements of the experiment.

1.4.3 Experiment Chamber

The experiment chamber consists of four differentially pumped vacuum regions: the jet, second stage, main chamber, and catcher regions. A large helmholtz-coil array and two smaller trim coil arrays surround the chamber, to be discussed in the spectrometer section.

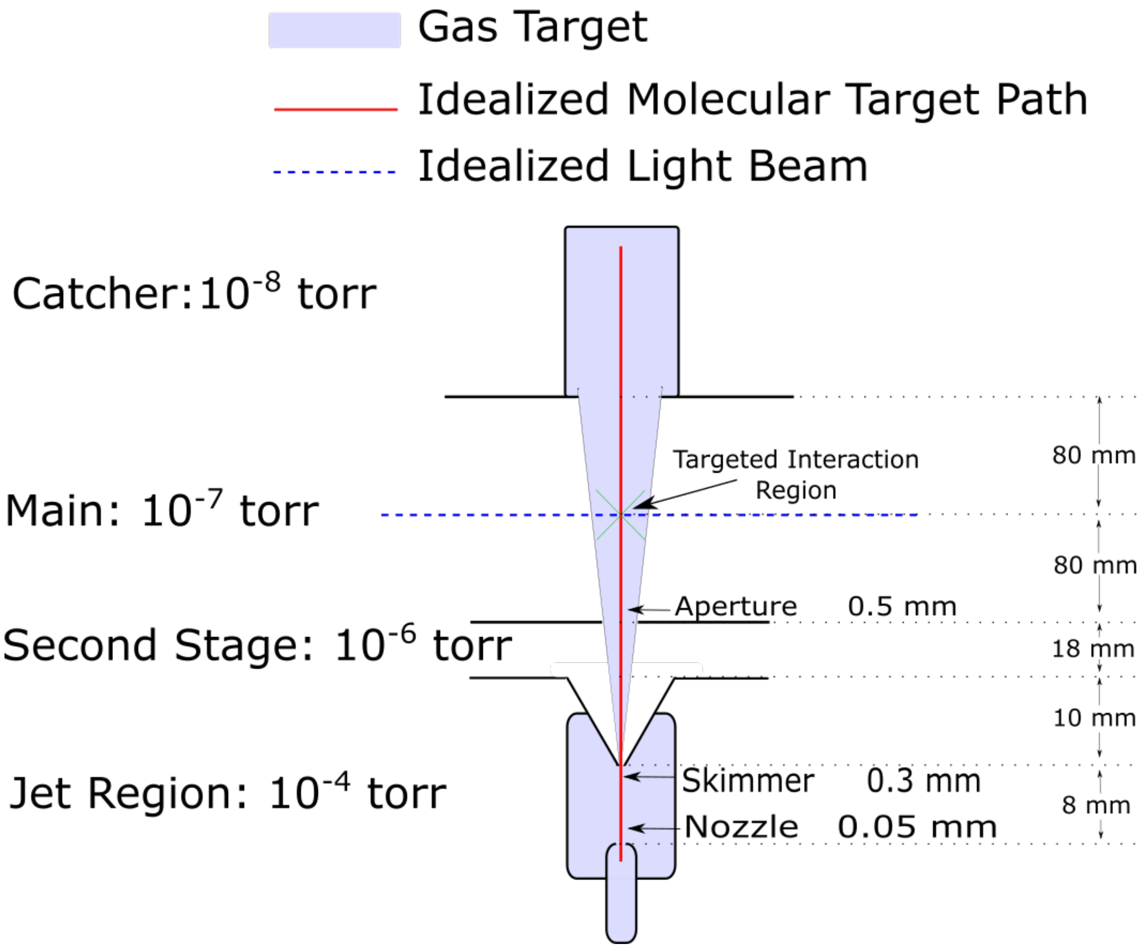

Figure 1.6: Schematic of the Experiment Chamber used for the water experiment.

Jet Region The jet region is the origin of the target gas in the experiment chamber. An external gaseous water reservoir was heated to 150^oC and was fed into the chamber through a gas line heated to 125^oC to prevent water cluster formation. The heated gas line is terminated with a $50\mu m$ nozzle that is exposed to the first vacuum region, the so-called jet region. A large pressure differential forms across the nozzle, through which the gas phase water target is forced into the jet region. The abrupt pressure and volume change causes the gas target to undergo an adiabatic expansion into the jet region, which reduces its rotational and vibrational energy and motivates the "cold target" naming convention. The thermal gas cone expands upward toward a small hole, called a skimmer. The majority of the gas incident on the skimmer is rejected by the conic geometry; the experiment demands gas particles of well defined lab-frame velocity in the interaction region, as well as a minimized spatial profile. A turbo pump evacuates the majority of the unwanted gas from the jet region, which is typically maintained on the order of 10^{-4} torr.

Second Stage The second stage is a small vacuum region through which the gas target passes and undergoes a second stage of collimation and pumping. So-called "hot gas" from the jet region that makes it through the skimmer is unlikely to be directed toward the aperture, and typically bounces around the second stage until interacting with the turbo pump located in that region. The second stage operates at around 10^{-6} torr.

Main Chamber Region The main chamber region is the housing of the primary experimental apparatus, the spectrometer array. Feedthroughs for power supplies and signal I/O allow the experimentalist to control various degrees of experimental freedom without resorting to opening the chamber. The photon beam enters and exits the main chamber region along an axis perpendicular to the length of the spectrometer array. Finally, an externally controlled phosphor screen can be raised and lowered along the axis of the light beam for alignment assistance, viewed from several glass windows into the chamber. The main chamber vacuum is the most important, as any contamination of the photon's beam path results in aberrant data collection. It is maintained around 10^{-7} torr.

Catcher Region The catcher region operates as a molecular beam dump after the target gas exits the main chamber. Due to the extremely small interaction cross sections and low target density, the majority of the gas target passes through the spectrometer without interacting with the photon beam. To reduce the amount of aberrant gas particles contaminating the chamber, a long tube with an extra turbo pump attached is used to "catch" the gas as it exits the spectrometer. This helps reduce the amount of gas available for the photon beam to ionize outside the interaction region, so-called "hot gas". The catcher region typically operates around 10^{-8} torr.

Summary The goal of the multi-staged differential pumping is to produce as narrow a molecular target profile as is practically possible, populated by particles mostly occupying their ground states. The geometry of the nozzle, skimmer, and aperture repetitively maximize the velocity distribution $\frac{V_{\parallel}}{V_{\perp}}$, which produces the desired narrow beam.

1.4.4 Spectrometer

The spectrometer array consists of two particle detectors separated by several externally controlled electrostatic acceleration regions. A magnetic field is provided by external Helmholtz coils and runs parallel to the length of the spectrometer.

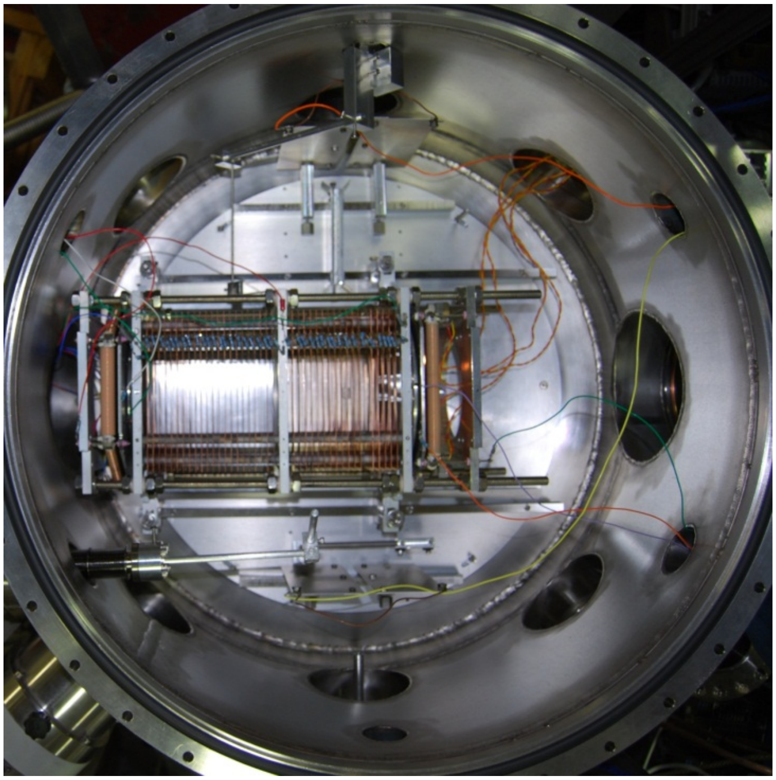

Figure 1.7: Photograph of the Spectrometer used at the LBNL beamline.

The electrostatic acceleration regions are formed by a series of equidistant metallic plates, connected in series via resistors. Each region has uniquely specified electric fields (see below).

Electric and Magnetic Fields The area where the light beam and molecular beam intersect is called the interaction region. It constitutes the center of the spectrometer, where the photon beam crosses the molecular beam at (ideally) 90^o, with both beams mutually perpendicular to the axis of the spectrometer. Within the interaction region, a constant electrostatic field of $8.1\frac{V}{cm}$ is applied, and is often referred to as the extraction field. Upon photoionization, the extraction field separates the electrons and positive ions, pushing each toward their respective detectors.

The ion detector is found within the region of the extraction field. The ions experience a constant F_E after the ionization event and are pushed onto the ion detector to ensure a $4\pi\ \Omega$ solid angle detection efficiency.

The electrons, upon exiting the interaction region, are allowed to travel without any acceleration due to an electric field. This field free region, called the drift region, is approximately twice the distance from the ionization point to the end of the interaction region. The use of a drift region in mass spectrometry is due to early techniques developed by W.C. Wiley and I. H. McLaren [10]. They found that a drift region was the best way to produce time focusing of charged particle sources with finite-volume origins. Due to the finite size of the molecular- and photon-beam overlap, the electrons (and ions) are not all created in the same location in space. This spacial imperfection causes the time signature to be blurred out, which in turn reduces energy and angular resolution. The drift region technique, often called McLaren geometry for brevity, serves to sharpen time-of-flight resolution.

The particles are also subjected to an 8.55 Gauss magnetic field, colinear with the axis of the spectrometer. The massive positive ions experience very little acceleration due to F_B, but the electron path is strongly perturbed. The magnetic field acts to confine the electrons liberated in the molecular dissociation event. This effect is best displayed using cylindrical coordinates, wherein the axis of the spectrometer is the $\hat{z}$ axis. Upon ionization, electrons move radially outward from the point of the ionization event. In cylindrical coordinates (r, ϕ, z), this means the electron has some velocity vector

$$\overrightarrow{v} = v_z\hat{z} + v_r\hat{r} \tag{1.1}$$

The B field is coaxial with the spectrometer, such that

$$\overrightarrow{B} = B_z\hat{z} \tag{1.2}$$

The force on an electron due to the magnetic field, F_B is

$$F_B = -e \cdot (\overrightarrow{v} \times \overrightarrow{B}) \tag{1.3}$$

$$\begin{vmatrix} \hat{r} & \hat{\phi} & \hat{z} \\ v_r & v_\phi & v_z \\ B_r & B_\phi & B_z \end{vmatrix} = \begin{vmatrix} \hat{r} & \hat{\phi} & \hat{z} \\ v_r & 0 & v_z \\ 0 & 0 & B_z \end{vmatrix} = 0 \cdot \hat{r} - v_r B_z \cdot \hat{\phi} + 0 \cdot \hat{z} = -v_r B_z \hat{\phi}$$

The $\hat{\phi}$ force component imparts a $\hat{\phi}$ velocity component, which in turn produces a $\hat{r}$ force component through the $\overrightarrow{v} \times \overrightarrow{B}$ relationship of the Lorentz force. The electron travels upon a gradually widening helical path toward the detector, orbiting the $\hat{z}$ axis. Eventually it reaches a cyclotron radius that is smaller than the radius of the detector and achieves radial equilibrium; thusly, the $\overrightarrow{B}$ field confines the electrons and facilitates $4\pi\Omega$ detection efficiency.

Detectors Both the electron- and ion-detectors are delay line anode micro-channel plate (DLA MCP) detectors. The micro-channel plate is a thin slab of resistive material with a honeycomb-like lattice of tiny angled tubes piercing through its width. Upon impact by an energetic charged particle, the MCP releases a shower of electrons. An electrostatic gradient is applied across the plate to establish an electric field that guides the shower of electrons down the lattice of holes. Typical ΔV across the width of the MCP is $2500V$. As the liberated surface electrons bounce along the holes, more electrons are released. The MCP, which typically involves two plates adjacent to each other, acts as a signal multiplier to convert a single charged particle hit into a large electronic signal suitable as an input to an amplifier.

The DLA is a square (in the case of the recoil detector) or hexagonal (in the case of the electron detector) lattice of wire pairs. The wire pairs are wrapped around a metal plate, but are isolated from the plate by plastic. The metal plate, called the anode holder (AH), is held at a voltage approximately 50V above the near side of the MCP. This potential difference attracts the electron cloud (which represents a physics event from the interaction region). The wire pairs, called "signal (SIG)" and "reference (REF)", are held at +100V and +150V from the AH, further drawing the electron cloud onto the DLA. As the energetic electron cloud passes through the wire pair, the wire pair acts as a wave guide-like antennae, detecting the changing electric field and propagating that information in both directions along the wires. The use of this signal will be discussed in the next section.

1.4.5 Signal and Data Processing

The electronic signal output of the detector device comes as two pulses (per wire pair), each traveling down the signal/reference pair in opposite directions, away from the location of the hit on the detector. To consider the full picture of signal processing, however, it will be worth pausing at this step and consider the experiment as a whole.

The chain of events leading to an acquired data event is as follows. The synchrotron light source pulses twice per revolution while in two-bunch operation, or once every 328.15 ns. This pulse constitutes $t_o = 0$, the beginning of the time-of-flight for each of the particles. Next, due to the presence of the electric and magnetic fields in the spectrometer, the charged particles are accelerated toward the MCP-DLA detectors for collection. When the charged particles collide with the MCPs, a large quantity of electrons are liberated from the surface. This abrupt change in charge density changes the electrostatic potential of the MCP, which is to be held constant by a high voltage power supply. To accommodate the change in charge density, the power supply pushes electrons back onto the MCP to restore the voltage dialed in on the device. This instantaneous current change is measured as a pulse, and is marked as the time the particle hit the detector, t_{MCP}. Next, as the electron cloud from the back of the MCP passes through the DLA wire pair layers, pulses travel in each direction of the wire pairs and are measured. The travel speed of these pulses along the wire pairs is

$$v_{signal} = \frac{L}{t_1 + t_2} \tag{1.4}$$

where L is the length of the wire pair across the DLA and (t_1, t_2) are the arrival times of the pulses exiting the DLA in each direction. The distance of the pulse from either of the edges of the detector is just

$$x_{1,2} = v_{signal} \cdot t_{1,2} \tag{1.5}$$

Taking the difference between these distances yields the position measurement that will be used for analysis, with an origin at the center of the detector.

$$x = v_{signal} \cdot (x_1 - x_2) \tag{1.6}$$

Once the position of the event is recorded, the event acquisition is considered complete. The measured pulses from the MCP, DLA, and synchrotron are fed into a series of signal processing units (see ***signal processing*** below) to form digital pulses usable by the acquisition computer.

Signal Processing The MCP and DLA signals are fed into fast amplifiers in preparation of use in nuclear instrumentation module (NIM) signal processing devices. Since the goal of the signal processing units is to accurately deliver a timing signature to the analysis computer, the exact time that a pulse occurs is crucial. Unfortunately, pulse sizes from the DLA are not normalized. As a result, voltage threshold triggering and gating can both introduce noise and discard good events.

The solution is to employ a constant fraction discriminator (CFD). The CFD takes an analogue pulse as an input, then splits that pulse into two pulses. It inverts one pulse, delays it by a fixed amount, then recombines the split pulses. The result

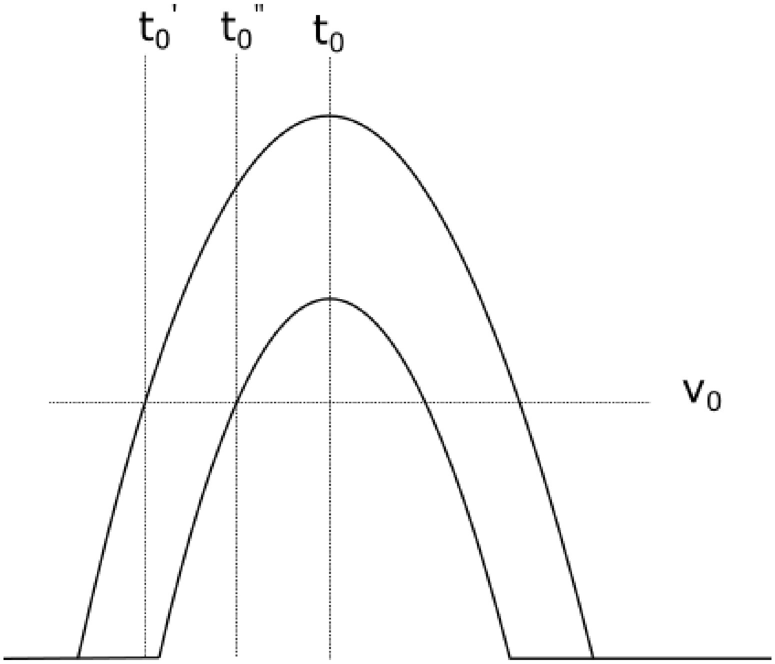

Figure 1.8: Threshold triggering will yield different times for pulses of different heights, even if those pulses occur simultaneously.

of this treatment is to create a semi-sinusoid wave packet with a zero crossing that is *independent of original pulse height*, effectively negating the time resolution problem presented by pulses of varying heights.

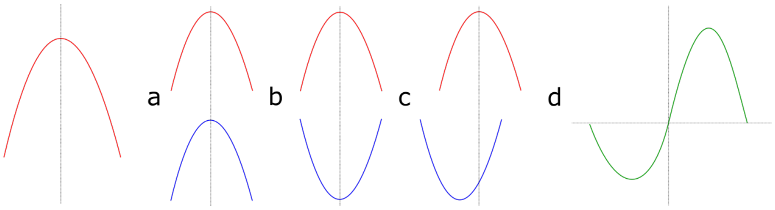

Figure 1.9: A constant fraction discriminator operates by **a)** splitting the pulse **b)** inverting one of the pulses **c)** delaying one of the pulses **d)** recombining the pulses

After treatment with a CFD, the position signals from the DLA are fed into a time-to-digital converter (TDC) card in the acquisition computer. The MCP signal is split: one signal is fed directly into the TDC, while the other is coupled to the ALS bunch marker signal in a logical AND gate.

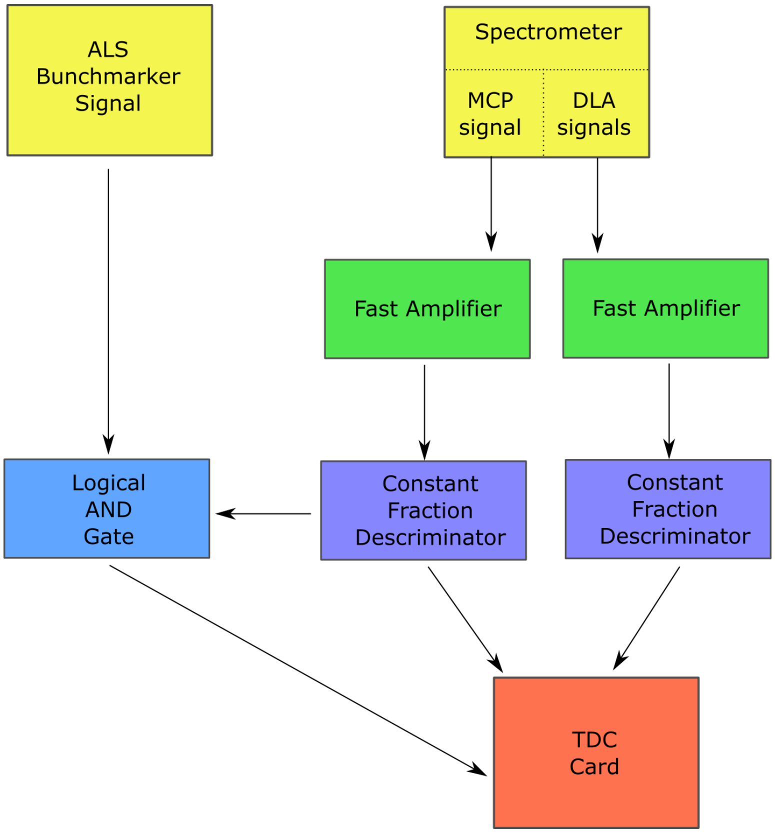

Figure 1.10: Pictoral representation of signal processing strategy

The experimentalist is left with a series of times, positions, and the field strengths inside the spectrometer. From these values, three dimensional momentum and energy information can be found. This process is the focus of **Chapter 2: Data Analysis and Results**.

Chapter 2

Water Experiment - Data Analysis and Results

2.1 Introduction

The experimental output described in the previous chapter can be reduced, very simply, to the production of a collection of timing signatures. The task of the experimentalist is to convert these timing signatures into physical quantities of interest: time of flight, position, and detection coincidence verification. From these basic values, more advanced calculations can be made to find momenta, angular distributions, and energies, as well as molecular reference frame transformations that make all of these quantities more elucidating. This process, and the fruits of that labor, are the subjects of this chapter.

2.1.1 Simulations

The COLTRIMS technique measures multiple particles in coincidence. This powerful molecular microscope technique comes with a significant cost, however: data acquisition is oppressively slow. It is a price worth paying, once the data is collected, but the problem is significant enough that every possible effort must be made to minimize wasted time. To further compound the problem, the two-bunch mode of the ALS operates for 4 weeks per year. This confluence of challenges makes the beam time *extremely* valuable. As a result, all the experiments (barring impromptu ideas) are planned ahead of time, and experimental degrees of freedom are simulated to pick the optimal starting point.

Microsoft Excel A spreadsheet consisting of a myriad of experimental degrees of freedom, such as interaction region electrostatic field, jet velocity, and magnetic field, has been developed by the research collaboration responsible for this data collection. The spreadsheet allows experimentalists to approximate the required field strengths to achieve $4\pi\ \Omega$ collection efficiency. While these values are only rough estimates, they give the experimentalists an excellent starting point when data acquisition begins. Variations on these starting points to the desired settings takes tens of minutes, rather than the many hours an entirely guess-based approach might.

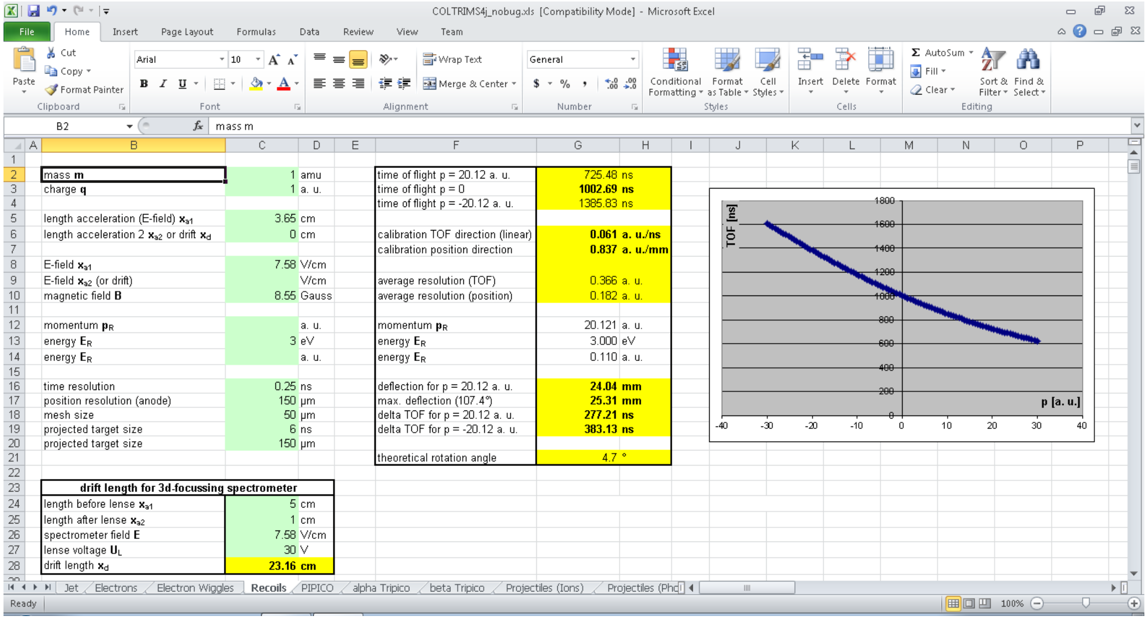

	B	C	D	F	G	H
1						
2	mass **m**	1	amu	time of flight p = 20.12 a. u.	725.48	ns
3	charge **q**	1	a. u.	time of flight p = 0	**1002.69**	**ns**
4				time of flight p = -20.12 a. u.	1385.83	ns
5	length acceleration (E-field) $\mathbf{x}_{a1}$	3.65	cm			
6	length acceleration 2 $\mathbf{x}_{a2}$ or drift $\mathbf{x}_{d}$	0	cm	calibration TOF direction (linear)	**0.061**	**a. u./ns**
7				calibration position direction	**0.837**	**a. u./mm**
8	E-field $\mathbf{x}_{a1}$	7.58	V/cm			
9	E-field $\mathbf{x}_{a2}$ (or drift)		V/cm	average resolution (TOF)	0.366	a. u.
10	magnetic field **B**	8.55	Gauss	average resolution (position)	0.182	a. u.
11						
12	momentum $\mathbf{p}_{R}$		a. u.	momentum $\mathbf{p}_{R}$	20.121	a. u.
13	energy $\mathbf{E}_{R}$	3	eV	energy $\mathbf{E}_{R}$	3.000	eV
14	energy $\mathbf{E}_{R}$		a. u.	energy $\mathbf{E}_{R}$	0.110	a. u.
15						
16	time resolution	0.25	ns	deflection for p = 20.12 a. u.	**24.04**	**mm**
17	position resolution (anode)	150	µm	max. deflection (107.4°)	**25.31**	**mm**
18	mesh size	50	µm	delta TOF for p = 20.12 a. u.	**277.21**	**ns**
19	projected target size	6	ns	delta TOF for p = -20.12 a. u.	**383.13**	**ns**
20	projected target size	150	µm			
21				theoretical rotation angle	4.7	°
22						
23	**drift length for 3d-focussing spectrometer**					
24	length before lense $\mathbf{x}_{a1}$	5	cm			
25	length after lense $\mathbf{x}_{a2}$	1	cm			
26	spectrometer field **E**	7.58	V/cm			
27	lense voltage $\mathbf{U}_{L}$	30	V			
28	drift length $\mathbf{x}_{d}$	**23.16**	**cm**			

Figure 2.1: Example image of the Excel spreadsheet used to estimate particle time-of-flight.

The Excel simulation can also help identify different ion species based on their expected TOFs.

2.1.2 Calibration Data

Calibration data is typically taken after experimental data, chronologically, to ensure that the calibration data is taken with the correct spectrometer settings that correspond with the experimental data. This calibration data is used to ensure the parameters of the analysis software will produce accurate values for momentum, angles, and energy.

2.1.3 Data Acquisition System

The timing signals sent to the acquisition computer are processed by a special PCI card called a time to digital converter (TDC). Within a strictly scrutinizing view, the data is no longer *continuous*, as the computer operating the TDC is forced to bin the data within discrete units based on the processor of the machine. The time resolution of the experiment is nowhere near the typical operating speeds of modern processors, however, so the problem of binning continuous data is not significant.

COBOLD The digitized time data is processed with a software package called COBOLD. The software is written and maintained by RoentDek, the manufacturer of the MCP-DLA detectors used in the experiment. COBOLD is a fully realized acquisition and analysis framework that allows the user to customize variables, perform mathematical operations, and plot the variables in real time during data collection.

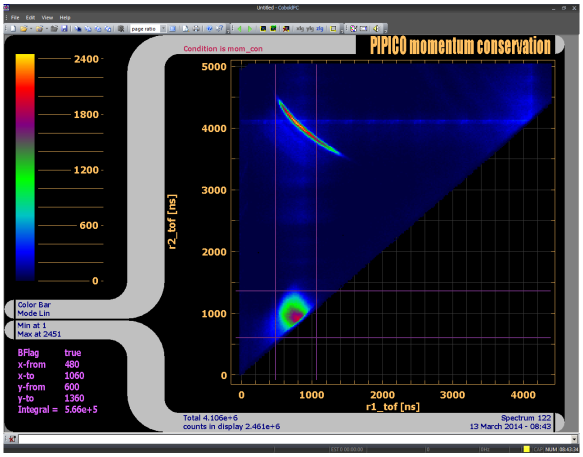

BFlag true
x-from 480
x-to 1060
y-from 600
y-to 1360
Integral = 5.66e+5

Total 4.106e+6
counts in display 2.461e+6

Spectrum 122
13 March 2014 - 08:43

Figure 2.2: The acquisition software allows the display of custom plots in real time.

LMF2ROOT While COBOLD is fully capable of performing all of the operations needed to analyze COLTRIMS data, a more powerful and specialized analysis framework has been developed. COBOLD writes the incoming data to a list mode file (LMF), a large scale text format. The specialized analysis framework reads the data in these list mode files and writes them to ROOT histogram data structures. ROOT is an analysis framework written and maintained by CERN, not entirely unlike COBOLD itself in purpose. The software used to convert from LMF files produced by COBOLD to ROOT files is called, appropriately, LMF2ROOT. ROOT is written in C++ and is extremely similar syntactically. LMF2ROOT exploits this convenience by using C++ code to perform both basic and complex calculations and data manipulation, then creates ROOT histograms natively, which can then be viewed by the experimentalist and further manipulated in the ROOT framework at the leisure of the experimentalist.

2.2 Pre-Analysis: Calibration, Detector Orientation, Coincidence

Before the results of the experiment can be considered, the experimentalist must ensure the data are correctly calibrated. This process involves using calibration data, properly orienting the detector images, and using logical coincidence techniques to gate false events.

2.2.1 Time Sum

The first step is to use a data correlation technique called a time-sum. The raw data coming from the TDC corresponds to time signatures, all taken relative to an experimental master clock. When a particle strikes the MCP, the voltage pulse provided by the HVPS is recorded, t_{MCP}. Next, two pulses (per wire pair across the DLA) are recorded, $t_1^{'}$ and $t_2^{'}$. The travel times for the DLA pulses, from creation to measurement, are the time difference between the master clock measurement of these pulses minus the creation time of the pulse, which coincides with the pulse of the MCP:

$$t_1 = t_1^{'} - t_{MCP} \tag{2.1}$$

$$t_2 = t_2^{'} - t_{MCP} \tag{2.2}$$

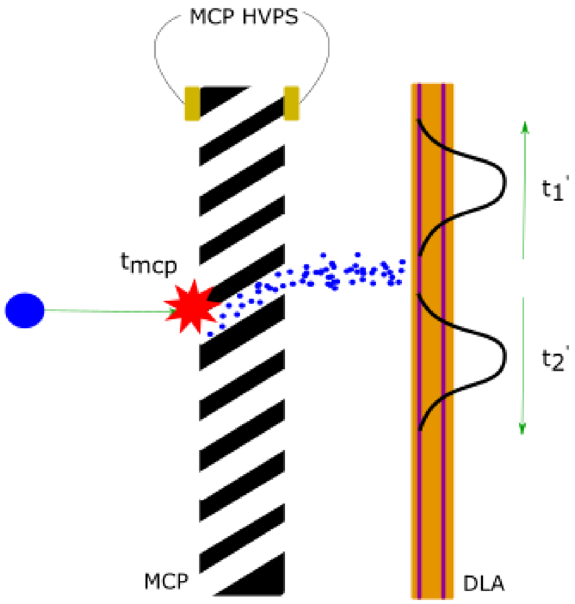

Figure 2.3: Illustration of the times used in the Time Sum technique

The time that a theoretical pulse created at one extreme end of the detector and traveling along the full width of the detector is fixed. For a non dispersive wave travelling with constant velocity, the time is simply:

$$t_{full} = \frac{d_{detector}}{v_{pulse}} \tag{2.3}$$

With equations (2.1,2.2,2.3) in mind, it is clear that the sum of the two pulse times, $t_1 + t_2$ should be a constant. In fact, it is largely unimportant what that constant is. As a result, any combination of detector signals that do not yield a consistent time-sum can be discarded as unusable events.

2.2.2 Detector Orientation

Proper orientation of the detectors serves two purposes. First, it helps the experimentalist visualize the raw data, which in turn helps separate real data from false events. This is, strictly speaking, not necessary for data analysis, but it saves a substantial amount of time in the analysis stage. Second, the ion and electron detectors are not aligned automatically. That is, the lab frame coordinates of the ion detector and the lab frame coordinates of the electron detector are not equal. This leads to severe complications in the analysis phase, and can very easily cause errors.

To orient the detectors, the lab frame is defined in the following way. The photon beam provided by the ALS moves in the $+\hat{x}$ direction. The molecular water beam moves in the $+\hat{y}$ direction. The axis of the spectrometer falls along the z-axis, with the ion detector defining the $+\hat{z}$ direction and the electron detector defining the $-\hat{z}$ direction.

In figure 2.4, the shape of the circular MCP is made apparent. Several features appear that will help orient the detector. The vertical stripe across the detector is commonly called the "hot gas stripe." The chamber has residual gas particles - it is maintained at a vacuum of around 10^{-7} torr. Those gas particles are largely due to imperfections in jet collimation. Some of the gas particles that are rejected by the two stages of gas collimation find their way into the main chamber. Such particles may collide with a turbo pump and are then removed, but most merely bounce around inside the chamber. The light from the ALS indiscriminantly ionizes all particles in its path. That band of ionized particles and electrons are then pushed toward their respective detectors. This background ionization manifests as a stripe

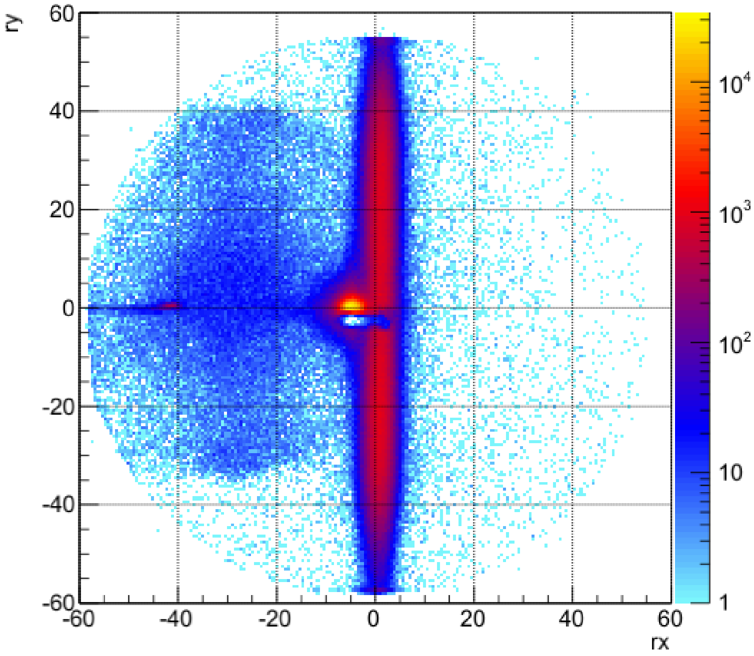

Figure 2.4: The recoil detector data, as it is fed into COBOLD, does not necessarily default to the frame the experimentalist wants to use.

along the direction of the photon beam - which allows the experimentalist to define that direction however they choose.

The horizontal stripe extending from the center of the image to the left edge represents the molecular gas beam. Inside the chamber, the molecular beam is made up largely of ground state neutral water molecules. After the molecular beam counters the ALS light beam, many particles are ionized in a wide variety of ways, many of which are uninteresting to the experimentalist. Some of the post-collision states are highly excited neutral Rydburg states, with half-lives on the order of nanoseconds. Such excited molecules will continue to travel with the velocity of the molecular jet (toward the jet catcher region) until they either exit the chamber, autoionize, or field-ionize within the electric field of the spectrometer. In any of these cases, the ions are created along the path of the molecular beam, rather than in the small region where the molecular and photon beams interact directly. The result is a column of ionization events, stretching from the interaction region to the jet dump.

A smaller circular pattern of diameter $80mm$ appears on the left side of the ion detector. This is due to a reflection of the electron detector. While the typical outcome of an electron striking an MCP is the production of more electrons, sometimes an ion is ejected from the surface as well. In such a case, the ion is accelerated through the electric field in the spectrometer and is measured on the ion detector at the opposite end of the spectrometer. The image is offset from the center because the channels inside the MCP are sliced at an 8^o grade.

The final feature worth noting is the bright spot very near the center of the detector. These are the actual ionization events the experimentalist is interested in - events that occur within the overlapping molecular and photon beams. This bright spot is offset slightly from the center due to the velocity of the gas jet, a fact that will be used later in spectrometer calibration.

With the features of figure 2.4 it is clear that a clockwise rotation of 90^o will properly orient the ion detector.

Orientation of the electron detector is a different matter altogether. The electron detector is a hexagonal detector, i.e., it has three wire pair layers rather than the two layers of the ion detector. At first glance, it is obvious that rather than being

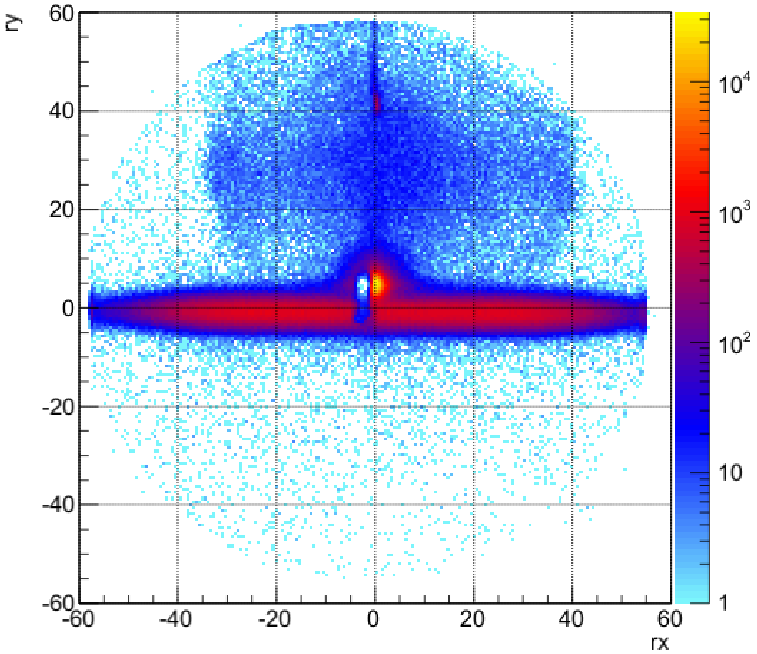

Figure 2.5: A 90^o clockwise rotation properly orients the recoil ion detector.

off by a rotation of $n \cdot 90^o$, the electron orientation will be off by some rotation of $n \cdot 60^o$.

The hot gas stripe is visible in the raw detector image. However, proper orientation is impossible with only a one-dimensional guideline. To orient the electron detector, the reflection on the ion detector will be exploited. Reflection events on the ion detector will also be recorded on the electron detector, as the COLTRIMS apparatus measures events in coincidence. Applying gates that target unique regions inside the reflection of the electron detector will yield a similar pattern on the electron detector, which can then be used to orient it.

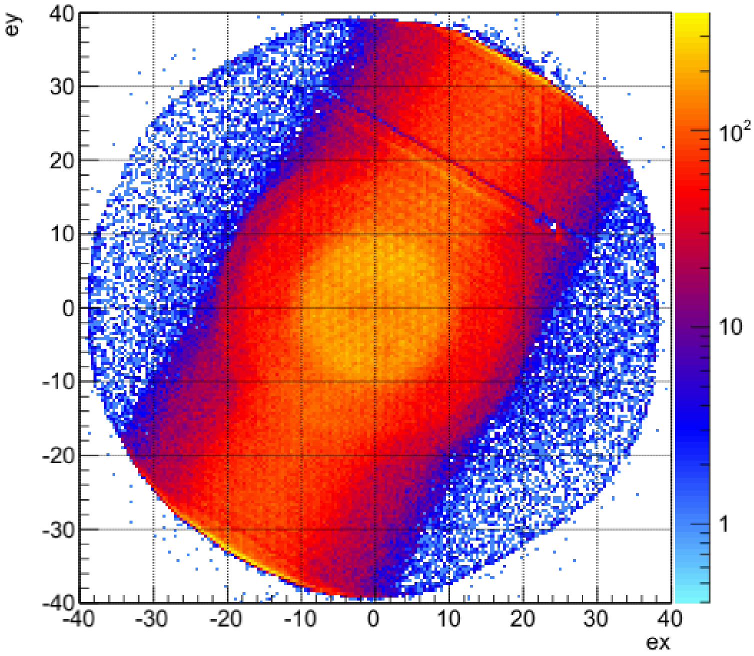

Figure 2.6: The electron detector raw image lacks the amount of helpful distinguishing features of the recoil detector image.

2.2.3 Interactive Parameter Adjustment

All the measurements taken in the lab are prone to some amount of error, be it instrumentation error, human error, or otherwise. While all steps practically possible must be taken to avoid human error, other sources of error are frequently unavoidable. In such cases, COLTRIMS experimentalists look to the data to retroactively calibrate the spectrometer to minimize such error.

The LMF2ROOT analysis framework includes spectrometer setting variables that are used as inputs to momentum calculations. As a starting point, the values

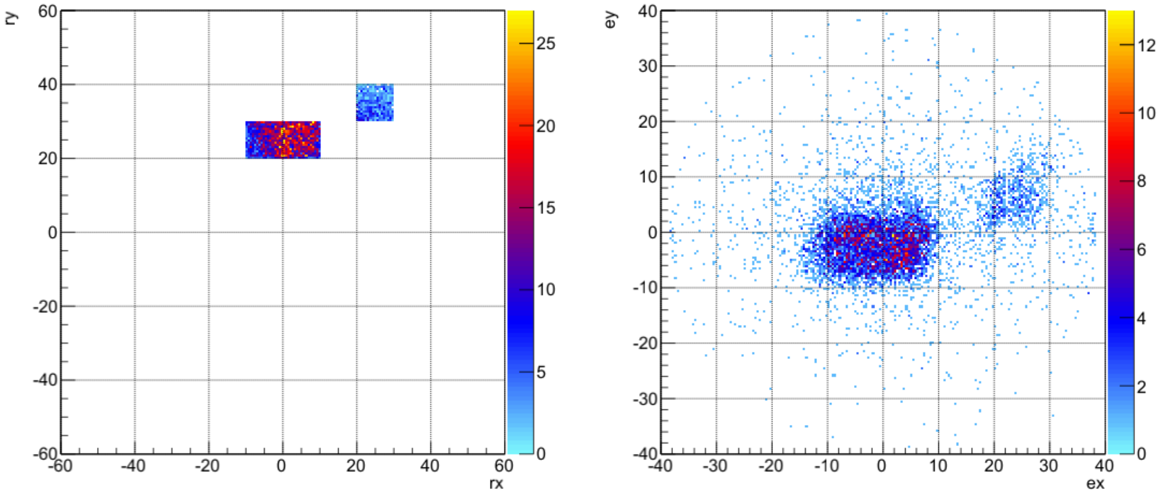

(a) Two gates offset in both the x and y dimensions will allow the electron detector to be oriented properly.

(b) A reflection about the x-axis and a -120^o rotation yield the correct orientation.

Figure 2.7: Orienting the electron detector via reflection gating.

from the live experimental lab notebook are used, but these values are merely estimates. A particular power supply's digital readout may say 8.4 volts, but not only is that measurement limited by the significant figures, it's internal calibration may well be inaccurate as well. In an experiment as complex as COLTRIMS, a wide array of such unanticipated errors can be imagined. COLTRIMS experimentalists turn to basic physics to help calibrate the spectrometer variables.

The primary tool in this analysis framework is the Interactive Parameter Adjustment, or IPA. The IPA will parse a small amount of data from a given reaction pathway and will display this data in root. The IPA has an interactive menu of adjustable parameters that, upon a manual update, will recalculate the displayed data.

In this way, the experimentalist can apply some **ab initio** concepts to calibrate the experiment.

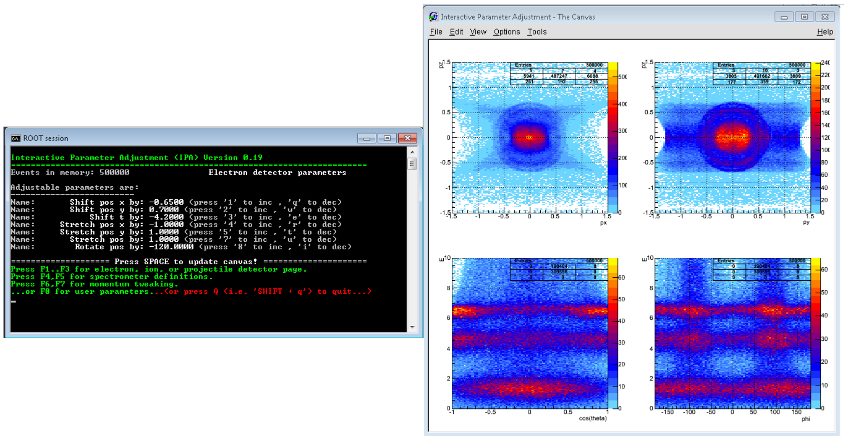

```
Interactive Parameter Adjustment (IPA) Version 0.19
==========================================================================
Events in memory: 500000                        Electron detector parameters

Adjustable parameters are:
-------------------------
Name:         Shift pos x by: -0.6500 (press '1' to inc , 'q' to dec)
Name:         Shift pos y by: 0.7000 (press '2' to inc , 'w' to dec)
Name:             Shift t by: -4.2000 (press '3' to inc , 'e' to dec)
Name:       Stretch pos x by: -1.0000 (press '4' to inc , 'r' to dec)
Name:       Stretch pos y by: 1.0000 (press '5' to inc , 't' to dec)
Name:         Stretch pos by: 1.0000 (press '7' to inc , 'u' to dec)
Name:          Rotate pos by: -120.0000 (press '8' to inc , 'i' to dec)

==================== Press SPACE to update canvas! =====================
Press F1..F3 for electron, ion, or projectile detector page.
Press F4,F5 for spectrometer definitions.
Press F6,F7 for momentum tweaking.
...or F8 for user parameters...(or press Q (i.e. 'SHIFT + q') to quit...)
_
```

Figure 2.8: The IPA assists the experimentalist in calibrating the analysis software.

When a two body breakup occurs, the resulting Coulomb explosion conserves momentum. The charged particles travel through the interaction region, where the static electric field imparts an acceleration on them, and onto the detector. Plotting tof_2 vs tof_1 will yield parabolas for any particle pair that conserves momentum. Within the IPA framework, a PIPICO tool exists that will calculate these parabolas and overlay them with the data. The parabola depends on the particles mass, charge, and the field strength and length of the acceleration region. The PIPICO tool takes these experiment parameters and calculates the PIPICO parabolas. As the lengths of the regions, charges, and masses are known, adjusting the acceleration region's field strength until the PIPICO calculation overlays the data effectively determines the true strength of the electric field.

Next, the isotropy of the unaligned molecular decay is exploited to adjust the individual field momenta, the time of flight, and the magnetic field strength.

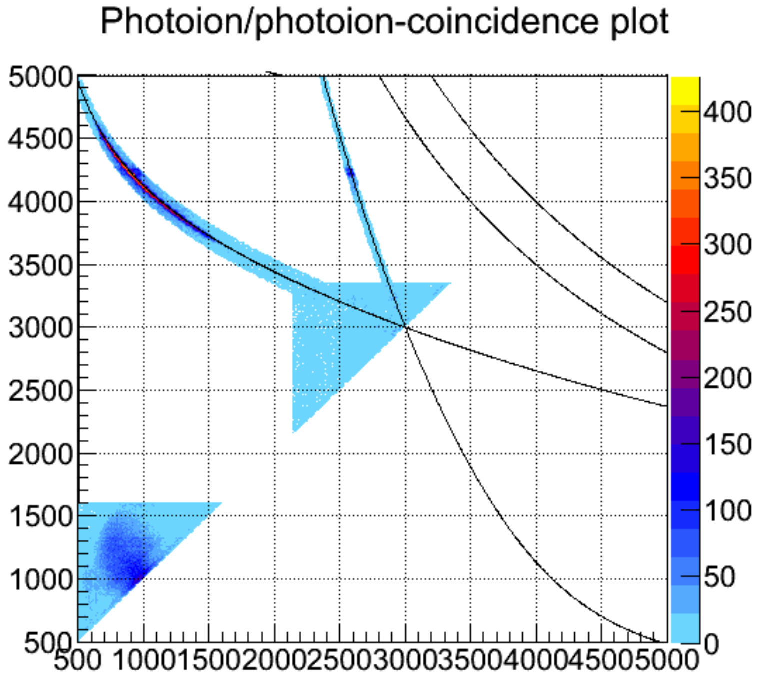

Figure 2.9: The IPA's PIPICO tool is used to calibrate the electric field strength.

In the lab frame, the $\hat{z}$ axis is chosen as the direction of the photon polarization. Any effects of this polarization on the photoelectron distribution should by symmetric about this axis. The photoelectron energy, in particular, should have no angular dependence. Therefor, plots of photoelectron energy against ϕ and the solid angle weighted $cos(\theta)$ should be straight horizontal lines (see figures 2.11 and 2.10).

As a final note, the calibration data is always taken from well known atomic or molecular species. The single ionization of helium, nitrogen, N_2, and so on are common targets. For this experiment, calibration data was taken with water, simply because it was convenient at the time of data collection. The calibration used for this experiment was the single photoionization of water using $20eV$ photons. There are

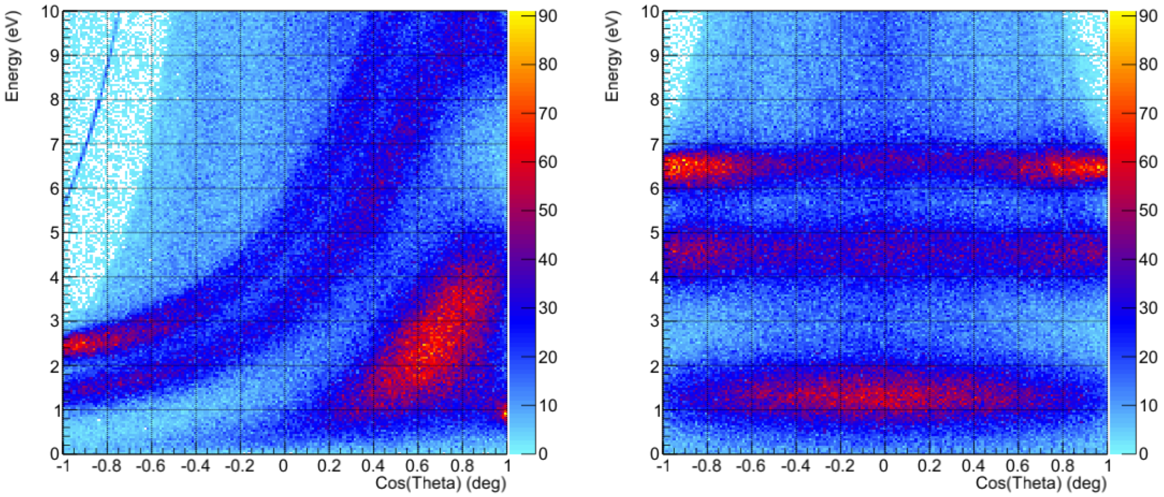

Figure 2.10: Electron energy vs $cos(\theta)$ (left) before and (right) after adjusting positions, times, and magnetic field strength.

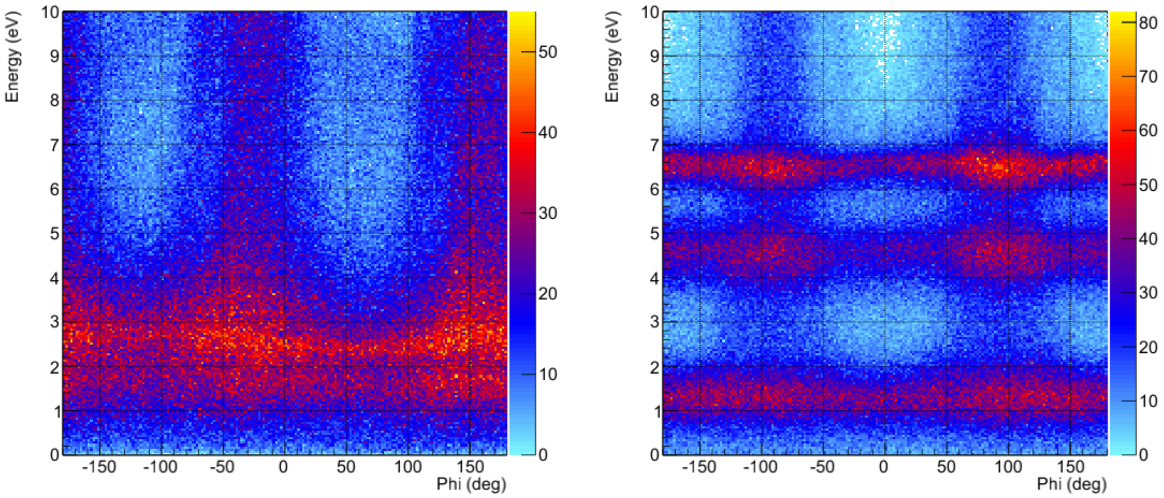

Figure 2.11: Electron energy vs ϕ (left) before and (right) after adjusting positions, times, and magnetic field strength.

three accessible cation states within $20eV$ of the water ground state [11], including the cation ground state. For these states, conservation of energy states

$$E_{watergroundstate} + E_{\gamma} - E_{cationstate} = E_{electron} \tag{2.4}$$

A summary of this calibration and the historical data are shown in table 2.1, and a schematic showing the conservation of energy for the system is shown in figure 2.12.

Table 2.1: Energy Calibration Data

Cation State	**Data from Jackels**	**E Calculation**	**E Experiment**
B_1	12.61	7.39	6.496
A_1	14.73	5.27	4.565
A_2	18.55	1.45	1.321

2.3 Analysis

Once appropriate calibration of the experimental parameters has been completed, it is time to consider the data from the standpoint of a physicist, finally working under the premise that the data are accurate representations of the experiment. Tens (often hundreds) of millions of real events must be parsed and interpreted, a daunting task for both the processor of the computer used and for the experimentalist themself.

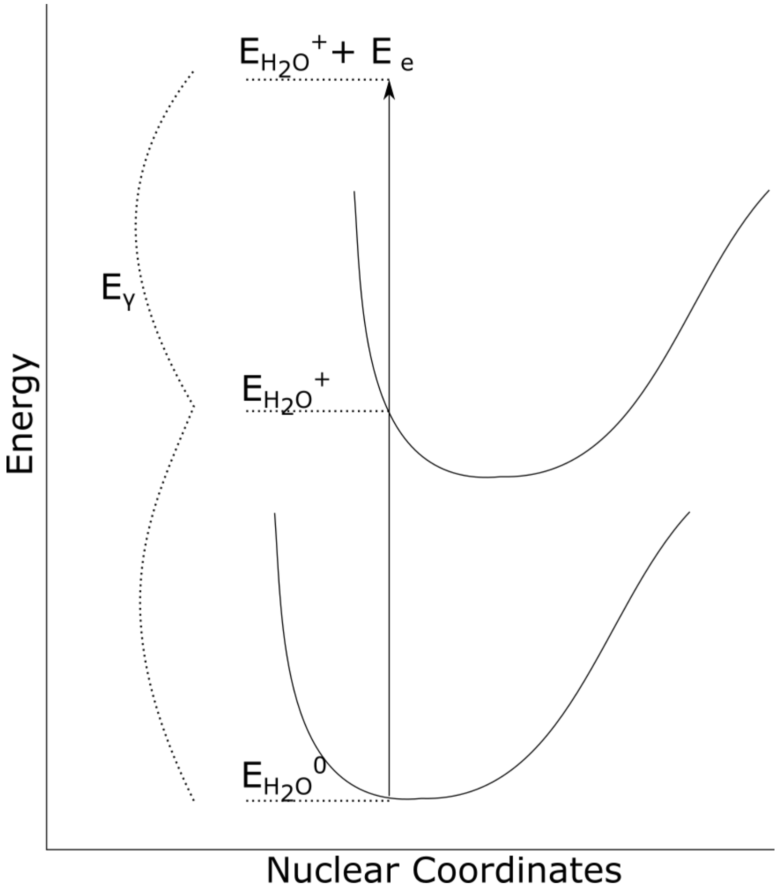

Figure 2.12: Excitation energy beyond the ion potential energy surface is transferred to the liberated electron.

2.3.1 Raw Data and Presorters

The raw data are worth considering to verify the different decay channels sought in the experiment. From the literature, recall that there are several excited states available to H_2O following the impact of a photon above the vertical double-ionization threshold.

$$H_2O^{2+*} \rightarrow H^+ + H^+ + O^* \tag{2.5}$$

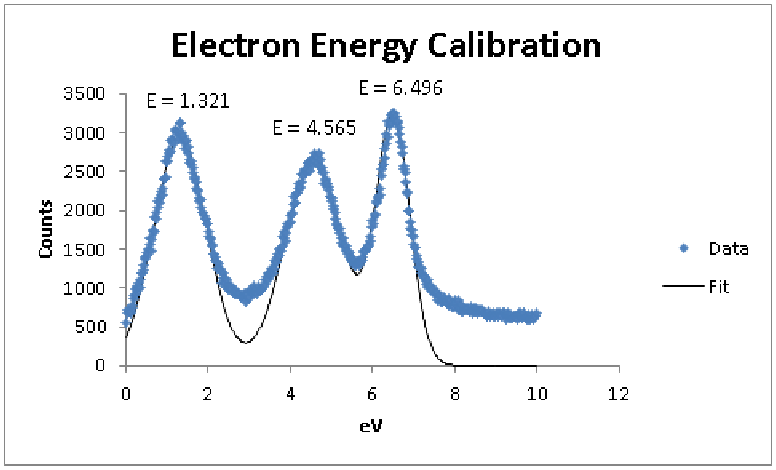

Figure 2.13: Clear peaks emerge in the energy spectrum of photoelectrons ejected by $20eV$ photons.

$$H_2O^{2+*} \rightarrow H^+ + H + O^{+*} \tag{2.6}$$

$$H_2O^{2+*} \rightarrow H^+ + OH^{+*} \tag{2.7}$$

(In each of Equations 2.5 - 2.7 the (*) refers to any of several energetically available excited states or the ground state).

Presorters Any investigation of a particular channel obviously does not require data from another channel - which is precisely the purpose of presorters. Presorters typically operate by setting gates on time-of-flight spectra and by rejecting events that are visibly not part of good event collection, based on their position on the ion detector. (see Fig. 2.14)

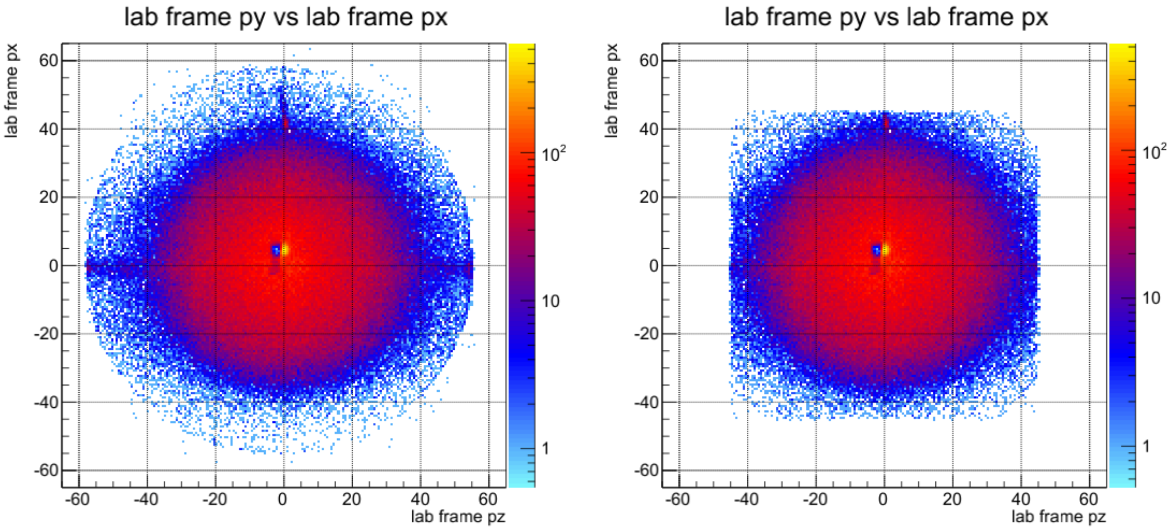

Figure 2.14: In addition to TOF coincidence gates, all ions measured must appear within a position gate.

Consider the geometry of the ion-side of the spectrometer. A particle of charge q and mass m finds itself in a uniform electric field, located in the center of the interaction region. The field exerts a force on the charged particle according to the equation

$$F = q * (-\nabla V) = q \cdot \vec{E} \tag{2.8}$$

until the particle crosses the grid mesh that separates the interaction region from the MCP.

The field in the interaction region performs work on the charged particle according to

$$W = \Delta E = \int_{x_o}^{x_f} F \bullet dx = \int_{x_o}^{x_f} q \cdot \vec{E} \bullet dx \tag{2.9}$$

The electric field is uniform, thus the integral reduces to

$$\Delta E = \Delta x q \cdot \vec{E} \tag{2.10}$$

where Δx and $\vec{E}$ are known.

The Taylor series expansion of the position for the charged particle can be simplified as

$$x(t) = x_o + v_o \cdot t + \frac{1}{2} a \cdot t^2 + ... \tag{2.11}$$

The initial position of the particle, x_o, is arbitrary as usual, but the distance between $x(t)$ and x_o is relevant. The difference is reassigned as Δx. The initial velocity of the particle is a spherically uniform distribution of values - the vector mean of which is 0. The acceleration of the particle is determined by the force and mass of the particle. With equation 2.10 in mind:

$$a = \frac{F}{m} = \frac{q \cdot \vec{E}}{m} \tag{2.12}$$

At last, plugging 2.12 into 2.11 and solving for t yields

$$t = \sqrt{\frac{2\Delta x}{a}} = \sqrt{\frac{2\Delta x}{\frac{q\cdot\vec{E}}{m}}} = \sqrt{\frac{2\Delta x}{\vec{E}}}\sqrt{\frac{m}{q}} \tag{2.13}$$

With emphasis on the value of $\sqrt{\frac{m}{q}}$. All the other quantities are known constants of the experimental apparatus. It is clear, then, that the TOF for ions is *proportional to the square root of the mass-to-charge ratio*:

$$TOF_{ion} \propto \sqrt{\frac{m}{q}} \tag{2.14}$$

Knowledge of this behavior, when combined with Excel simulations, allows the experimentalist to uniquely identify particles in the TOF spectrum based on the quantity $\sqrt{\frac{m}{q}}$. Thus, a presorter can be defined that accepts only particles of charge q and mass m, near a particular time of flight.

Calculation of the electron TOF is notably different than that of the recoil ions. Their charge and mass are fixed, so they cannot be identified using the same parameter that was so useful for the recoil ions. The external magnetic field runs parallel to the length of the spectrometer, and so despite the complexity added to the calculations required for momentum, this $\vec{B}$ has no affect on the TOF of the electron. Despite these complicating factors, at this stage of analysis, *none of it matters*. For a given experimental setup, the TOF for the electrons is *fixed*. As a result, all electrons within a given time window are considered valid when they occur in coincidence with desirable ion measurements.

The basic TOF-coincidence presorter appears thusly as pseudocode:

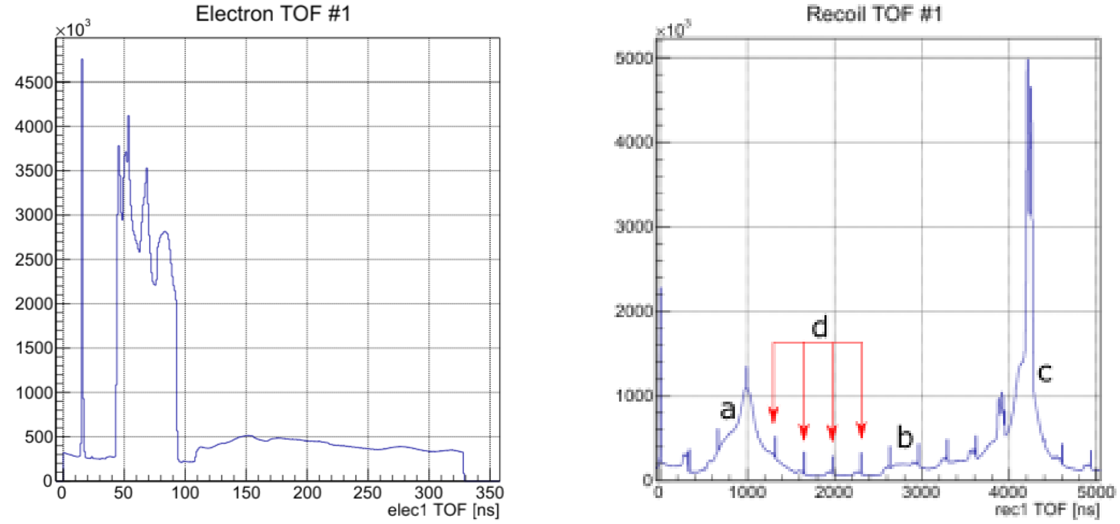

Figure 2.15: Raw Electron TOF spectra (left) and recoil ion TOF spectra (right).

$$\begin{aligned} &\text{if } (TOF_{r-min} < TOF_{recoil} < TOF_{r-max}) \\ &\text{and } (TOF_{e-min} < TOF_{electron} < TOF_{e-max}) \\ &\qquad\qquad\qquad \text{then } event = good \end{aligned}$$

This presorter checks to see if all recoil ions and all electrons appear within their respective predefined time windows. If they do, the data of all the particles is recorded within the presorter channel for further analysis.

Raw Data Raw TOF spectra are the simplest way to isolate unique particle combinations in coincidence, and are used with presorters to assist in parsing the experimental data. The electron TOFs are not unique to the individual reactions, but when taken with different coincidence parameters they are nevertheless different spectra, and are shown here for completeness.

In the raw data shown in 2.15, the maximum electron TOF measured is precisely the ALS bunchmarker, $326ns$. Any electrons collected beyond this window would be indistinguishable from electrons created by the subsequent ALS pulse. Several features in the recoil ion spectrum are of interest, labeled a-d. Feature **a** is the TOF for particles of $m = 1$,$q = 1$, corresponding to hydrogen ions (protons). Feature **b** is a small feature that maps to either $m = 18$,$q = 2$, or $m = 9$,$q = 1$, or is coincidental noise at the appropriate time interval. The presence of a heavy lithium isotope or beryllium atom in the experiment chamber is exceedingly unlikely, so the signal is either coincidental noise or the water dication has been observed. Later analysis of this feature did not yield enough evidence for the dication to warrant discussion. Feature **c** corresponds to $m = 17$,$q = 1$, the OH^+ ions created by the ionization of water. It is likely that O^+ is also built into the broad shoulder to the left of this feature. Feature **d** is a small thin spike showing up periodically across the entire TOF spectrum. These features are easily explained: the distance between them is exactly $326ns$, the time between ALS pulses. A combination of hot gas events and detector noise that have incidentally made it past early efforts at coincidence gating show up in the TOF spectrum.

Validation of the reaction pathway leading to $2H^+$ ions was performed with a electron TOF and recoil TOF coincidence measurement. Electrons falling at TOF 70 ±30ns, in coincidence with ions falling at TOF 1000 ±600ns, were accepted for this channel, and only when exactly 2 electrons and 2 ions were measured with these TOFs. (figure 2.16)

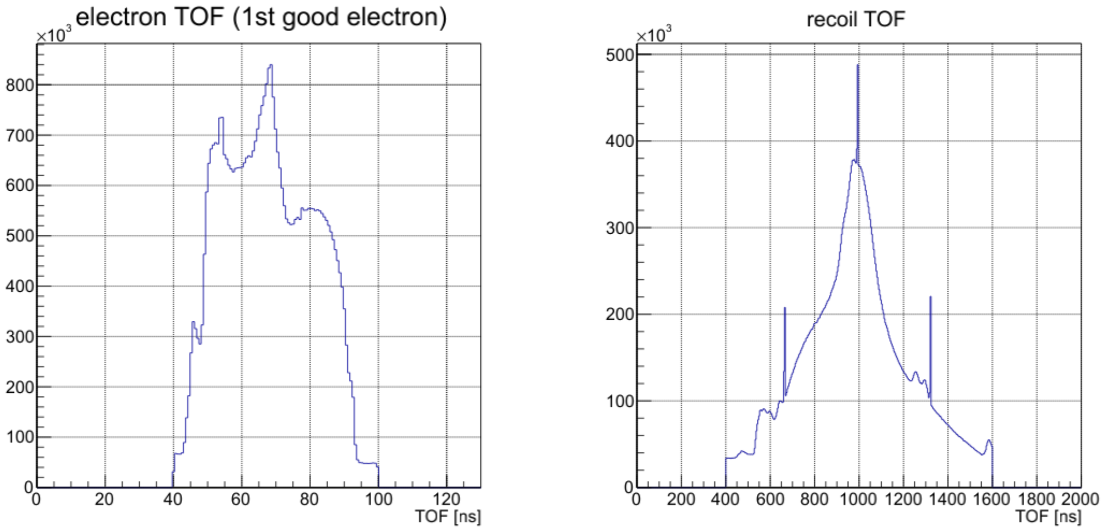

Figure 2.16: Raw Electron TOF spectra (left) and recoil ion TOF spectra (right) for the $2H^+$ reaction pathway.

The reaction leading to $H^+ + OH^+$ was validated using a PIPICO gate. This gate requires a combination of hits with $\frac{mass}{charge}$ ratios of $\frac{1}{1}$ and $\frac{17}{1}$ in coincidence, and within ±100ns of the theoretical center of the parabola. Once again, electrons are accepted at 70±30ns. (figure 2.17)

Presorting data can take many hours. Unfortunately, any mistakes made in the presorter definitions, or in the use of the IPA for calibrating the detectors, will invalidate any results from presorter parsing. However, with properly presorted data, the second phase of LMF2ROOT analysis can take place, wherein the presorted data are paired with reaction channels.

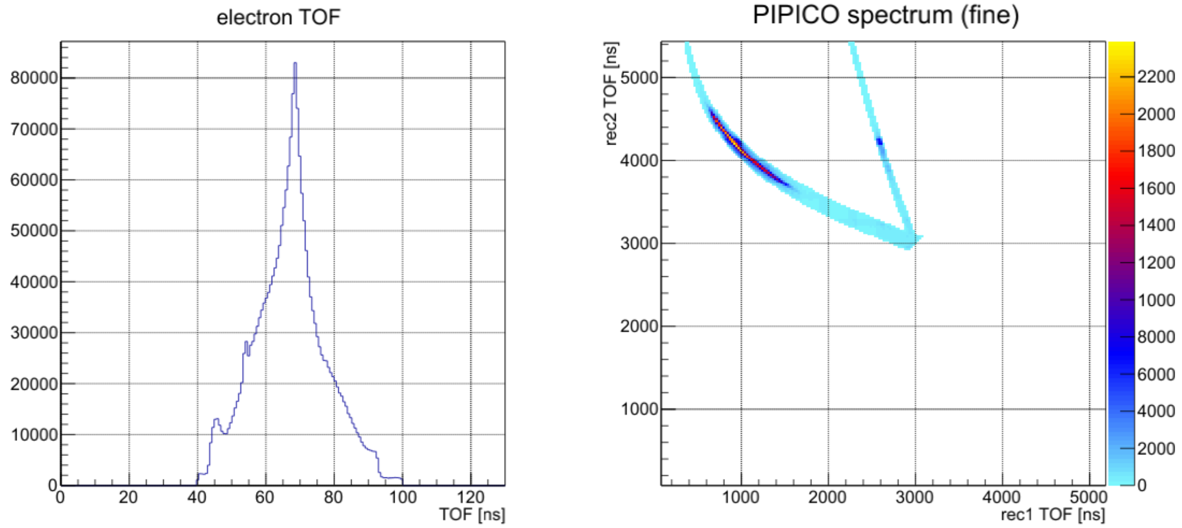

Figure 2.17: Raw Electron TOF spectra (left) and recoil ion TOF spectra (right) for the $H^+ + OH^+$ reaction pathway.

2.3.2 Reaction Channels and ColAHelL

Once the data have been coarsely categorized and reduced by presorters based on particle TOF coincidence, the particles involved in each event are assigned to event channels for treatment with LMF2ROOTs analysis functions. Data analysis channels are given names, integer flags for use in bookkeeping, and each recoil ion involved in the channel is listed with their physical parameters *charge* and *mass*. For each channel, particles are assigned to it by pairing the channel's identification flag to a matching presorter.

The reaction integer assignment is paired with the corresponding presorter flag by LMF2ROOT's analysis code. A series of functions within ColAHelL (Coltrims Analysis Helper Library) are called, using the presorter's data and the reaction's

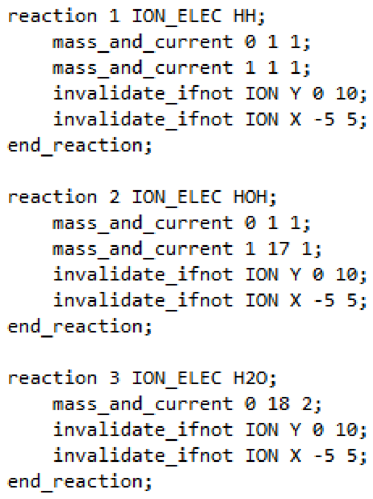

```
reaction 1 ION_ELEC HH;
    mass_and_current 0 1 1;
    mass_and_current 1 1 1;
    invalidate_ifnot ION Y 0 10;
    invalidate_ifnot ION X -5 5;
end_reaction;

reaction 2 ION_ELEC HOH;
    mass_and_current 0 1 1;
    mass_and_current 1 17 1;
    invalidate_ifnot ION Y 0 10;
    invalidate_ifnot ION X -5 5;
end_reaction;

reaction 3 ION_ELEC H2O;
    mass_and_current 0 18 2;
    invalidate_ifnot ION Y 0 10;
    invalidate_ifnot ION X -5 5;
end_reaction;
```

Figure 2.18: Reactions define the masses, charges, and further coarse gating parameters for each experimental channel.

parameters, to calculate the vector momenta of each particle in the event channel. See **Appendix B: Code Samples** for details of the analysis code.

2.3.3 Physical Properties: Momenta, Angles, Energy

The first derived quantity generated by the analysis code is the vector momentum information for a given channel. The kinetic energy of each particle is then calculated simply as

$$KE = \frac{\overrightarrow{p} \bullet \overrightarrow{p}}{2m} \tag{2.15}$$

The angles between vectors are easily calculated using trigonometric relations, e.g. using the law of cosines:

$$\overrightarrow{p_1} \bullet \overrightarrow{p_2} = |p_1||p_2| \cdot cos(\theta) \tag{2.16}$$

Per the name of the analysis framework, LMF2ROOT, the analysis code provides convenient helper functions that will fill ROOT histograms with these derived quantities, in the same way that it created time-of-flight histograms or position density plots for the presorted data. See **Appendix B: Code Samples** for the example code that calculates particle momenta.

2.4 Results

Once LMF2ROOT is properly calibrated, reaction channels have been defined, and the data have been processed, it is time to consider the results of the experiment. The angular distributions of particle momenta, their energies, and any interplay between these variables must be carefully scrutinized for patterns and compared to existing work in the literature.

2.4.1 $H^+ + H^+$ Channel

The vast majority of time and effort has been spent analyzing this reaction pathway, from the earliest learning attempts well into the writing of this thesis.

$$\gamma + H_2O \rightarrow H^+ + H^+ + O^* \tag{2.17}$$

The interpretation of the results has gone through many phases. A vaguely chronological account of the analysis process is the subject of this section. The motivation to focus on this pathway was the capacity of the system be fully oriented in a fixed body reference frame. Fixed frame recoil ion dynamics are often limited along bond breakup axis' (as would be the case in the $H^+ + OH^+$, or in larger molecules). The $H^+ + H^+$ reaction pathway is a 2-ion, 2-bond reaction where the final momenta of the fragments can be measured either directly (as in the case of the hydrogens ions) or via conservation of momentum (the O^* particle). When the unstable H_2O^{2+} dication falls apart, the fragments conserve momentum. Thus, measurement of two H^+ ions gives complete momentum information:

$$\overrightarrow{p}_{H1} + \overrightarrow{p}_{H2} = -\overrightarrow{p}_O \tag{2.18}$$

This information by itself is of no particular interest in the lab frame (figure 2.19). To observe the momentum in the frame of the molecule, a transformation to that frame must be undertaken. The standard practice for molecules of C_{2v} symmetry is to define the molecular z-axis between the two bond axis, with the y-axis coplanar with the molecule and the x-axis defined in the standard way according to a right-handed coordinate system, such that $\hat{x} \times \hat{y} = \hat{z}$.

To that end, the following coordinate system is created using the momenta of the H^+ ions, $\hat{p_1}$ and $\hat{p_2}$.

$$\hat{z} = \frac{\hat{p_1} + \hat{p_2}}{|\hat{p_1} + \hat{p_2}|} \tag{2.19}$$

$$\hat{x} = \hat{z} \times \hat{p_1} \tag{2.20}$$

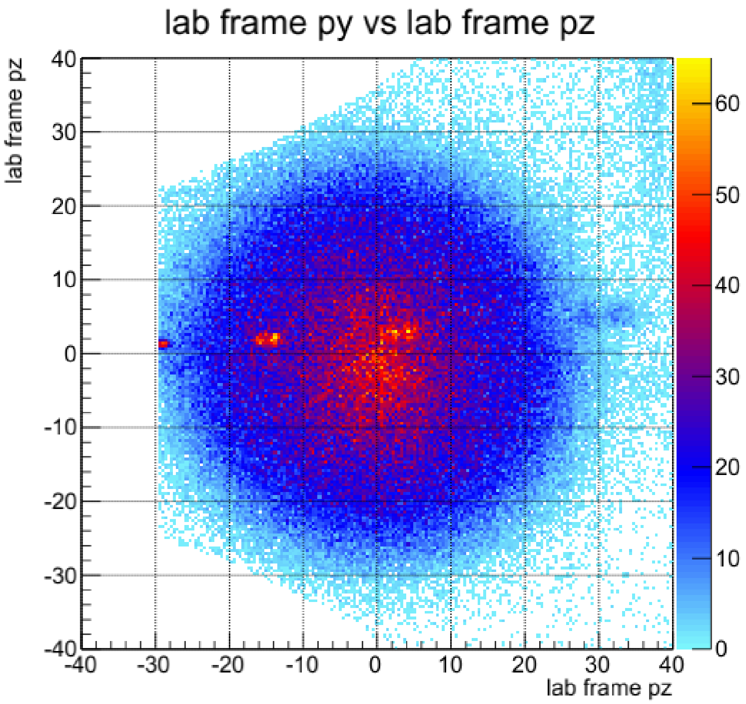

Figure 2.19: Molecules interacting with the photon beam are randomly oriented, leading to an ambiguous Newton sphere of H^+ fragments.

$$\hat{y} = \hat{z} \times \hat{x} \tag{2.21}$$

The resulting molecular frame has a z-axis that always bisects the H^+ momenta, and the molecular plane is defined by the y-axis as desired (figure 2.20).

Before further discussion, it is worth noting that by using the molecular reference frame as defined above, the momentum of the reaction particles has been reduced to two dimensions, from the three dimensions of the lab frame. The electron momenta, to be discussed later, are still three dimensional in this reference frame. These

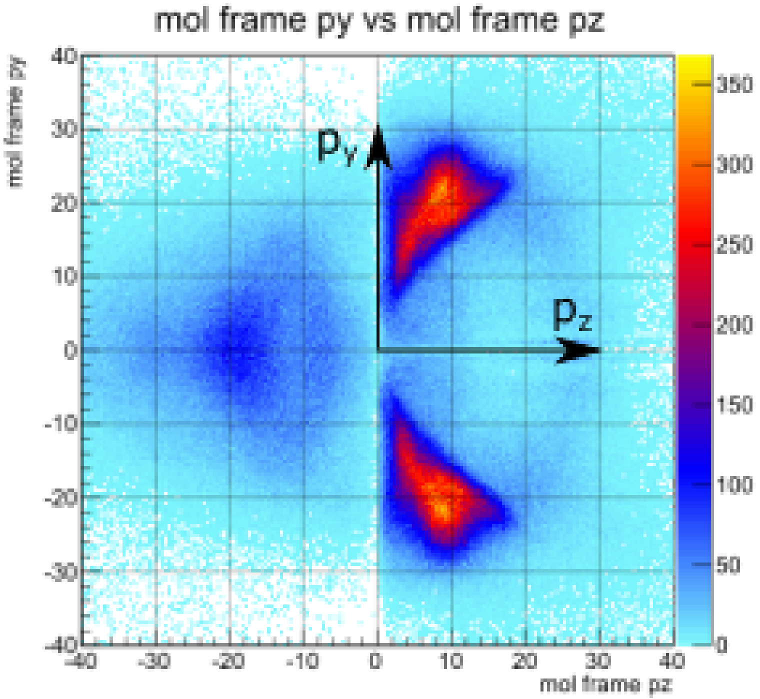

Figure 2.20: Entering a fixed-body molecular frame elucidates molecular dissociation dynamics.

momenta density plots are the first of their kind in momentum spectroscopy. A fully fixed molecular frame has never been measured for cases beyond a single recoil axis.

The naïve expectation is that the molecular frame momenta would be smooth two dimensional distributions, with $|p|$ correlating to the resting bond length of H_2O and $\theta = 104.5^o$, the resting HOH bond angle of ground state water. It is immediately clear that this is not the case: there is structure visible in the momentum density plot, highlighted in figure 2.21. The overlap in the structure is prohibitive with regard to differential analysis gates, but the obvious structure warrants further investigation.

Without a clear idea what the structure represented, a methodical approach was undertaken to find a way to separate the structure in the momentum density plot.

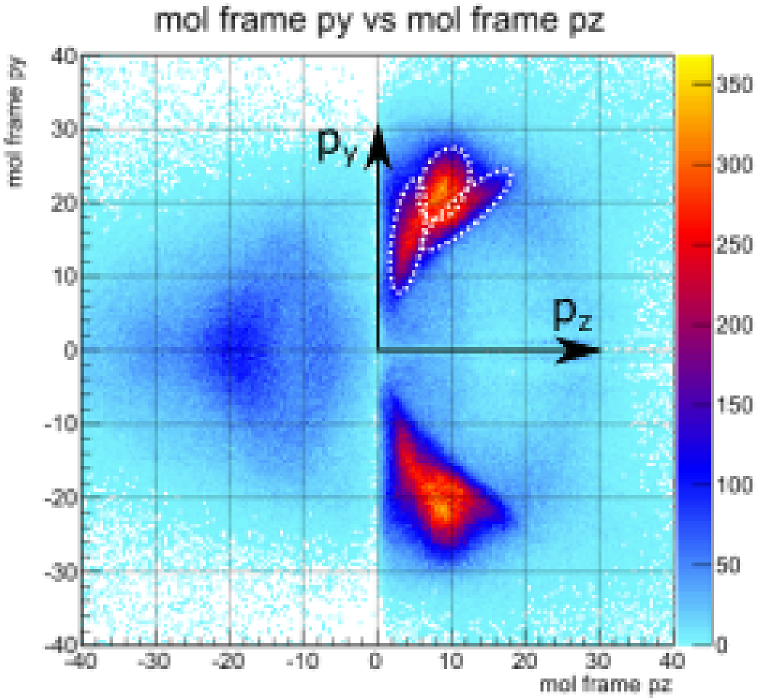

Figure 2.21: Entering a fixed-body molecular frame elucidates molecular dissociation dynamics.

An algorithmic mixing of all interesting quantities, such as total electron energy, KER, bond angle, the sum of the energy totals, and more were plotted and sorted through.

The sum of both electron energies and the KER (figure 2.22) reveals three clear peaks: two of comparable amplitude, and one of substantially smaller amplitude. These peaks were not understood initially, but their importance would be discovered later.

Expanding the one dimensional energy plot into an energy correlation plot between electron energy and KER reveals further structure (2.23). In such a plot, the total energy of the one dimensional histogram corresponds to diagonal lines of

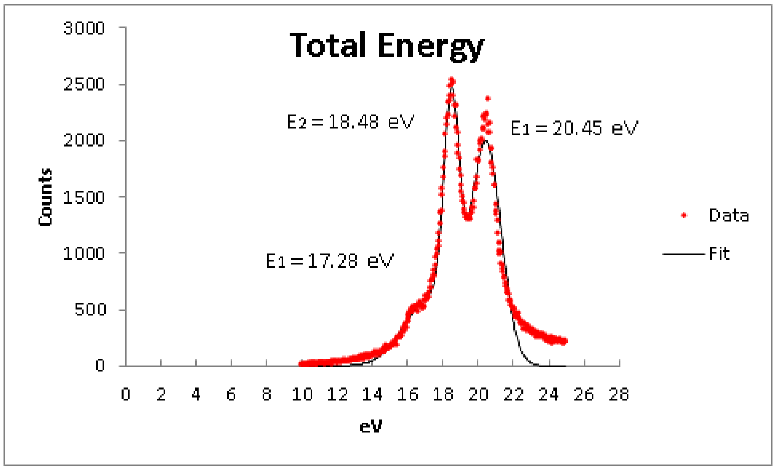

Figure 2.22: The total energy histogram corresponding to the $H^+ + H^+$ channel shows three distinct energy peaks.

$slope = -1$, which is suggestive of energy conservation between the plotted quantities. Initial inspection of this density plot, along with the molecular frame momentum plot and one dimensional total energy histogram, yielded speculation that the water molecule was falling apart into several as-yet unidentified oxygen states.

It was at this stage of the analysis that the majority of the historical literature search was undertaken. It became apparent that the structure observed in the data corresponded in some way to the excited states of the dication, the excited states of the neutral oxygen fragment, or both.

A clear idea of how the different energy and angular quantities related to each other began to form after an invaluable lunch conversation with Dr. C. William McCurdy, Dr. Thomas N. Rescigo, and Dr. Frank Yip. The KER and electron energy sum act, in tandem, as a map between the excited dication state and the excited oxygen fragment. The sum of the energies, electron energy total + KER, has

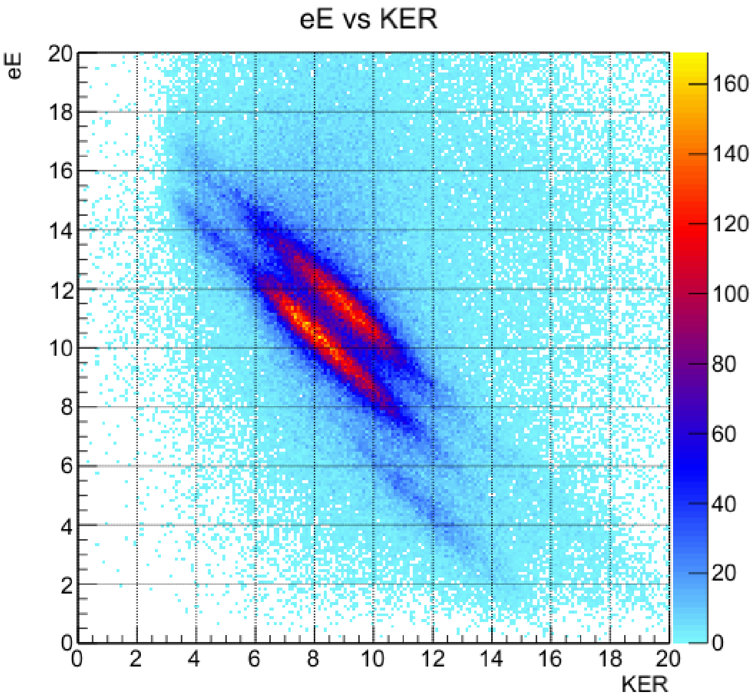

Figure 2.23: A density plot of the electron energy vs KER provides further contrast to the features in the data.

peaks corresponding to three excited states of the oxygen atom. By conservation of energy, it is clear that the energy sum peak with the greatest total energy corresponds to the oxygen state with the least internal energy, i.e., the ^3P ground state. Working down the energy correlation plot, the next lowest energy band corresponds to the ^1D oxygen term, while the lowest band corresponds to the ^1S oxygen term. As a quick point of reference, the NIST Atomic Spectra Database for neutral water energy levels was consulted (figure 2.24).

The correspondence between the NIST energy level data and the $H^+ + H^+$ data was encouraging. A fruitful collaboration between the California theory group and the Auburn experimentalists lead to calculations of several limited projections

Table 2.2: Oxygen Energy Separation

Terms	**NIST Data (eV)**	**Experiment (eV)**
^1D - ^3P	1.967	1.97 ± 1.30
^1S - ^3P	4.190	3.17 ± 2.32

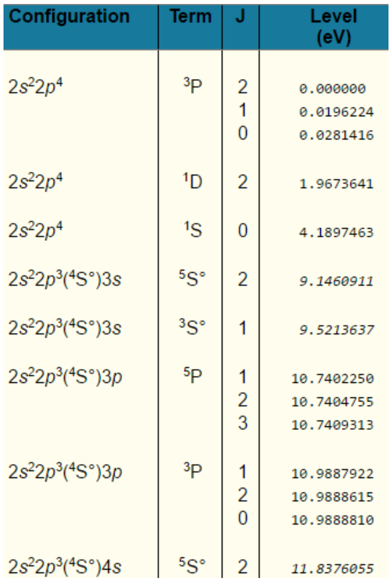

Configuration	Term	J	Level (eV)
$2s^22p^4$	^{3}P	2	0.000000
		1	0.0196224
		0	0.0281416
$2s^22p^4$	^{1}D	2	1.9673641
$2s^22p^4$	^{1}S	0	4.1897463
$2s^22p^3(^4S°)3s$	^{5}S°	2	9.1460911
$2s^22p^3(^4S°)3s$	^{3}S°	1	9.5213637
$2s^22p^3(^4S°)3p$	^{5}P	1	10.7402250
		2	10.7404755
		3	10.7409313
$2s^22p^3(^4S°)3p$	^{3}P	1	10.9887922
		2	10.9888615
		0	10.9888810
$2s^22p^3(^4S°)4s$	^{5}S°	2	11.8376055

Figure 2.24: Data from NIST showing the energy separation between neutral oxygen terms.

of energetically accessible water dication potential energy curves, generated by the theory team. These corresponded to many of the dication curves cited in some of the historical literature, another promising tie to previous work in the study of the dication.

Taking the $2H^+$ reaction pathway as a premise, the H_2O^{2+} ion is certainly unstable. For non-linear molecules, there are $3N - 6 = 3$ degrees of freedom. These are:

1. Bending of the bond angle

2. Stretching of bond A

3. Stretching of bond B

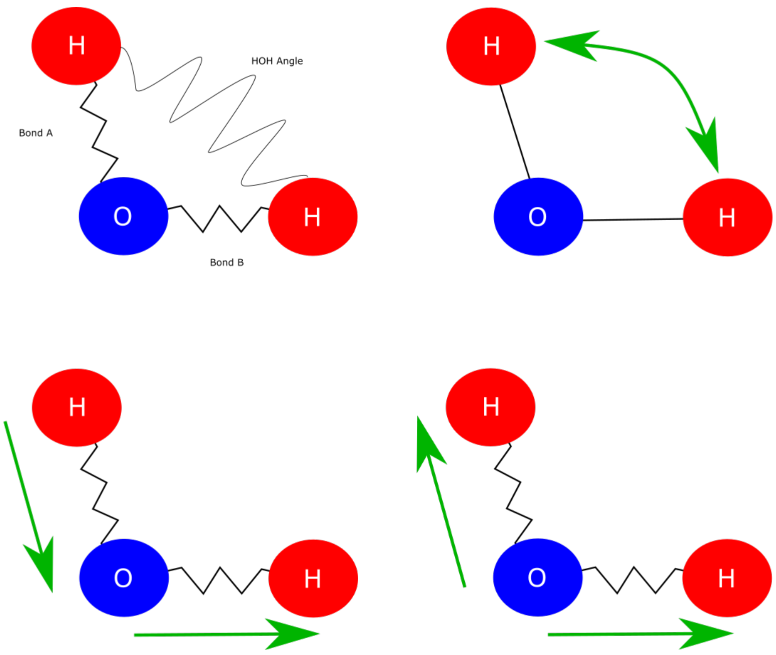

Figure 2.25: The water molecule, which possesses C_{2v} symmetry, has three modes of oscillation. Top Left: Vibrational degrees of freedom. Top Right: HOH bond bending. Bottom Left: Asymmetric Stretch. Bottom Right: Symmetric Stretch.

Visualization of a potential energy surface containing three degrees of freedom is convoluted at best; calculation of such a surface is challenging, but not impossible. For simplicity of calculation, and to help with the analysis process, it is valuable to consider simplified versions of the potential energy surface. One such simplification is the so-called ”symmetric stretch”, wherein the bond angle is fixed and the two OH bonds are stretched together, such that vibrational motion is symmetric and, once coupled, one dimensional (see figure 2.25, bottom right).

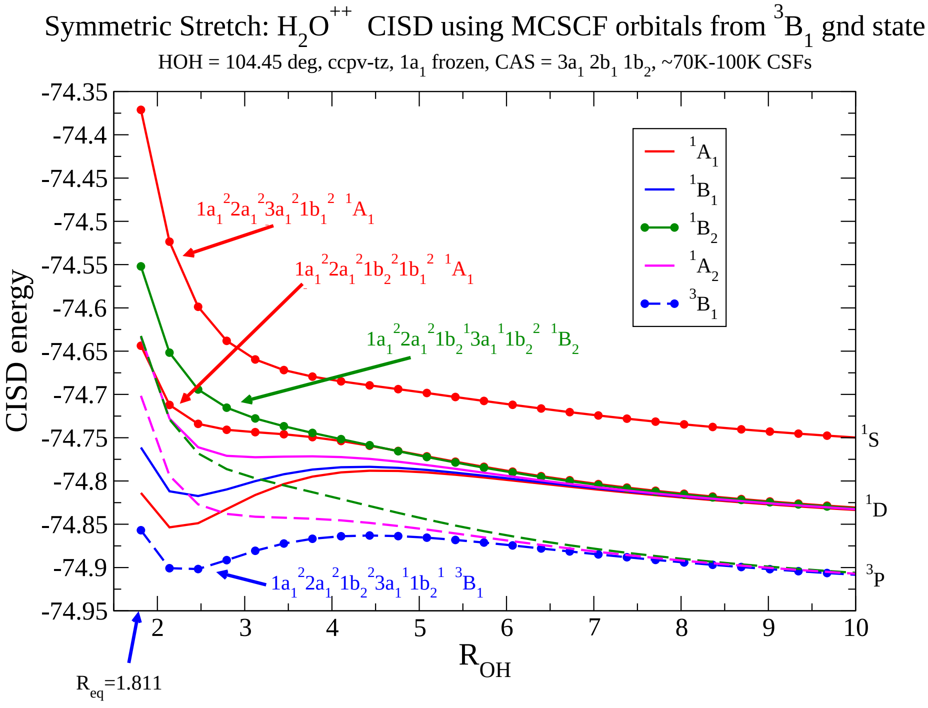

Figure 2.26: Potential energy surface projections of the nine lowest lying dication states with fixed bond angle and equal bond stretching.

The potential energy curve calculations in the symmetric stretch regime (2.26) begin around 1.811 Bohr, roughly the resting bond length of the water neutral. These potential energy curves represent projections of the potential energy surface under the aforementioned conditions, i.e., with symmetric bond stretching and a fixed HOH bond angle of 104.45^o. The individual electronic terms are listed for four of the curves. The curves for all the energetically available dication states are shown, and are traced to their semi-asymptotic limits around 20Å. The varying limits of these curves all converge to three energies, corresponding to oxygen terms: ^3P, ^1D, and ^1S. Some of these curves are clearly repulsive in the region of the resting bond length of ground state water, around 0.96Å. Other curves exhibit local minima or nearly flat local gradients, corresponding to barely repulsive or even non-repulsive behavior. This corresponds to states that cannot dissociate via a symmetric elongation of the OH bonds. Instead, these states must either bend along the HOH bond angle, or must asymmetrically stretch in order to dissociate. Figure 2.26 suggests that dication potential energy surfaces that are clearly repulsive in the symmetric stretch regime are likely to dissociate into the $H^+ + H^+$ channel.

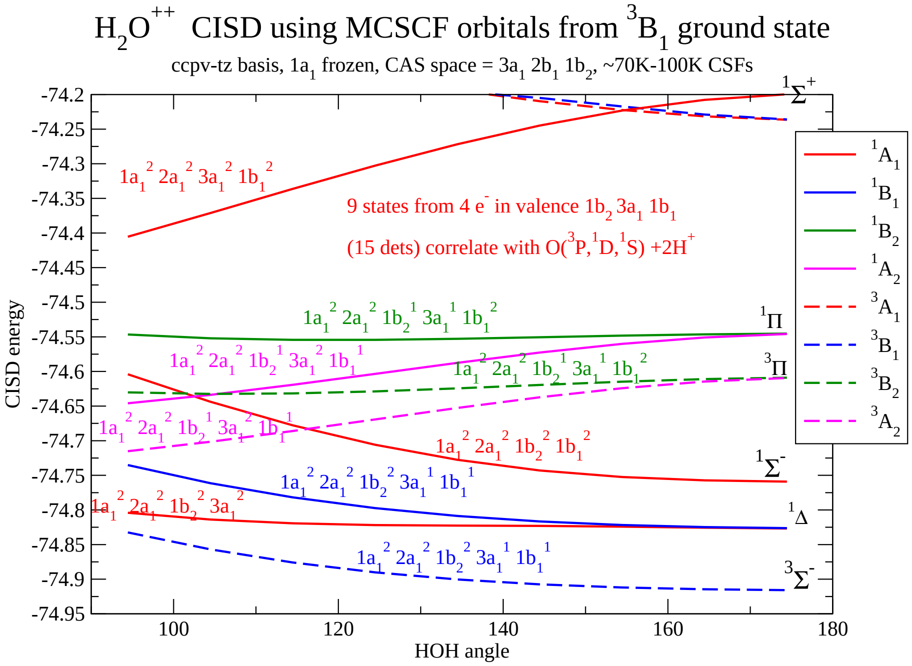

Figure 2.27: Potential energy surface projections of the nine lowest lying dication states with fixed OH bond lengths.

A similar one dimensional projection of the dication potential energy surface can be made for the special case when the two OH bonds are held at a fixed length (2.27). These curves suggest that some states are energetically inclined to expand or squeeze the bond angle; some also appear to have small or insignificant bending gradients. It is worth noting that in this projection, the asymptotic behavior of the molecule is entirely unclear. Any dissociation process necessarily involves elongation of the bonds. However, the potential energy surface is smooth and continuous, and so the projection is at least moderately useful in considering the behavior of the molecule immediately after population of each dication curve.

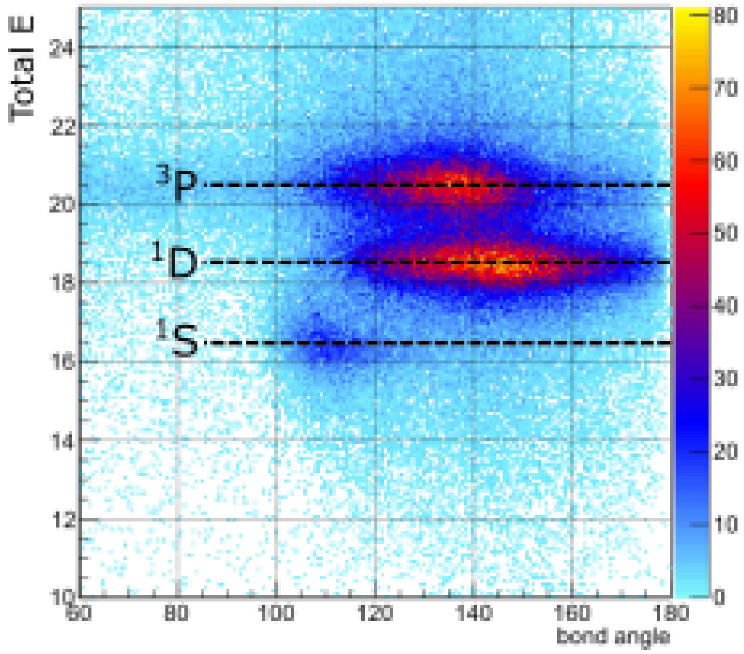

Figure 2.28: The energy bands visible in the Total Energy vs HOH Bond Angle plot correspond to the asymptotic oxygen neutral terms discussed previously.

In figure 2.28, striped features corresponding to the known oxygen terms following dissociation are clearly shown and, verifying the relationship predicted in the potential energy surface projections, each of these energies has a somewhat unique angular distribution signature. The potential energy surface projections contain more detail than 2.28, however. Each water dication state should have a unique KER, electron energy, and angular signature. These three signatures in combination should serve to uniquely identify the dication states.

Closer consideration of the electron energy as a valid variable reveals that it is superfluous. Since the electron energy and KER sum to the total system energy, only two of these values are interesting, the third merely being some linear combination of the other two. However, tracking down the unique signatures of the water dication states is difficult due to the nearness of their KERs, total energies, and bond angles. Often, looking at a reverse problem that is redundant may lead to a new outlook that leads to a breakthrough.

After elimination of the electron energy as a variable (due to its coupling to KER and total energy release), the next density plot to investigate one contrasting KER and HOH bond angle 2.29.

Figure 2.29 reveals several features. The KER of a given reaction depends, at least in part, on the bond length at the time of dissociation, while the bond angle of the fragments must correspond to the bond angle at the time of dissociation. This density plot, then, should somewhat resemble a 2D potential surface heat map, with the symmetric stretch bond length transformed into KER and the bond length exaggerated by the Coulomb potential of the exiting H^+ fragments. There are clearly

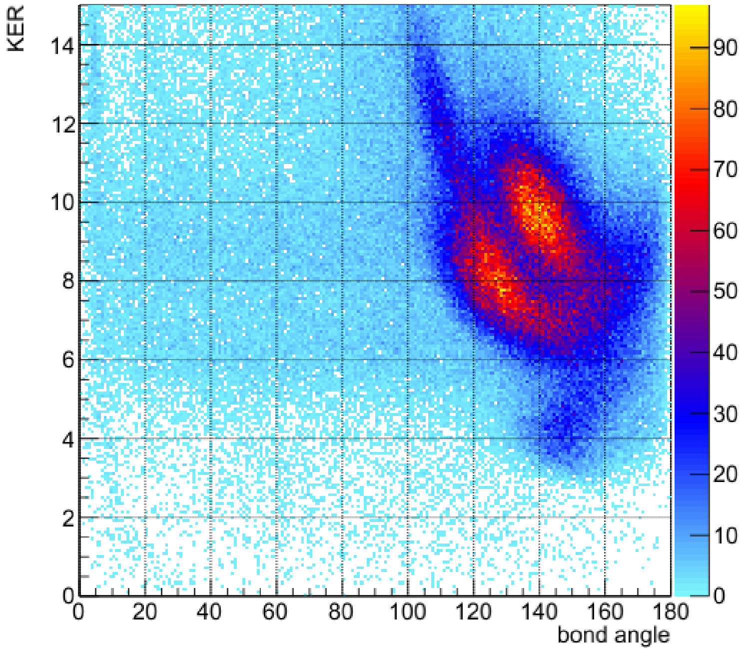

Figure 2.29: Islands appear in the KER vs Bond Angle density plot, which add contrast to the angular distributions of some of the potential dication states.

not nine separate features in 2.29, however, so further differential gating is required to isolate the different state signatures.

There is no ambiguity in applying a total energy gate to narrow the data to states correlating asymptotically to ^3P, ^1D, and ^1S oxygen terms. Gating on the total energy and investigating the KER vs Bond Angle density plot reduces the number of potential dication states involved in generating the features.

Each potential surface with a common asymptotic oxygen term has a unique KER signature, as shown in figure 2.26. Any density plot featuring the KER on an axis and gated on the oxygen term final energy gates should serve to isolate each dication state. The results of these gates are summarized in table 2.3. It is believed

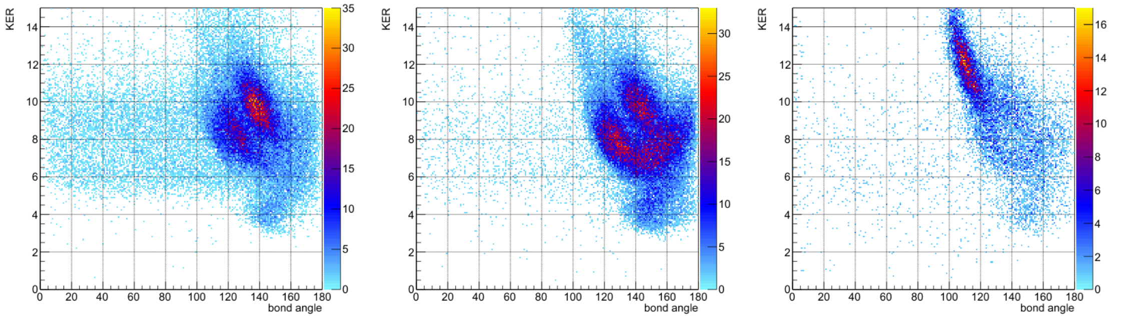

Figure 2.30: KER vs Bond Angle for ${}^3P$(left), ${}^1D$(center), and ${}^1S$(right) total energy gates.

that eight of the nine dication states featured in this analysis will dissociate into the three body channel.

Table 2.3: Dication State Quantities

Dication State (C_{2v})	**KER (eV)**	**Dis. Angle (deg)**	**O Term**
${}^3B_1$	4 ± 1	145 ± 5	${}^3P$
${}^3A_2$	8 ± 1	125 ± 5	${}^3P$
${}^3B_2$	9.5 ± 1	140 ± 5	${}^3P$
${}^1B_1$	4 ± 1	150 ± 5	${}^1D$
${}^1A_2$	7.5 ± 1	153 ± 5	${}^1D$
$2\ {}^1A_1$	7.8 ± 1	127 ± 5	${}^1D$
${}^1B_2$	9.7 ± 1	142 ± 5	${}^1D$
$3\ {}^1A_1$	12 ± 1	109 ± 5	${}^1S$

The KER values for each dication dissociating into three body channels have been calculated by the Berkeley theorists and are shown in table 2.4.

If the calculations match the KERs found in the data, it is believed that the unique signatures for each dication state have been found. It is worth considering that the KER calculations were performed under the symmetric stretch assumption, which

Table 2.4: Dication State Energy Calculations

Dication State (C_{2v})	**KER (eV)**
$^3B_1$	3.02
$1\ ^1A_1$	2.07
$^1B_1$	3.51
$^3A_2$	7.26
$2\ ^1A_1$	6.69
$^3B_2$	9.17
$^1B_2$	9.30
$^1A_2$	7.06
$3\ ^1A_1$	11.76

fixes the bond angle at the equilibrium angle of the water molecule. If the molecule dissociates at a different bond angle, such KER calculations could be inaccurate. A final table combining the theoretical and experimental results concludes this portion of the analysis.

Table 2.5: Summary of Dication State Energies

Dication State (C_{2v})	**Expt. KER (eV)**	**Theory KER (eV)**	**O Term**
$1\ ^1A_1$	(not observed)	2.07	^3P
$^3B_1$	4 ± 1	3.02	^3P
$^3A_2$	8 ± 1	7.26	^3P
$^3B_2$	9.5 ± 1	9.17	^3P
$^1B_1$	4 ± 1	3.51	^1D
$^1A_2$	7.5 ± 1	7.06	^1D
$2\ ^1A_1$	7.8 ± 1	6.69	^1D
$^1B_2$	9.7 ± 1	9.30	^1D
$3\ ^1A_1$	12 ± 1	11.76	^1S

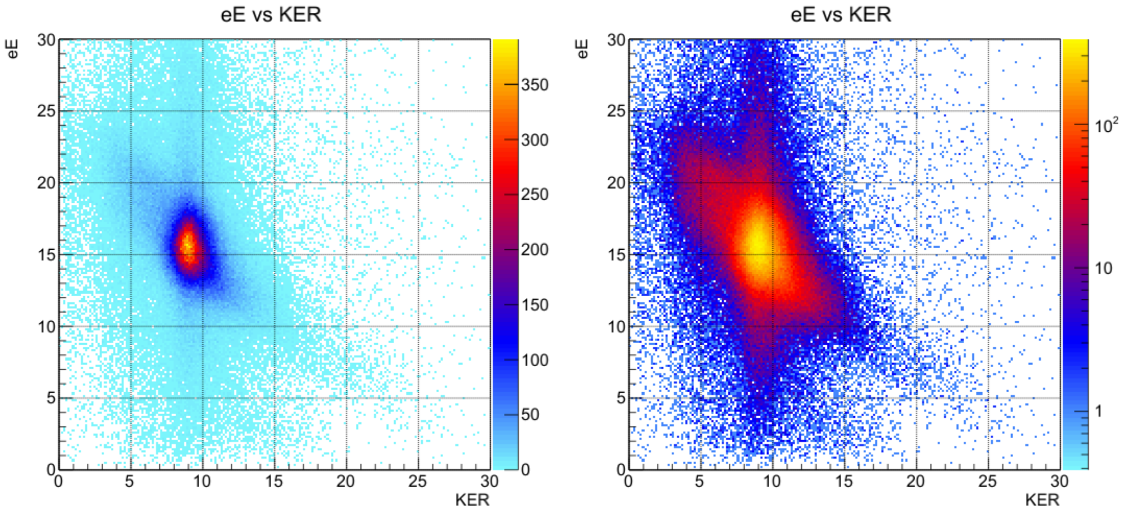

Figure 2.31: Electron Energy vs KER for the two-body breakup channel. The figures are the same data, with the right side plotted in a log(z) format.

2.4.2 $H^+ + OH^+$ Channel

The OH^+ fragment contains a more complex electronic structure than atomic oxygen and, as a diatomic molecule, also has a vibrational degree of freedom. As a result, there are significantly more final states available to the reaction fragments in the $H^+ + OH^+$ channel. In contrast, before the dication dissociates, it has fewer reaction coordinates to consider; the system is quasi-diatomic, with the OH fragment acting as a pseudo-atom in such a framework. With these differences in mind, it was expected that the total energy distribution of the fragments would be broad. Following a similar investigative strategy as in the $H^+ + H^+$ channel, the electron energy was plotted against the KER.

Two features stand out in figure 2.31. The first is a diagonal stripe of constant total energy around 26eV. The second feature is one without an analogue in the H^+

+ H^+ channel: a vertical stripe corresponding to reactions of roughly constant KER around 9 eV. Viewing the density plot in a log scale emphasizes that the feature of constant total energy is broad. The diagonal and vertical features overlap each other, so a proper gate on this plot is not immediately clear.

The density plot of the individual electron energies helps to distinguish these overlapping states.

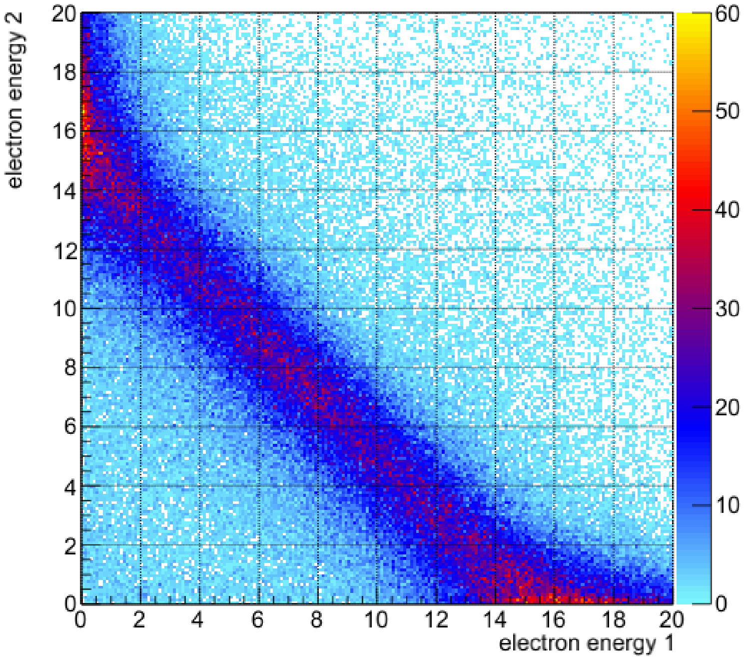

Figure 2.32: The electron energy correlation in a density plot. The strong features along the axis indicate highly asymmetric energy sharing between electrons.

Figure 2.32 has two features. In the first, the electrons share energy evenly, forming the downward diagonal stripe. In the second, islands of highly asymmetric energy sharing are visible on each of the axis'. Typically, highly asymmetric energy sharing in molecular ionization corresponds to either auto-ionization or auger decay.

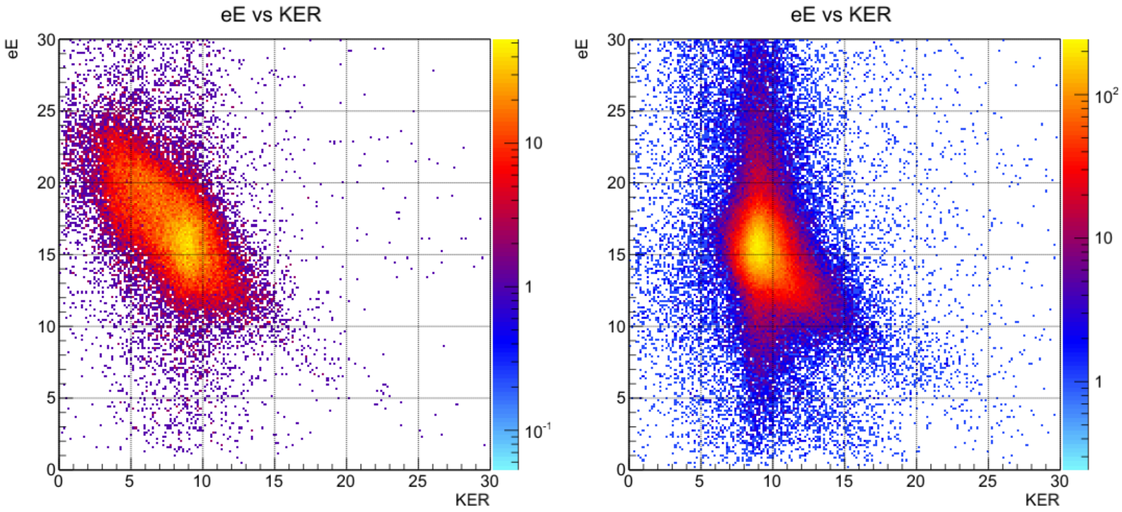

Figure 2.33: The electron energy vs KER is plotted for asymmetric electron energy sharing (left) and symmetric sharing (right).

However, these mechanisms are highly unlikely in this case. A likely source of this energy asymmetry is described in a paper by Colgan and Pindzola [12]. In [12], the authors found that for an excited helium atom in a triplet state, double ionization can lead to asymmetric energy sharing between electrons. It is possible that a similar mechanism could exist in the double photoionization of water.

Gating on the electron energy asymmetry and returning to the electron energy vs KER density plot validates this line of reasoning. Constraining the figure to cases where the electron energy is evenly distributed corresponds to dication states populating the vertical stripe, and cases where the electron energy is asymmetrically distributed partially isolates the diagonal energy feature. The resulting density plots are shown in 2.33.

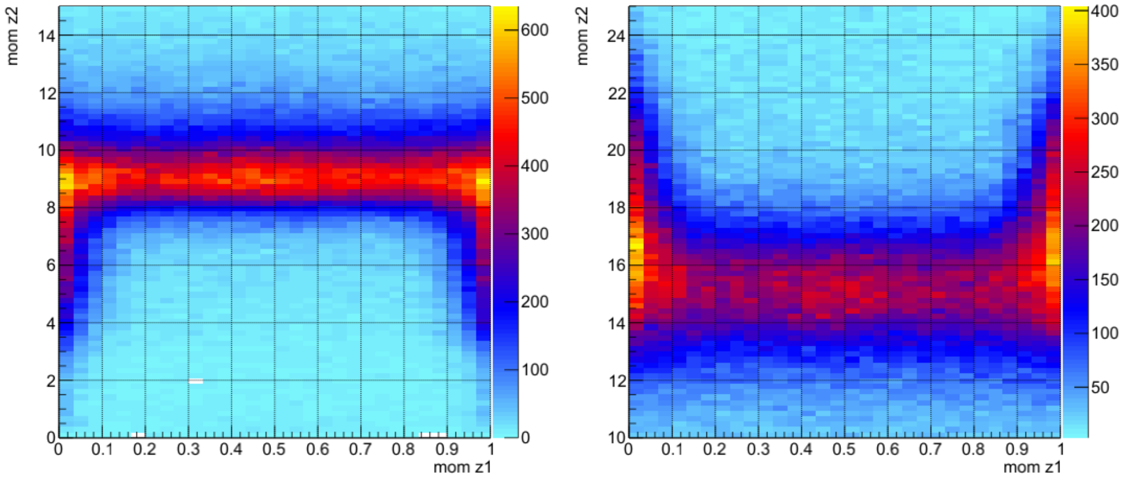

Figure 2.34: The KER (left) and total electron energy (right) are plotted against the electron energy sharing ratio.

Further detail is revealed by seeking the relationship between the asymmetric energy sharing and other variables, i.e. the KER and electron energy sum. Figure 2.33 shows these relationships in density plots.

The vertical features along the sides of figures 2.34 correspond to the asymmetric energy sharing case, while the horizontal stripe corresponds to symmetric energy sharing. These figures suggest that the asymmetric energy sharing corresponds to a dication state of large total electron energy release, e.g., a low lying dication state. Furthermore, the asymmetric energy sharing corresponds to a dication state with a relatively low KER, e.g., a gradual potential energy curve.

The paper by Gervais *et al* [7] was extremely informative in assigning dication states to their likely reaction pathways. Their calculations list a plethora of energetically available asymptotic states for the water dication. Those states are reproduced in table 2.6.

Table 2.6: Calculations from Gervais *et al*

C_s **S**	C_{2v} **S**	C_{2v} **C**	OH^+	**ΔE** H_2O **(eV)**	E_{elec} (eV)
X^3A''	$^3B_1$	$(3a_11b_1)^{-1}$	$X\ ^3\Sigma^-$	40.33	16.67
$2^3A''$	$^3A_2$	$(1b_21b_1)^{-1}$	$A\ ^3\Pi$	44.32	13.68
$1^3A'$	$^3B_2$	$(1b_23a_1)^{-1}$	$A\ ^3\Pi$	46.26	10.74
$1^1A'$	$^1A_1$	$(1b_1)^{-2}$	$a\ ^1\Delta$	41.37	15.63
$1^1A''$	$^1B_1$	$(3a_11b_1)^{-1}$	$a\ ^1\Delta$	42.84	14.16
$2^1A'$	$^1A_1$	$(3a_1)^{-2}$	$b\ ^1\Sigma^+$	46.03	10.97
$2^1A''$	$^1A_2$	$(1b_21b_1)^{-1}$	$^1\Pi$	46.02	10.98
$3^1A'$	$^1B_2$	$(1b_23a_1)^{-1}$	$X\ ^3\Sigma^-$	48.36	8.64

Table 2.7: Calculations performed by Gervais *et al* mapping the water dication in two symmetry states, C_S and C_{2v}, to OH^+ states. The energy above the water ground state and the corresponding electron energy for a 57 eV photon are in the rightmost two columns.

Gervais also performed classical trajectory calculations to anticipate the branching ratios for the eight lowest lying dication states. The only triplet state that regularly dissociates into $H^+ + OH^+$ is the $^3B_1$ state, which dissociates to the OH^+ ground state. The data for the water experiment anticipates such a dissociation pathway would have around 18 eV electron energy, and 7.5 eV KER, in slight disagreement with Gervais' numbers.

Two singlet states of the water dication had large branching ratios feeding into the $H^+ + OH^+$ channel: the lowest lying $^1A_1$ and the $^1B_1$. The second lowest lying $^1A_1$ was expected to yield roughly a two-to-one ratio of the three body break up to the two body one. The branching ratios as calculated by Gervais are given in (the table)

Table 2.8: Gervais Branching Ratios

	$^3B_1$	$1\ ^1A_1$	$^1B_1$	$2\ ^1A_1$	$^1A_2$	$^3A_2$	$^3B_2$	$3\ ^1A_1$
OD^+	86	74	87	67	1	1	3	4
OH^+	10	24	7	¡1	0	0	0	0
Three-body	4	2	6	32	99	99	97	96

It is unclear at this stage whether or not a symmetric molecule (H_2O) would behave much differently than the asymmetric version (HDO). Gervais' work is used here as it is as close to a relevant treatment to the current data as exists in the literature to date. A specific treatment for the water experiment would, of course, be preferential.

2.4.3 Summary of the Dication Mapping Process

Following excitation by a 57 eV linearly polarized photon, the water molecule is doubly ionized and can populate any of nine dication states. The dication is unstable, and the internal forces of the molecule force its components to rearrange themselves, leading to dissociation. There are qualitatively two ways this can happen. If the potential energy surface causes the OH bonds to stretch symmetrically, both bonds are broken and the dication breaks up into three recoil particles: $2H^+ + O$. If the potential energy surface causes the OH bonds to stretch asymmetrically, then only the bond with excessive $H-OH$ bond length is broken, and the dication breaks up into two recoil particles: $OH^+ + H^+$.

Each of the nine potential energy surfaces exist at energies ranging from roughly $39-50$ eV above the neutral water ground state. The photoelectrons carry away excess energy above the dication energy surfaces, and thus the nine surfaces have nine unique electron energy values. Each of these surfaces can dissociate in either the two body or three body asymptotic limit. Each transition from a dication state to one of the two recoil fragment asymptotes has a ΔU associated with the transition, which manifests as kinetic energy distributed across the fragments. Many of the dication potential surfaces overwhelmingly dissociate into only one of the decay channels, by ratios of 9-to-1 or larger. Some of the dication surfaces feed into both decay channels in nearly equal amounts.

2.5 Electron Correlation

For both the two body and three body dissociation pathways, the correlation between photoelectrons is of particular interest. Electron correlation is at the forefront of molecular ionization research; indeed, the theoretical support for the double photoionization of water is likely several months away as of the writing of this thesis. Without a good theoretical reference frame, the electron correlation effects are offered here for the sake of thoroughness and as potential motivation for future analysis or experiments.

2.5.1 $H^+ + H^+$ Electron Correlation

In the three-body case, the water dication can be oriented in its molecular frame via conservation of momentum. As a result, the relationships between the orientation of the molecule, the polarization of the incident photon, and the angular distribution of the photoelectrons can be investigated.

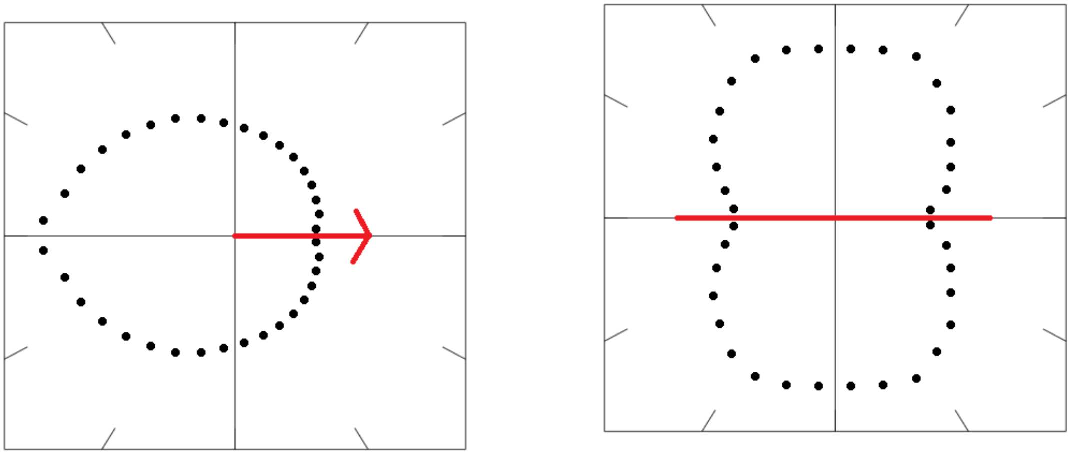

(a) The angle between the photoelectrons, normalized for solid angle. The red arrow represents 0^o.

(b) The angle between the photoelectrons and the polarization axis of the incident photon beam. The red bar represents the polarization axis.

Figure 2.35

Figure 2.35 displays the angles between the two photoelectrons (left) and between the photoelectrons and the polarization axis (right). The angle between the photoelectrons corresponds to the so-called "knock out" model of double photoionization. In quantum mechanics, the photon is a one electron operator, and must therefor only act on a single electron. One interpretation of double photoionization is that, upon excitation by a photon, the primary photoelectron collides with another electron in the molecule, depositing energy and liberating the impacted electron from its bonding orbital. The collision is considered quasi-classically like a billiard ball collision. The angle between the two electrons, then, would be nearly 90^o before considering the electric repulsion. The expected angular distribution is then one that grows in probability toward the electrons exiting the molecule at 180^o from each other, as they would in the asymptotic limit of the Coulomb potential. Gating on the various final asymptotic states (Oxygen ^1S, ^1D, ^3P) or on the intermediate dication states (table 2.5) has no effect on this angular distribution.

The distribution of electrons from the polarization axis appears to take the shape of a d-wave, with the electron emission amplitudes perpendicular to the polarization axis. Without input from a theoretical framework for the angular distribution of valence photoelectrons, there has not yet been significant speculation as to the cause of this distribution.

Perhaps the most unique ability of the COLTRIMS technique is the ability to generate MFPADs: molecular frame photoelectron angular distributions. Electron correlation is at the forefront of modern molecular physics, and the COLTRIMS apparatus is uniquely capable in studying these data. Figure 2.36 suggests that the

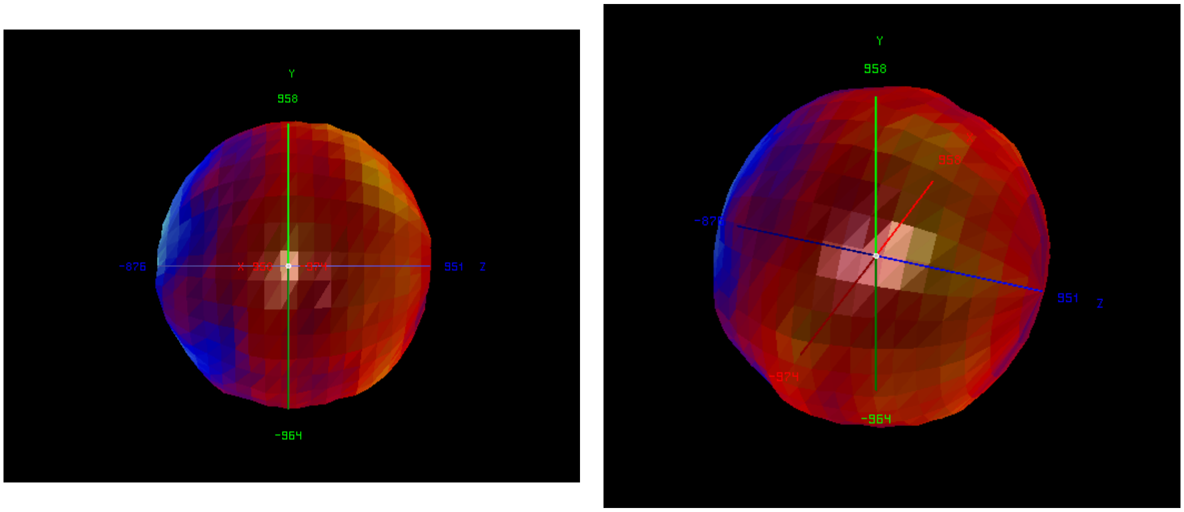

Figure 2.36: A molecular frame photoelectron angular distribution (MFPAD) shown looking into the plane of the molecule (left), and from a diagonal for perspective (right). The heat map ranges from 800 events (light blue) to 1100 events (yellow).

photoelectrons tend slightly to exit in the $2H^+$ hemisphere of the dissociating water molecule.

A variation on the MFPAD is to construct a similar 3D heatmap of the polarization axis in the molecular frame, identifying the orientation of the molecule relative to the light source at the time of dissociation. Such figures are shown in 2.37.

Analysis of figure 2.37 suggests that the molecule is more inclined to photodissociate when the polarization axis of the incident photon aligns with either the plane of the molecule, or perpendicular to it. Rigorous justification this is forthcoming with the work of the Berkeley theory group. However, alignment of the polarization axis with the largest molecular orbital probability density locations is a reasonable qualitative explanation.

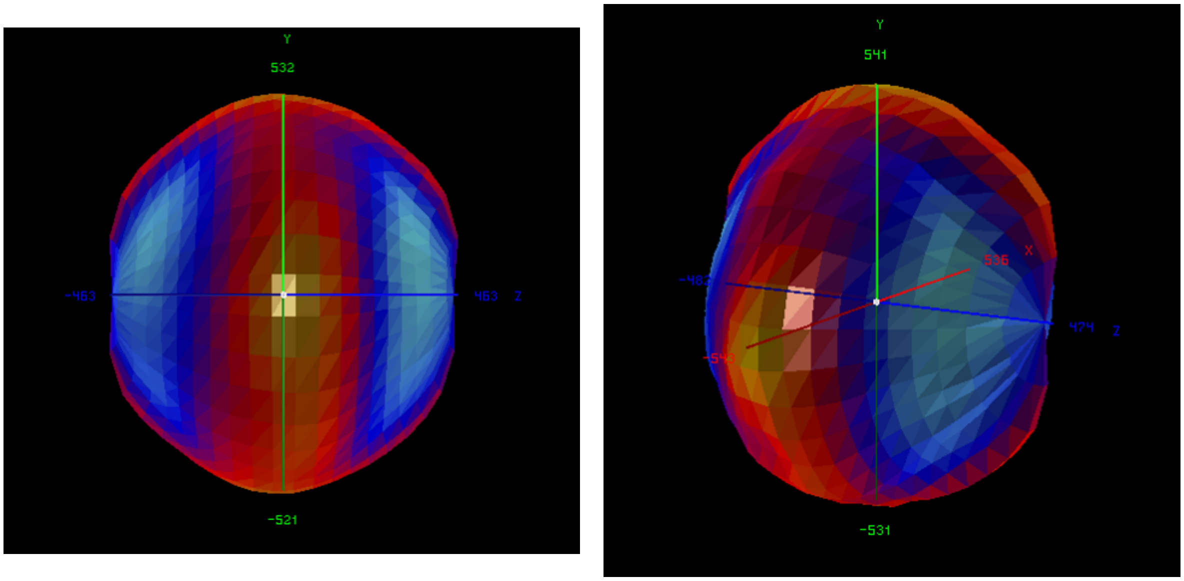

Figure 2.37: A three dimensional heat map of the polarization vector in the molecular frame looking into the plane of the molecule (left) and with a diagonal perspective (right).

2.5.2 $H^+ + OH^+$ Electron Correlation

The two-body reaction pathway does not allow the unique orientation of the water dication before dissociation. However, the axis of the quasi-diatomic breakup can be fixed to investigate the relationship between the polarization of the incident photon and the angular distribution of the photoelectrons.

As was noted in the identification of dication states leading to the two body breakup, the electron energy sharing comes in two species: symmetric and asymmetric. In the three body breakup, the electrons symmetrically shared energy and the electron-electron correlation was attributed to the quasi-classical "knock out" description, wherein the incident photon liberates one electron and that photoelectron collides with another electron, sharing energy and recoiling in a billiards-like fashion.

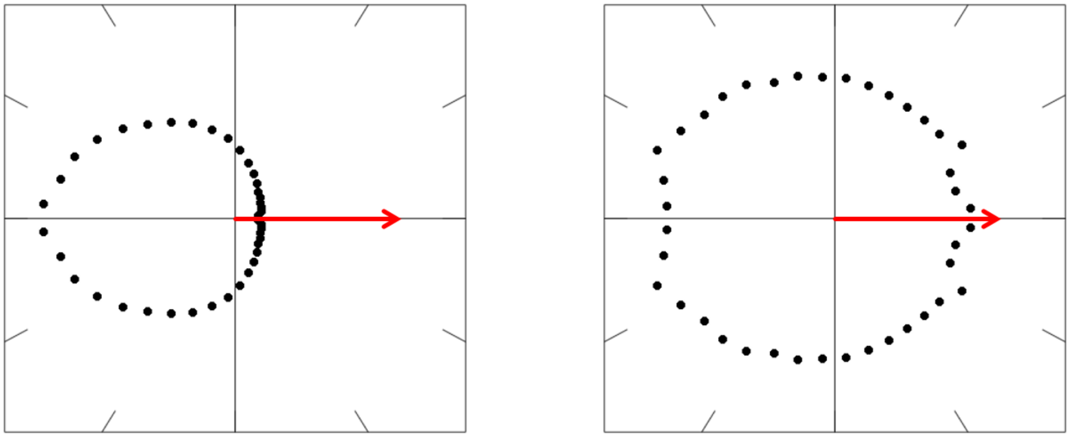

Figure 2.38: The angle between photoelectrons for symmetric (left) and asymmetric (right) energy sharing. The red arrow indicates the direction of the high-energy electron in the asymmetric case.

However, in the two-body breakup, a large quantity of the electrons asymmetrically share energy, which is not well explained by the "knock out" model. A second model, the so-called shakeoff, is one where the rapid vacation of the primary photoelectron causes a change in the inter-molecular binding forces such that a secondary electron relaxes into a continuum state [13]. The shakeoff model predicts asymmetric energy sharing between the electrons, where the primary photoelectron carries away virtually all of the photon energy and the secondary electron relaxes into a continuum state marginally above its zero point energy.

Figure 2.38 displays the expected angular distributions for the "knockout" and "shakeoff" models of double photoionization. The "shakeoff" low energy electron exits the dication isotropically, with virtually no kinetic energy and no reason to do otherwise. The "knockout" photoelectron is given momentum by the primary

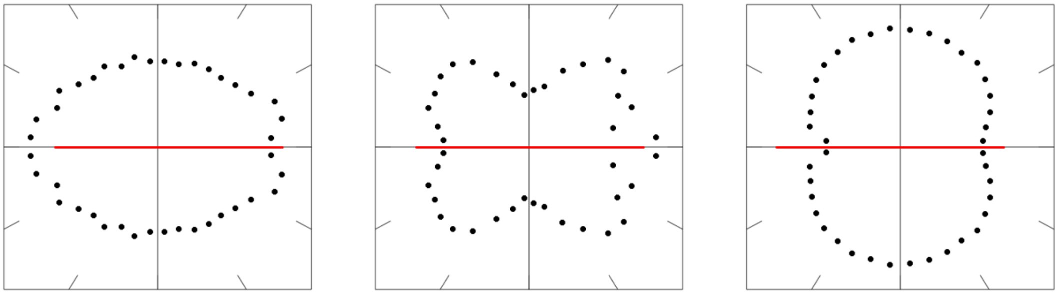

Figure 2.39: The low energy electron isotropy is perturbed into a p-wave-like distribution (left). The high-energy electrons follow a d-wave-like distribution (center). The symmetric energy sharing electrons appears to be mixed p- and d-wave-like distributions (right). The right bar shows the polarization axis.

photoelectron and shares energy, and their proximity manifests in mutual Coulomb repulsion.

Further scrutiny of the system reveals an abundance of electronic structure. Figure 2.39 shows the angular correlation of the photoelectrons with the polarization axis for both the asymmetric sharing cases, as well as the symmetric sharing case. Each regime has a unique angular distribution signature.

A final figure in the analysis of the photoelectron distributions for the two-body breakup is one where the polarization axis is perpendicular to the high energy electron. The angular distribution of the low energy "shakeoff" electron is plotted in this regime in figure 2.40. The theoretical techniques necessary to generate such an angular distribution are currently under development in the theory group at Berkeley.

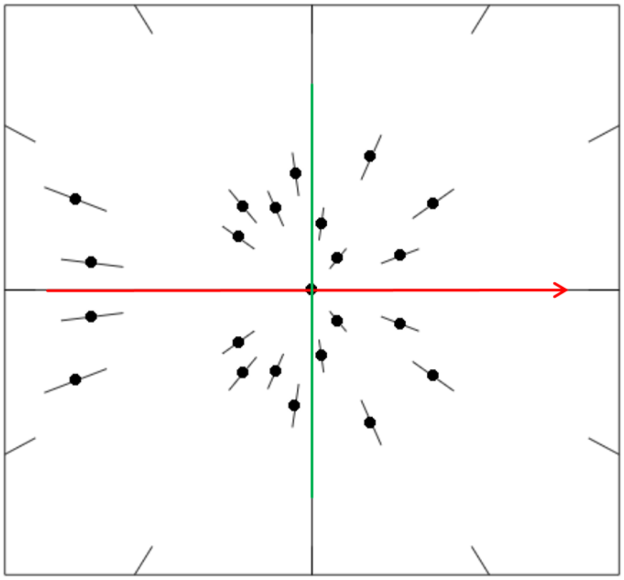

Figure 2.40: The angular distribution for the low energy electrons when the high energy electron is perpendicular to the polarization axis.

2.6 Analysis Summary

Analysis of the ionic fragments following double photoionization of water generated a map between the available dication states and the asymptotic two- and three-body breakups. The power of the COLTRIMS technique allows this molecular breakup to be fully imaged in three dimensions - the molecule was oriented in its own reference frame, and the relative motion of the dissociating dication and photoelectrons have been measured in that reference frame. This is, as of the writing of this thesis, a first in molecular photodissociation research. There is no existing theoretical model for the treatment of electron correlation between two valence photoelectrons in such a system. This thesis, or at least its presented data, serve as motivation to advance electron correlation techniques in the field.

Chapter 3

CF_4 Experiment: Apparatus and Background

3.1 Introduction

The CF_4 experiment is due to a pair of publications by Frímann H. Ómarsson and associates. Their experiment of dissociative electron attachment (DEA) to carbon tetrafluoride yielded exciting - and somewhat exotic - results. Perhaps the most fundamental tenet of modern science is the requirement of reproducibility: an experiments results, whether they are expected or wholly new, must be reproducible. The goal of the Auburn experiment was twofold: to see if the unique outcome of the Ómarsson group could be reproduced, and also to bring to bear the COLTRIMS molecular microscope on the carbon tetrafluoride system. The history of dissociative electron attachment to CF_4, a basic discussion of the physical process, and an in depth review of Ómarsson's results constitute this chapter.

3.2 Dissociative Electron Attachment

Electron scattering experiments are substantially different than photodissociation experiments, particularly at low energies. When the molecular potential extends in to the continuum, incident electrons can become trapped in this potential, coupling to the electronic configuration of the molecule. In the case of carbon tetrafluoride, the resonance state is metastable and the ion falls apart in one of two ways:

$$e^- + CF_4 \begin{array}{l} \longrightarrow CF_3 \; + \; F^- \\ \longrightarrow CF_3^- \; + \; F \end{array}$$

3.2.1 Resonance

Resonance is, in a simple picture, the coupling between two physical systems, e.g., vibration of one system drives or enhances vibrations in another. In dissociative electron attachment, electrons couple to molecular system via a resonance of some kind. The resonance description of this process implies that it only occurs over particular energy ranges for the incident electron. That electron's wave function couples to some part of the molecular system, and that interaction drives the dissociative process. Two particular types of electron scattering resonances are known to be relevant in this case: shape resonance and Feshbach resonance.

The outer valence electron term for the ground state CF_4 molecule is:

$$...(4a_a)^2(3t_2)^6(1e)^4(4t_2)^6(1t_1)^6 \tag{3.1}$$

This configuration has two low lying antibonding σ^* orbitals of character a_1 and t_2. A low energy electron can couple into the unoccupied antibonding orbital in one of two ways. In the first, the electron is merely trapped in the centrifugal barrier of the potential well. It couples to the "shape" of the electrostatic potential near the molecule - a shape resonance. In the second case, the incident electron scatters off one of the bonding electrons in the molecule. Both electrons can then be trapped in the empty antibonding orbitals. In such a case, where the external electron couples to an internal degree of freedom of the molecule (the bonding electron), the resonance is referred to as a Feshbach resonance, named for Herman Feshbach.

3.3 History of DEA to CF_4

Of particular interest in the DEA process is the eventual partitioning of the incident electron's kinetic energy. DEA is an electron-molecule scattering collision, and so the electron's kinetic energy must couple into the molecular system in some way. An early paper into the partitioning of the electron energy in DEA came from P.W. Harland and J.L. Franklin [14]. Harland and Franklin measured the kinetic energies of several ion species following DEA, including NF_3, BF_3, and the subject of this thesis, CF_4. The incident electron's translational energy is distributed across translational, vibrational, and electronic degrees of freedom in the intermediate metastable molecular ion. This distribution of energy can vary within a particular species based on ion formed after dissociation, e.g., the kinetic energy of the fragments depends on which fragment traps the extra electronic charge. The attachment process to CF_4 comes in two varieties, wherein either F^- or CF_3^- fragments are created after dissociation. Within the F^- channel, there are two potential outcomes. In the first case, two different resonances can be measured. In the first, the F^- fragment has nearly zero translational energy. This is likely due to a resonance where virtually all of the electron energy is deposited into vibronic degrees of freedom in the CF_3 fragment, or in a reaction pathway that produces three fragments:

$$e^- + CF_4 \rightarrow F^- + F + CF_2 \tag{3.2}$$

Harland and Franklin discuss the possibility of reaction 3.2 in two forms:

$$e^- + CF_4 \rightarrow F + CF_3^- \tag{3.3}$$

$$CF_3^- + F \rightarrow CF_2 + F + F^- \tag{3.4}$$

$$e^- + CF_4 \rightarrow F_2^- + CF_2 \tag{3.5}$$

$$F_2^- + CF_2 \rightarrow CF_2 + F + F^- \tag{3.6}$$

In both 3.3 and 3.5, Harland and Franklin calculated that the second step was endothermic and, therefor, energetically forbidden under the circumstances of the experiment. They concluded, therefore, that the quasithermal F^- channel was due to:

$$e^- + CF_4 \rightarrow F^- + CF_3^* \tag{3.7}$$

Data from Harland and Franklin for the appearance energies, resonance maxima, and $\frac{KER}{E_{electron}}$ are given in table 3.1.

Following Harland and Franklin in 1978 was a more focused paper by Verhaart *et al* [15]. Verhaart investigated the electron transmission spectra, dissociative attachment and threshold excitation spectra for CF_nCl_{4-n}, for $n = [1, 4]$. Verhaart *et*

Table 3.1: Data from Harland and Franklin

Ion	**Appearance Energy (eV)**	**Resonance Peak (eV)**	α **(slope)**
F^-	4.65 ± 0.1	6.15 ± 0.1	0.40
$(thermal)$	$6.2 - 6.5$	7.5	0.46
CF_3^-	5.4 ± 0.1	6.9 ± 0.1	0.33

al were motivated in part by the interaction that chlorofluoromethane decomposition fragments have with the ozone layer. Low energy electron impact studies of these species were important to advancing understanding of electronic states that were inaccessible to photon spectroscopy.

Verhaart's paper found no evidence for the thermal F^- channel implied by [14]. The F^- peak height was found near 7 eV, situated between the peak heights found by [14]. For the CF_3^- channel, a peak height of 6.9 eV was found, in agreement with Harland. Verhaart attributes the dissociative process to the incident electron being caught in a vacant antibonding $C - F$ molecular orbital.

In 1980, E. Illenberger [16] repeated some of the measurements of Verhaart, with particular emphasis on the translational energy distributions of the reaction fragments. Illenberger observed the quasi-thermal ion channel previously measured by Harland. The value of the Illenberger paper is their presentation of their data points providing the relationship $\frac{KER}{E_{electron}}$, given as parameter α by Harland. These data points will be used later in considering the results from the Auburn experiment.

A paper dedicated entirely to the investigation CF_4 DEA resonances was produced in 1994 by Le Coat *et al* [17]. Le Coat summarizes the potential resonances based on the point group of CF_4, the T_d group. Le Coat's paper gives another set of data to contrast with the KER slope, as well as making low resolution observations on the angular distribution of the ions. They conclude that the $^2T_2$ shape resonance is responsible for the dual channel which produces F^- and CF_3^- fragments, while attributing the thermal F^- channel to a $^2T_1$ Feshbach resonance. In contrast with Harland and Franklin, Le Coat concludes this thermal channel is the result of double bond breaking. Finally, Le Coat observes that there is no evidence for contributions from the $^2A_1$ shape resonance, and no evidence of the Jahn-Teller effect.

Table 3.2: CF_3^- Data from Le Coat

Electron Energy (eV)	CF_3^- **Fragment (eV)**	**Total KER (eV)**
5.5	0.218	0.90
6.0	0.265	1.23
6.8	0.338	1.57
7.0	0.411	1.90
7.5	0.476	2.21
8.0	0.540	2.50
8.5	0.613	2.84
9.0	0.649	3.01

The final points of reference in the literature are the papers by Ómarsson *et al* ([18],[19]), which served as motivation for the experiment performed in Auburn's DEA laboratory. These papers refer to the same experiment, which employed a velocity slice imaging (VSI) experimental technique. VSI stands in contrast to the other experiments referenced in this history due to its ability to measure the full 360^o angular distribution of the dissociation. Due to the cylindrical symmetry of the system, the true angular distribution is in fact spanned in 180^o. However, earlier measurements of the angular distribution[17] did not measure the full range of angles.

The experiment by Ómarsson yields a discontinuous change in the slope of the KER release, around 7 eV incident electron energy. This stands in sharp contrast to results in the literature, where the slope is a constant value throughout the range of the resonance. Ómarsson attributes this abrupt change to energetic restrictions of the DEA resonance below the bond dissociation energy (BDE) of the $C-F$ bonds. The argument goes that, below the BDE, the CF_3^- anion must rearrange itself to its lowest energy equilibrium geometry. This takes considerable energy, and is primarily responsible for the vibrational distribution of incident electron energy. In contrast, above the BDE the process is assumed to proceed directly, in a non-adiabatic fashion wherein the majority of the incident electronic energy is converted into KER.

The presence of this "kink" in the KER for the CF_3^- channel, as an entirely unique result, was motivation for the experiment performed at Auburn. Details of Ómarsson's experiment, such as KER and angular distribution, will be referenced later during the analysis section.

3.4 Experimental Apparatus

3.4.1 Review - COLTRIMS experiments

The experimental apparatus used for the CF_4 experiment employs some of the same techniques that the water experiment used. In particular, it is a COLTRIMS experiment, exploiting a cold molecular gas beam and a position sensitive delay line anode detector. The specific details of this apparatus differ significantly from the water experiment, however.

The Auburn DEA COLTRIMS experiment consists of several interacting systems. These systems will each receive a direct treatment in the following sections:

- Vacuum System
- Residual Gas Analyzer
- Ion Gauge Array
- Gas Jet
- Electron Gun
- Spectrometer

3.4.2 Vacuum System

All of the equipment used in the experiment requires high vacuum to operate. The chamber consists of four regions, each with a dedicated turbo pump. These turbo pumps are networked into three roughing pumps, which are used to pre-pump the vacuum and to maintain low vacuum downstream of the turbo pumps.

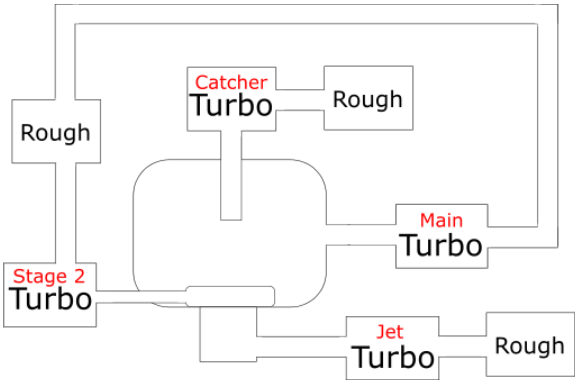

Figure 3.1: Each primary vacuum region is pumped by a turbo pump, backed by a roughing pump. The chamber and second stage, which see minimal throughput, share a roughing pump.

3.4.3 Residual Gas Analyzer

The Residual Gas Analyzer (RGA) is a diagnostic tool used to scrutinize the background content of the vacuum. A RGA is a small, sturdy mass spectrometer. It is attached to the main chamber and measures both the content and relative partial pressures of gas species making up the background atmosphere of the experiment.

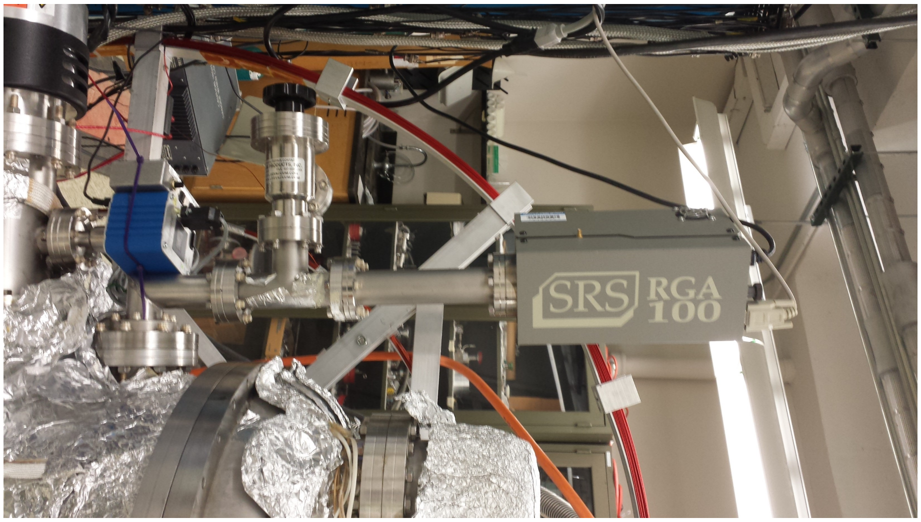

Figure 3.2: The RGA is attached to the main chamber region via an external flange.

The RGA serves several functions. In times of questionable vacuum integrity, it can be used to hunt leaks in the apparatus via its ability to detect tiny amounts of a tracer gas (typically helium). The RGA can also be used to detect severe jet misalignment or a clogged gas jet nozzle - the gas jet species is measured in the RGA if it makes it into the main vacuum chamber. Often, a technique called ”baking” is used to drive the most common contaminant, water, out of the vacuum chamber. Baking involves slowly raising the temperature of the chamber walls to expel adsorbed water molecules, which are gradually pumped out of the chamber.

The RGA measures the partial pressure of water in the chamber and acts as a guide for the effectiveness of the chamber bake. Finally, the RGA can be used to scrutinize the content of a gas jet. The gas jet can become contaminated via leaks or improper gas jet line pumping. Due to the geometry of the experiment, these contaminants and leaks are imperceptible otherwise. The partial pressure rises measured in the RGA can verify the presence of contaminants such as N_2 in the gas jet.

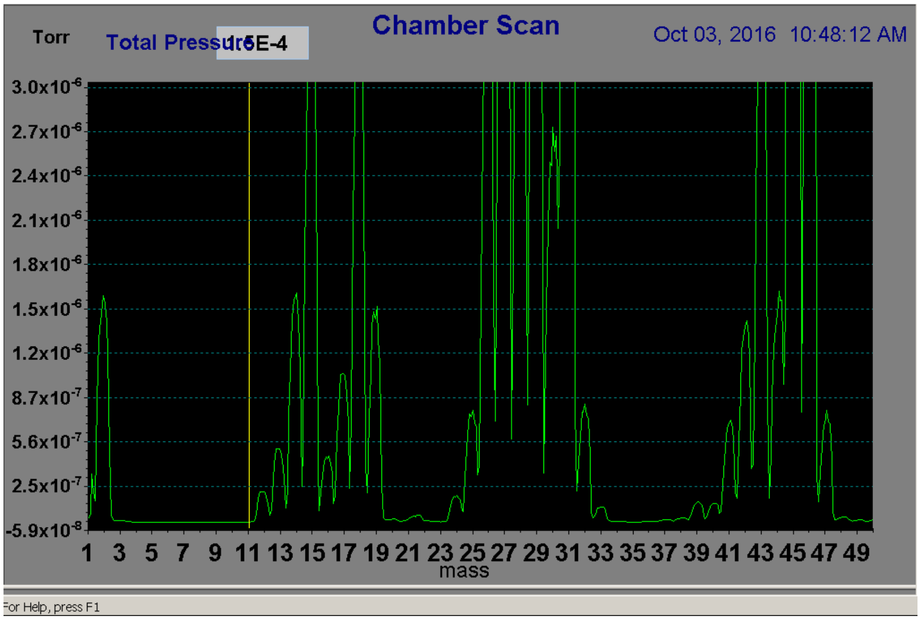

Figure 3.3: One of the many functionalities of the RGA: a mass spectrum of the residual gas given in partial pressures. The image shown is the result of ethanol being sucked into the chamber through a leak.

3.4.4 Ion Gauge Array

Each section of the experiment that is under vacuum (Jet, Second Stage, Chamber, Catcher) has an ion gauge attached. Tracking the individual pressures in each region gives valuable diagnostic information about the state of the experiment, in particular the status of the gas jet. A table of diagnostic examples is shown in table 3.3.

Table 3.3: Ion Gauge Diagnostics

Gauge Location	**Pressure (torr)**	**Diagnosis**
Jet	$> 3 \times 10^{-4}$	Risk of overheated jet turbo
Catcher	ΔP small	Jet is not aligned
Main	ΔP large	Jet is not aligned
Jet/Catcher	ΔP large/small	Partial nozzle blockage
Jet	$< 10^{-4}$	Complete nozzle blockage

3.4.5 Gas Jet Alignment

The jet nozzle is mounted on three externally controlled movement tracks to allow translational motion in three dimensions. The x and y directions control the nozzle alignment with the skimmer, while the z direction allows movement of the nozzle toward or away from the skimmer. Typically, the z distance is determined by the size of the nozzle, and is not actively adjusted.

Alignment of the gas jet involves the tracking of two different diagnostic values: the RGA partial pressure of the test gas, and the catcher pressure. If the jet is aligned, the rise in catcher pressure should be maximized. If it is not aligned, extraneous gas will leak into the chamber region and will find it's way into the RGA. Therefore, ideally, simultaneous maximization of catcher pressure and minimization of RGA partial pressure guarantee the best possible positioning for the jet nozzle relative to the skimmer.

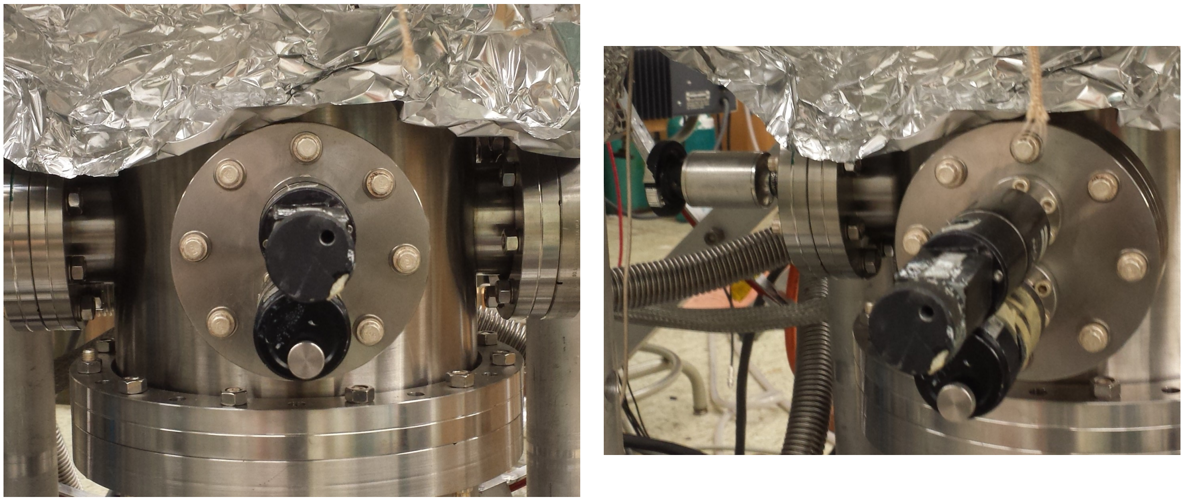

Figure 3.4: External adjustment of the jet nozzle is controlled through translation in 3 directions with external knobs.

3.4.6 Electron Gun

The electrons used for the scattering interaction of interest are produced by an ELG-2 Electron gun manufactured by Kimball Physics. The device comes with a EGPS-1022 digital power supply and control unit. The electron gun is aligned perpendicular to both the length of the spectrometer and the molecular beam. The electron emitter is a refractory metal thermionic emitter directly heated by a voltage source. The voltage source is referenced off the electron energy voltage, which is in turn referenced to system ground. Adjacent to the electron emitter is a grid, which allows the user dynamic control of the quantity of electrons released or, in the case of this experiment, a mechanism to pulse electron emission. The electrons are drawn into the main body of the gun by a local positive voltage, the so-called first anode. The beam is electrostatically collimated by a focusing voltage, and passes through X and Y deflection elements before exiting the gun.

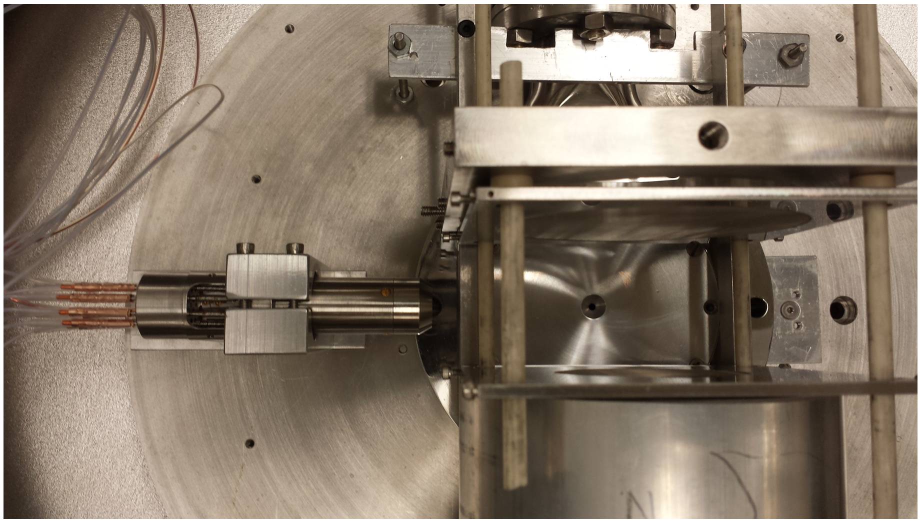

Figure 3.5: A picture of the electron gun at it's experimental resting position of 1cm outside the interaction region plates.

The Auburn experiment uses the magnetic fields of a Helmholtz coil configuration to steer the electrons and as a result does not employ the deflection elements of the electron gun. A schematic of the electron gun is shown in figure 3.6. A picture of the gun in the chamber is shown in 3.5.

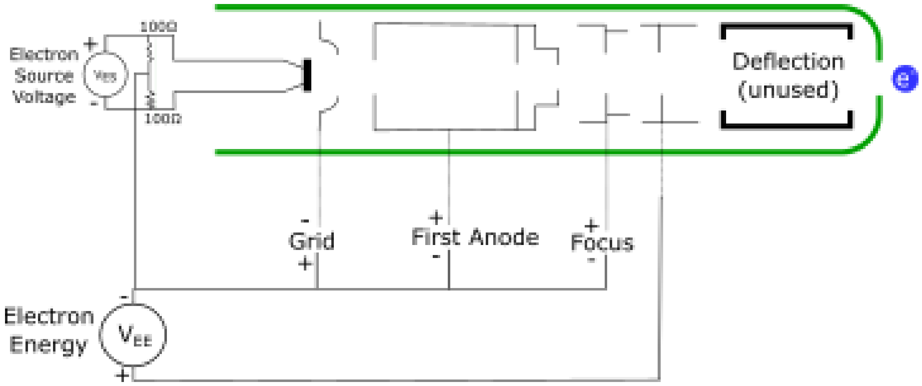

Figure 3.6: A simplified schematic of the electron gun.

3.4.7 Spectrometer

The spectrometer used in the CF_4 experiment is fundamentally different than the one used in the water experiment. The incident reaction particle is an electron, which responds to electric and magnetic fields. Furthermore, DEA experiments produce only one negative ion as a reaction fragment; neither electrons nor positive ions are created. The resulting spectrometer configuration must be chosen with each of these details under consideration.

Geometry The spectrometer geometry is shown in figure 3.7.

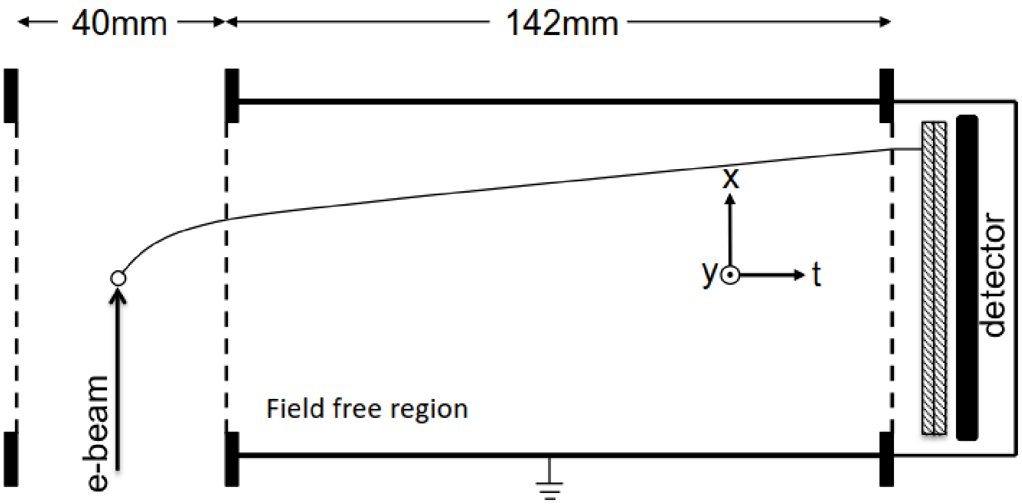

Figure 3.7: Schematic of the spectrometer used for DEA data measurement.

The spectrometer consists of a 40mm electric field region and a 142mm field-free region. The lab frame is defined by the electron beam (x-axis), molecular jet (y-axis), with the z-axis coaxial with the spectrometer. Since there is only one direction for dissociation fragments to travel, the "z" direction is called "t", referring to the "time-of-flight" direction. There is no significant reason for this notation change, except that it is sometimes helpful in mental visualization of the data. A picture of the spectrometer resting in the chamber is shown in figure 3.8.

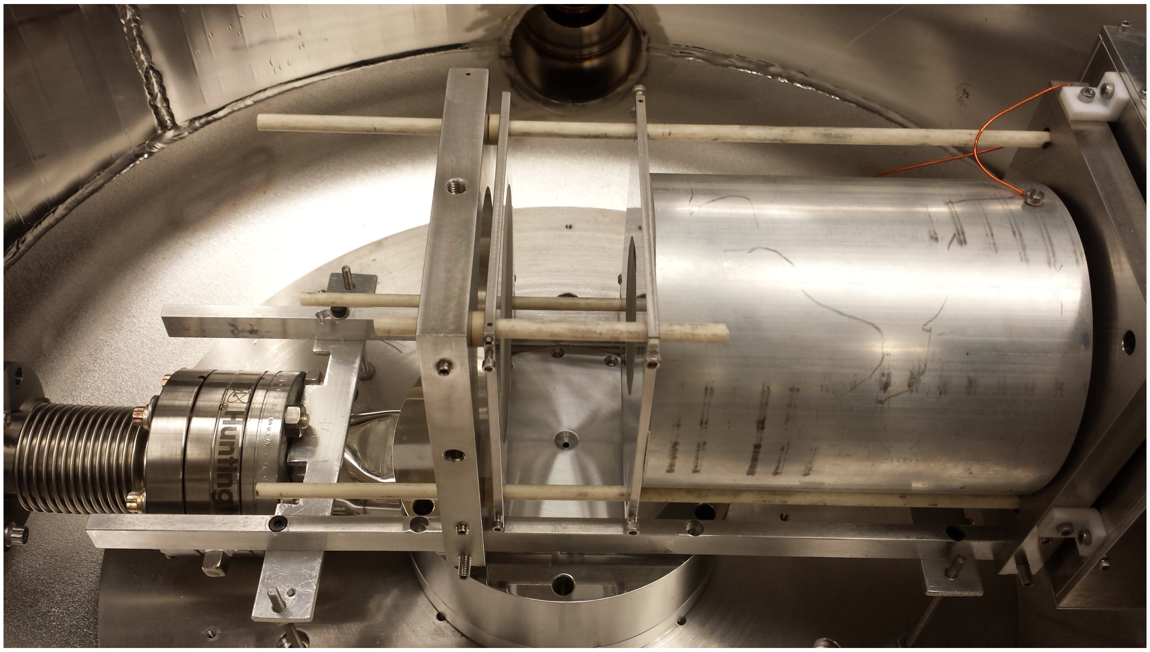

Figure 3.8: The second stage turbo pump is connected via the bellows in the image (left). The knife edge second stage skimmer can be seen below the interaction region (center). The drift region is a metal tube held at electric ground (right.)

The 40mm electric field region is defined by two circular wire mesh grids. The grid attached to the field free region is held at common ground. The mesh grids are parallel, forming a capacitor-like geometry. The field free region is used to give the Newton sphere created by the DEA reaction time to expand. Maximizing the area of the Newton sphere on the detector improves angular resolution.

Electric and Magnetic Fields The incident reaction particle, an electron, is susceptible to interaction with the spectrometer's electric field. To avoid disrupting the path of the electron beam, the entire experiment is undertaken under a pulsing scheme. In each cycle, the electron gun is pulsed for 50ns. As the electron beam crosses the molecular jet, DEA reactions occur. A fixed delay of $1\mu s$ follows the electron gun pulse, during which time the Newton sphere of the reaction fragments is allowed to expand. At the end of the delay, the left grid is raised to +250V for $1.3\mu s$. The pulse width and height are chosen carefully following Simion simulations to ensure the particles are still inside the electric field region when the pulse ends. This fact will be used later when considering the energy imparted to the particles by the spectrometer field.

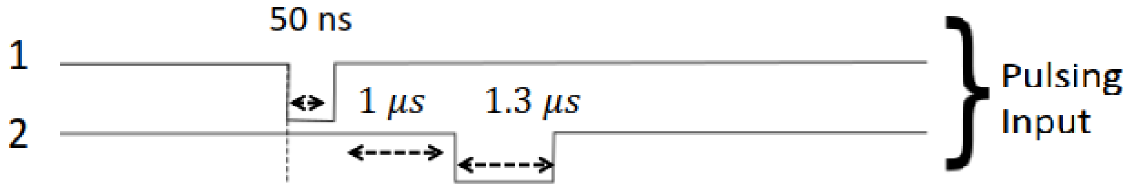

Figure 3.9: Schematic of electron bunch and electric field pulsing.

An external Helmholtz coil configuration and two square wire pairs surround the experimental chamber. This array is used to create a magnetic field which steers the electrons across the interaction region. Due to the substantially larger mass of the DEA fragments, their path is largely unaffected by the external magnetic field.

3.4.8 Signal and Data Processing

Data signals leave the chamber in the form of five pulses: one for the MCP, and two each for the x and y direction wire pairs in the DLA. This signals are small and require, as a first treatment, fast amplification. The chamber feedthrough, manufactured by Roentdek, brings the four DLA pulses out in pairs that are fed through shielded ethernet cable into a fast amplifying unit built, also built by RoentDek. The DLA pulses are then fed individually into a constant fraction descriminator, the operation of which is described in Chapter 1. The MCP pulse, in contrast, is delivered to a dual fast-amp and CFD unit made by Roentdek.

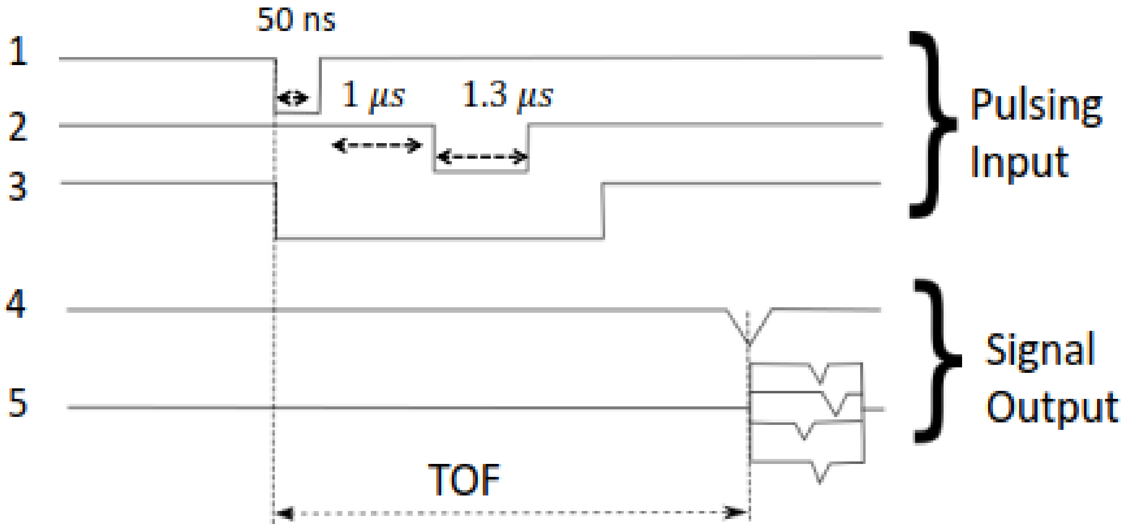

Figure 3.10: The full pulsing scheme of the spectrometer: 1) Electron Bunch 2) E-field delay and pulse 3) Electronic Veto 4) MCP Pulse 5) Anode Pulses

The full pulsing scheme is illustrated in figure 3.10. A full map of the electronics used in signal processing is illustrated in figure 3.11.

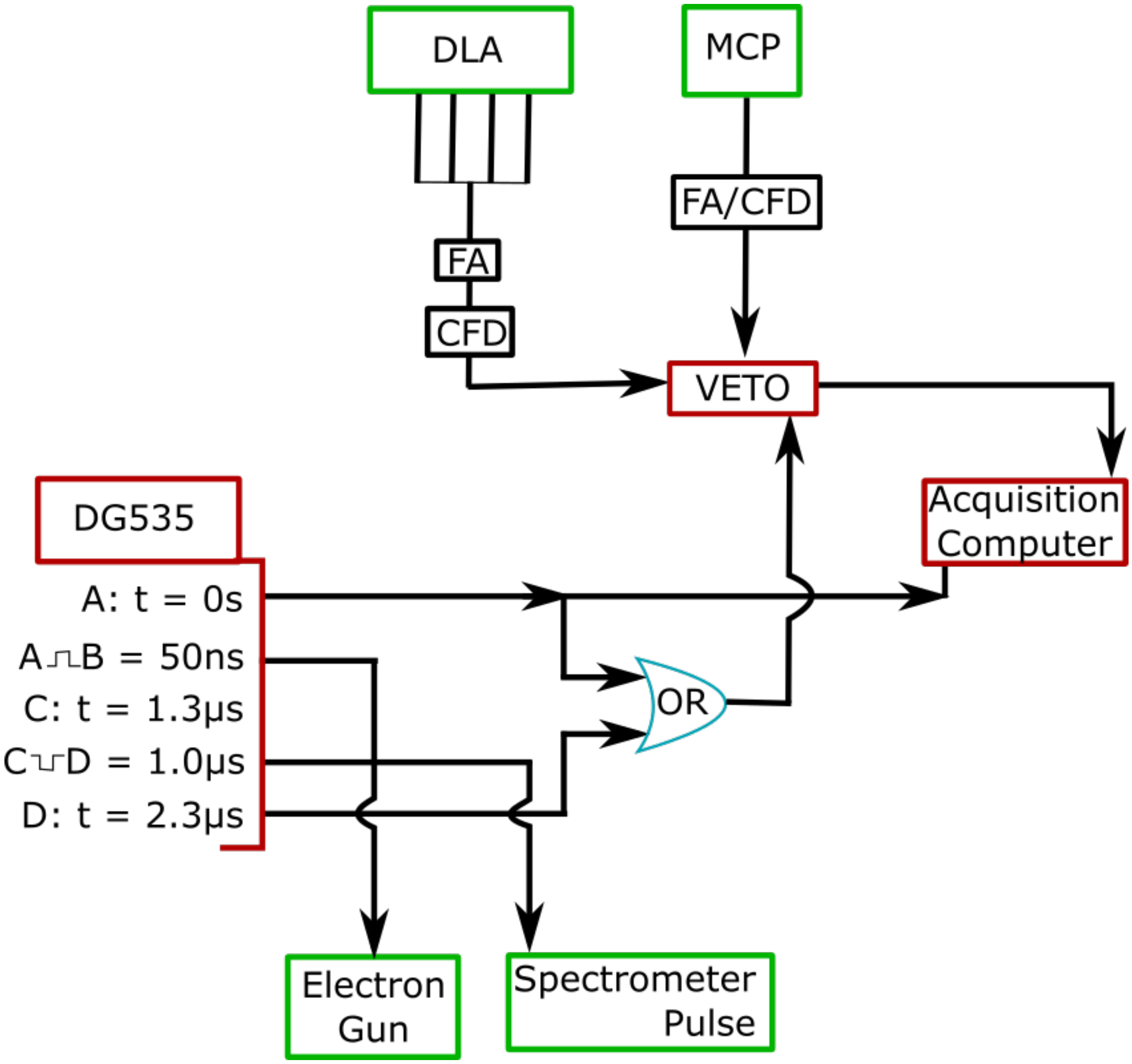

Figure 3.11: The experiment timing is controlled by a DG535 pulser unit, which controls when each device triggers.

Chapter 4

CF4 Experiment - Analysis and Results

4.1 Introduction

In general, the CF_4 analysis was a less involved process than that of the water experiment. A four particle system necessarily involves particle correlation and coincidence measurement - a single particle system has neither. Nevertheless, careful simulation, calibration, and gating are crucial to accurate analysis, and are discussed in their own sections before the experiment's results are presented.

4.1.1 Simulations

Two simulation tools are used to anticipate the appropriate spectrometer settings and to find time of flight corrections that must be applied to the raw data. Both simulations are used together to approximate the ion times of flight and to maximize the effective detector area used for data acquisition.

Excel Simulation The Microsoft Excel simulation used in the CF_4 experiment is similar to the one used in the water experiment, with the obvious exception of describing a different experimental geometry. It is a coarse tool that is used to compliment SIMIONs superior simulation and visualization environment.

Simion SIMION is a simulation software suite that is used to calculate electric fields and charged particle trajectories. The platform allows construction of surfaces whose electric potentials can be fixed or scripted to change in a prescribed way. It also allows the user to create charge particle distributions to observe the dynamics of these charged particles in the aforementioned electric fields.

For the CF_4 experiment, a SIMION environment designed by a previous Auburn graduate student (and possessing the same geometry as the current experiment) was used to simulate the z-direction time of flight for the CF_3 ions. A Lua script is used to control the simulated spectrometer settings and their time dependent behavior, and to generate fit data in Microsoft Excel.

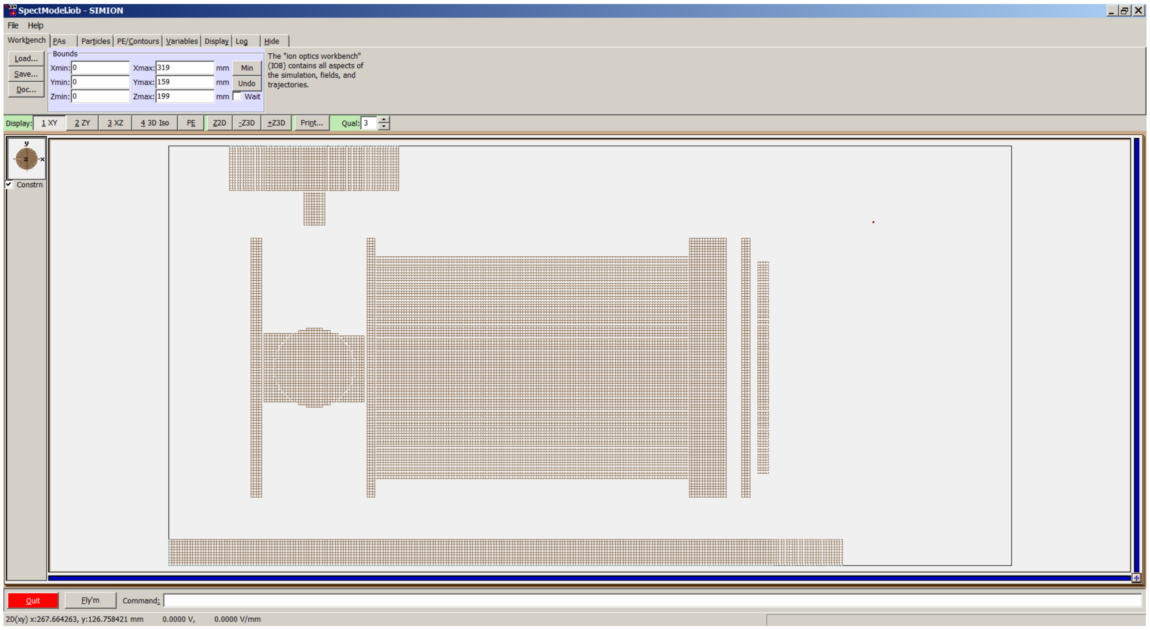

Xmin: 0 Xmax: 319 mm
Ymin: 0 Ymax: 159 mm
Zmin: 0 Zmax: 199 mm
☐ Wait

The "ion optics workbench" (IOB) contains all aspects of the simulation, fields, and trajectories.

Qual: 3

☑ Constrn

2D(xy) x:267.664263, y:126.758421 mm 0.0000 V, 0.0000 V/mm

Figure 4.1: The geometry of the spectrometer for the DEA experiment is simulated by defining equipotential surfaces in the SIMION world.

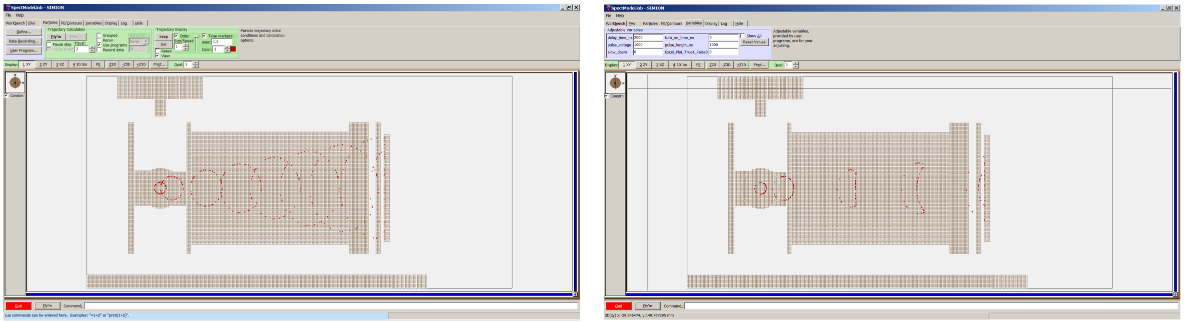

Figure 4.2: Simion will track the trajectory of particles as either lines or dots, and will leave markers for fixed time intervals as defined by the users. A good sim (left) and a bad sim (right) are shown for contrast.

A screen shot of the SIMION spectrometer used to simulate the experiment environment is shown in 4.1. SIMION works by numerically solving Laplace's equation for the electric potential function. The world is broken up into a mesh of 1mm cubes and the potential is found at each grid point. The user can then define particles with varying charges, masses, and initial conditions such as velocity and direction. SIMION finds the equation of motion for each grid point, updates the position of the particle, then recalculates the equation of motion based on the potential mesh solution to Laplace's equation.

In a bad experimental setting, the Newton sphere will be inverted along the leading edge. A non-spherical Newton sphere incident on the detector will not measure correct TOFs for the inverted segment, which will make the data unusable.

4.2 Analysis

The analysis portion of DEA COLTRIMS experiments generally consists of two phases: calibration and data visualization. Calibration involves adjusting SIMION script parameters until the simulation and TOF data match, and using the corresponding spectrometer settings to calculate the negative ion t component momenta. The x and y momenta components are then centered and scaled to match the simulation. Once the momenta are corrected, analysis of the KERs and angular distributions is possible.

4.2.1 Calibration

Calibration of the CF_3^- data involved matching the SIMION simulated spectrometer settings to the measured time of flight data for the experiment. The difference in TOF for F^- and CF_3^- particles should depend on the spectrometer settings. The electric field pulse used to push the reaction fragments toward the detector turns off before the particles leave the interaction region. The impulse on the particles is:

$$\overrightarrow{J} = \int_0^T \overrightarrow{F} \cdot dt = \int_0^T q\overrightarrow{E} \cdot dt \tag{4.1}$$

The interaction region has a roughly parallel-plate capacitor geometry; the electric field $\overrightarrow{E}$ is therefor a constant that does not depend on time. The integral in equation 4.1 reduces to

$$\overrightarrow{J} = q\overrightarrow{E}\Delta t_{pulse} \tag{4.2}$$

Δt corresponds to the pulse "width" of the electric field. J, the impulse, is the change in momentum of the particle in the field, $\Delta p = p_f - p_i$. Due to the careful configuration of the COLTRIMS apparatus, the particles have an initial momentum in the z direction of 0. The final z-direction momentum, p_z, is then:

$$p_z = qE\Delta t_{pulse} = mv_z \tag{4.3}$$

Once the pulse has turned off, the particles drift in a field free region until colliding with the MCP, at which time the event is considered "recorded". The time between the end of the spectrometer pulse and recording of the event must correspond to the time of flight of the particle. With the velocity of the particle, this time of flight can be found as:

$$TOF = \frac{x_{drift}}{v_z} = \frac{mx_{drift}}{qE\Delta t_{pulse}} = \frac{x_{drift}}{E\Delta t_{pulse}}\frac{m}{q} \tag{4.4}$$

The TOF is proportional, then, to $\frac{m}{q}$. For particles of fixed charge $-q$, the TOF is linear with mass.

With knowledge of the TOF's functional dependence on mass, the process of calibrating the SIMION simulation can begin. The experimental data consists of two TOF peaks: one for each particle, F^- and CF_3^-. In a system where $t_0 = 0$, the TOF for a particle of mass 0 should also be 0. However, the pulsing scheme employs a delay after the electron bunch pulse before the electric field pulse is switched on. This delay should correspond to a shift in the TOF spectrum for all particles of exactly that pulse delay (figure 4.3).

Clearly the TOF-intercept on such a graph moves down with any delay in the electric field pulse. Furthermore, due to the lengths of cables and myriad other

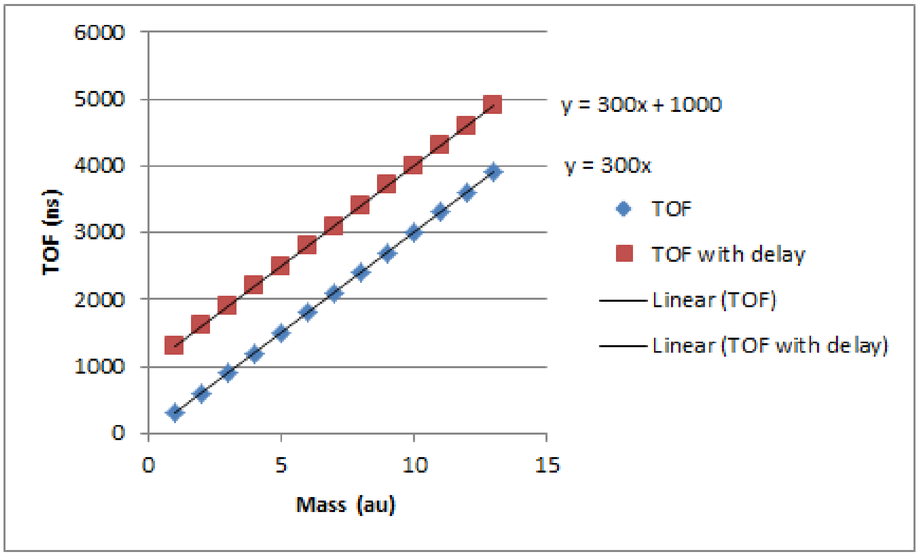

Figure 4.3: The delay of the spectrometer pulse moves the y-intercept for the linear TOF vs mass plot.

experimental factors, the delay of the real experiment is longer than the intentionally selected pulse delay. Regardless of this delay, the *slope* of the line should depend only on the spectrometer settings - the delay only shifts the y-intercept. This fact determines the fitting procedure for the SIMION simulation.

The slope of the TOF vs mass curve is first calculated from the experimental data. The spectrometer parameters of SIMION are then adjusted slightly until the simulated TOF vs mass slope matches the experimental one. The SIMION simulation is run using the correct settings and generates a p_z fit equation that takes, as an input, the TOF of the particle. The fit uses only the spectrometer delay prescribed in the experimental setup. The final step is to adjust the experimental TOF to match the corrected SIMION TOF intercept to accomodate for the unknown delays in signal processing. The p_z momentum is generated from the adjusted TOF data.

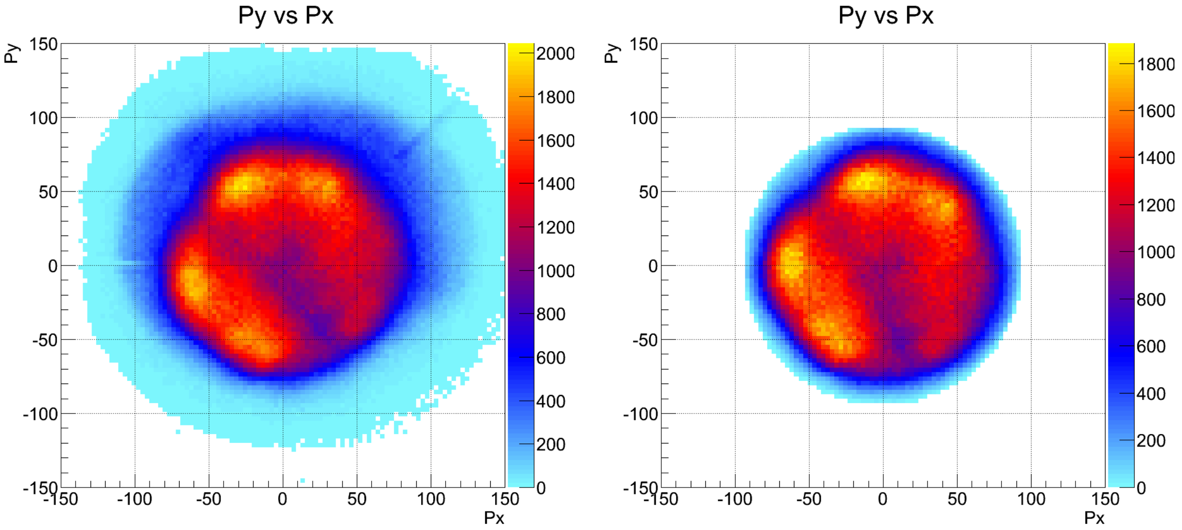

Figure 4.4: Centering the fragment momenta is necessary for correct KER calculation. A density plot of Py vs Px for the CF_3^- fragment at 8 eV incident electron energy is shown before (left) and after (right) momentum adjustment and gating.

The LMF2ROOT software calculates $p_{x,y}$ values using the adjusted TOF values:

$$p_{x,y} = \frac{m\Delta(x,y)}{TOF} \tag{4.5}$$

The scale of these values is approximately correct, as the TOF has already been adjusted in SIMION calibration step. However, the momenta are unlikely to be centered properly in the lab frame. The gas and electron jets do not cross at precisely the center of the spectrometer. As a result, the momenta are offset in each dimension. Each of the x, y, z momenta should be centered in momentum space; small adjustments to these values are made to center the distributions (figure 4.4).

Once the momenta are centered, the final step in calibration is to adjust the magnitudes of the momenta components. Since the molecule is randomly oriented at the time of the collision, the Newton sphere following dissociation should be isotropic. The momenta component distributions should therefor be similar in magnitude, and their 2D density plots should be round. Adjustments to stretch or compress these components can be done in LMF2ROOT. Once this step is complete, differential analysis of the KER and angular distributions is possible.

4.3 Results

The CF_4 experiment encountered significant experimental difficulty that made a complete measurement of the system impossible. In section **4.1.1: Simulations**, it was shown that non-ideal spectrometer settings can lead to an inversion of the leading edge of the Newton sphere, visualized in figure 4.2. A broad peak of noise plagued measurements of the experiment. The noise is displayed in 4.5.

The presence of the noise was attributed to various things at various times throughout attempts to fix it. As of the writing of this thesis, it is being attributed to erroneous electron gun spray that is back-scattering from different metal surfaces inside the experiment. Future chamber designs will likely include some kind of electron gun beam collimation.

The papers by Ómarsson [18, 19] identified unique results for the CF_3^- particle. A determination was made that the CF_3^- channel was of more interest to the Auburn group. Through a non-ideal spectrometer pulsing arrangement, the CF_3^- signal was delayed beyond the TOF of the unsolved signal noise. The F^- Newton sphere experienced lead-edge inversion as a result, and so anything beyond it's characteristic TOF could not be resolved with these data.

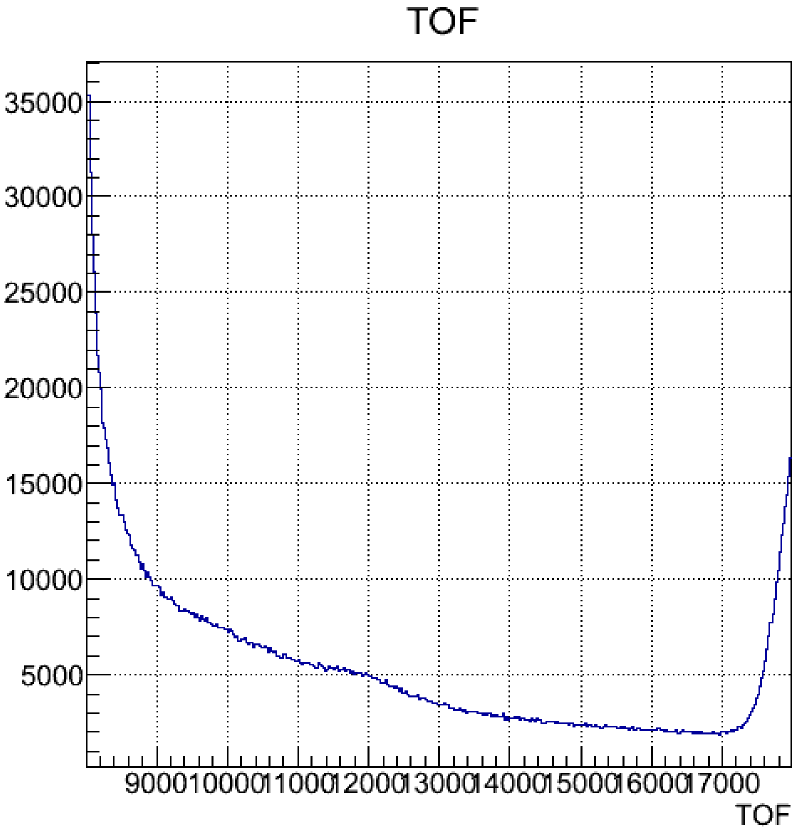

Figure 4.5: The F^- and CF_3^- peaks are cut off on the left and right side respectively. The long gradually sloping shoulder is most visible at 12000ns.

4.3.1 Momenta Distributions

Due to the random orientation of the molecule at the time of the electron scattering, the data should reflect a cylindrical symmetry about the axis of the incident electron beam. Figure 4.6 illustrate the cylindrical nature of the distribution.

The figures shown in 4.6 are projections of a Newton sphere onto two dimensions. While this can occasionally be sufficient, it is more informative to view thin slices of the Newton sphere that capture the angular character of the distribution without

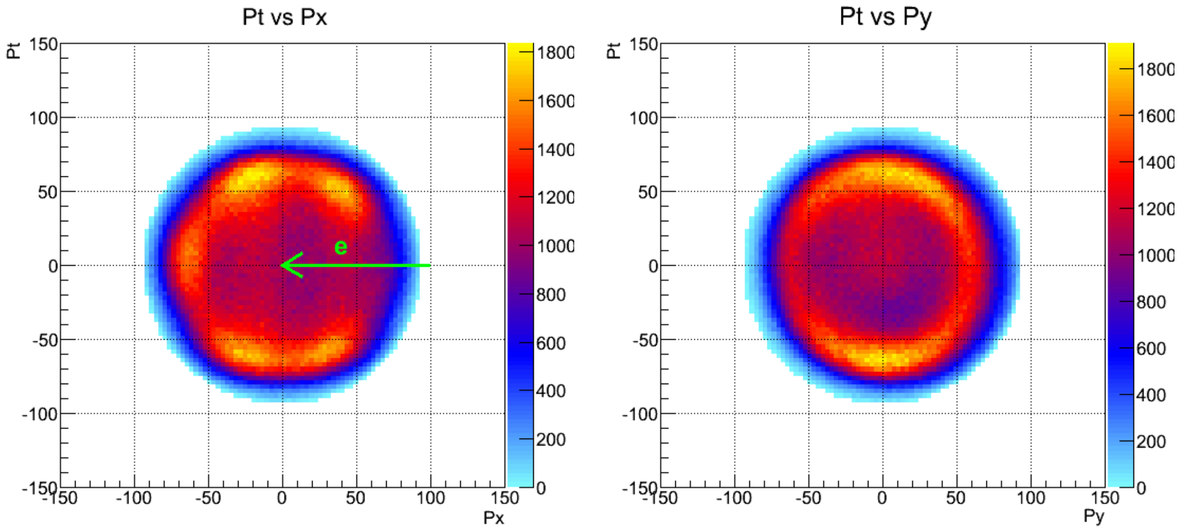
Pt vs Px

Pt vs Py

Figure 4.6: The green arrow in the left figure shows the direction of the electron beam. In the right figure, the electron beam goes into the page.

projection a third undistinguishable dimension onto the surface. Some experiments, such as the velocity slice imaging (VSI) experiment used in Ómarsson's papers, are designed around exclusively capturing such a slice. In the analagous Pt-direction, VSI experiments collect data for a fixed ΔTOF. These correspond to fixed-width slices of the Newton sphere. Often, due to the cylindrical symmetry of the experiment, such a slice is sufficient to capture the angular character of the data. However, a fixed-width slice of a Newton sphere captures a disproportionate amount of low KER particles. A low KER Newton sphere has a smaller radius in momentum space than a high KER Newton sphere. Capturing a fixed-thickness slice of a Newton sphere's cross section collects a larger solid angle of low KER Newton sphere's data. An illustration of this effect is shown in 4.7.

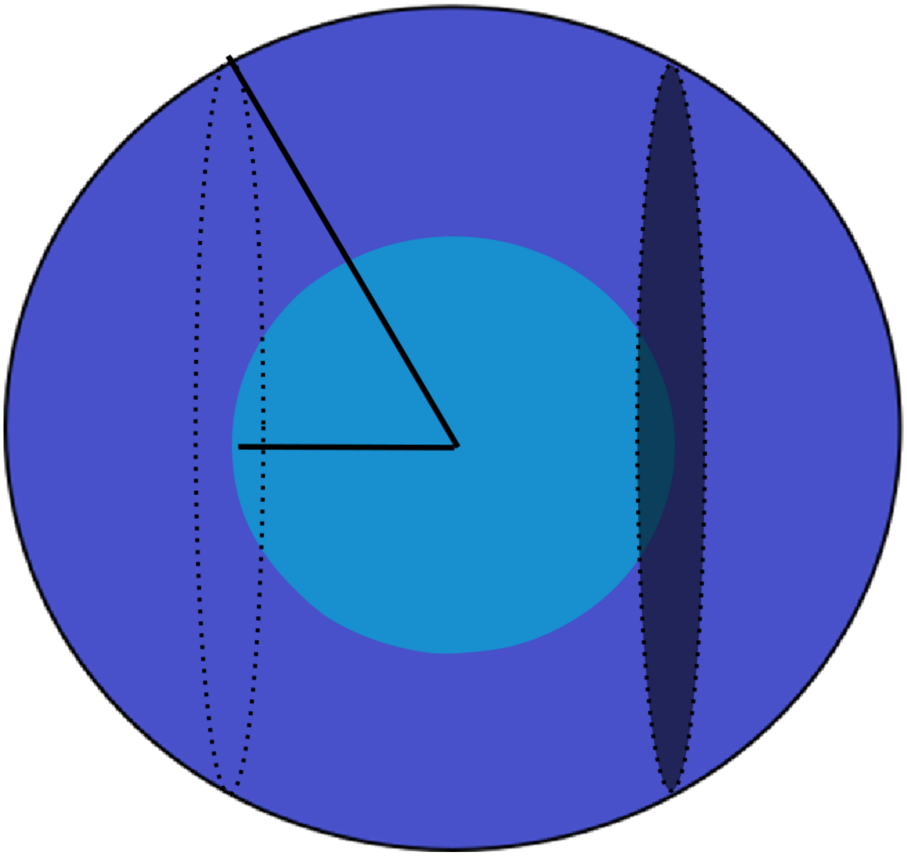

Figure 4.7: The full solid angle distribution of the inner sphere (light blue) will be collected for a fixed width slice, while only a fraction of the outer sphere (dark blue) would be collected.

COLTRIMS experiments do not have this limitation - fully resolved 3D momenta can be sliced and gated in a solid-angle preserving fashion. Two such gates are called collar gates and cone gates. Collar and cone gates slice data within a fixed angular distance from a given plane or axis', respectively (figure 4.8).

In the case of the CF_3^- data, a 5^o collar gate around the Pt-Px plane gave the cleanest density plot of the momentum distribution. The Pt vs Px density plot from

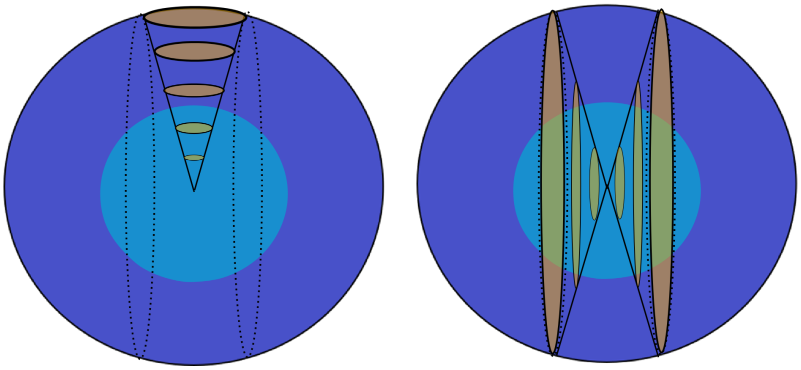

Figure 4.8: Cone gates (left) and collar gates (right) preserve the angular character of Newton spheres with different KERs.

4.6 is reproduced with this collar gate in figure 4.9 as an example. The image is further cleaned via background suppression for clarity.

From figure 4.9, the momentum distribution is two ”rings” of ions around $\sim 70^o$ and $\sim 120^o$ from the direction of the electron beam, as well as a bright feature for ions in the direction of the beam. Due to the cylindrical symmetry of the system, a one dimensional representation of the angular distribution is sufficient for investigation of its nature. The one dimensional distribution for an incident electron energy of 8eV is shown in 4.10.

A qualitative discussion of the angular distribution suggests that the attachment cross section that leads to $F + CF_3^-$ is very large when the electron is incident along a $C - F$ bond, causing that bond to break and leading to a peak in the angular distribution at 0^o. For the opposite case, when a $C - F$ bond is coaxial with the electron beam but is on the far side of the molecule from the approaching electron, the coaxial $C - F$ bond is unlikely to break. For either case, the non-coaxial $C - F$ bonds may break, causing peaks at 71^o and 109^o. The other cylindrically symmetric

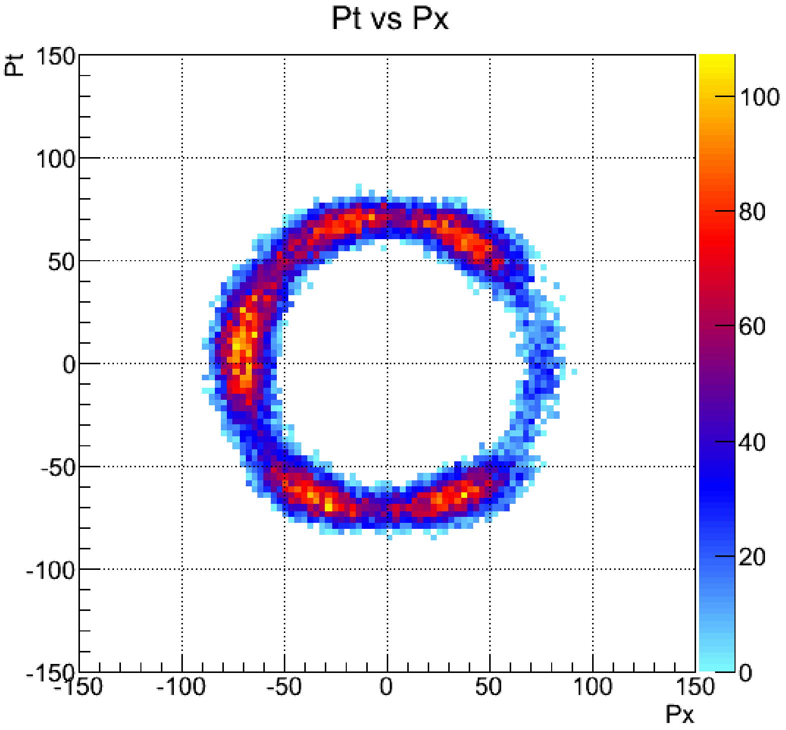

Figure 4.9: Application of a collar gate and background suppression significantly cleans the density plot to aid in visual appraisal.

orientation of the molecule is one where the incident electron approaches the molecule between two $C-F$ bonds, at 54.5^o from both. In such a case, breaking of the $C-F$ bonds can lead to ions at 54.5^o and 125.5^o. Each of these cases is illustrated in figures 4.11.

This qualitative discussion requires the transient CF_4^- ion to maintain it's T_d symmetry throughout the dissociation process, i.e., that it occurs in the axial recoil approximation. If the JTE occurs, the transient ion may instead be found in a C_{3v} symmetry wherein one of the $C-F$ bonds has been shortened or elongated. For each of the cylindrically symmetrical attachment geometries, such a change in symmetry

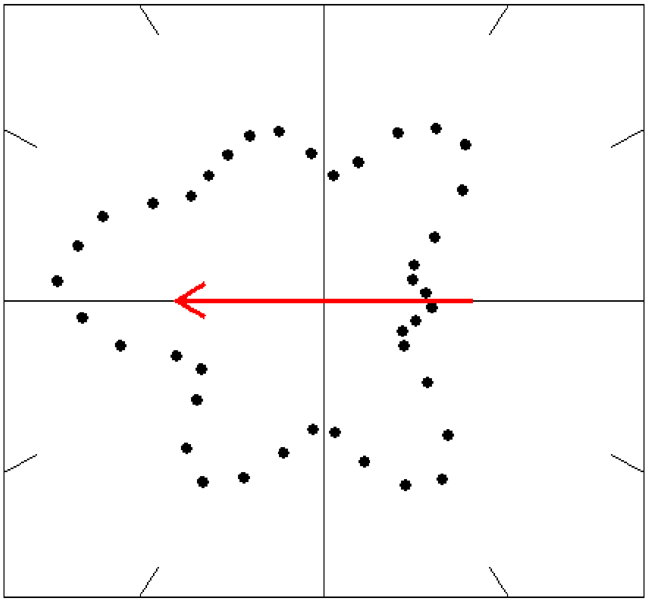

Figure 4.10: Angular Distribution of CF_3^- ions for an 8eV incident electron. The electron direction is shown by a red arrow.

would have a different effect depending on whether or not the primary C_{3v} axis was the one breaking or not. Ómarsson speculates in [18] that the Jahn-Teller Effect may play a role in DEA to CF_4. They fit their angular distributions with a mixture of T_d and C_{3v} symmetries for the CF_4^- ion, with an improvement to the error in the fit.

The 1D angular distributions for 5.5 and 8.5 eV incident electron energy are shown in figure 4.12 with the data from [18]. The Auburn experiment has more noise for the low KER data, which has been attributed to a large chamber background and reduced electron gun energy resolution for energies below 6 eV. It is clear in the figure for 8.5 eV, however, that the distributions have distinctly different features.

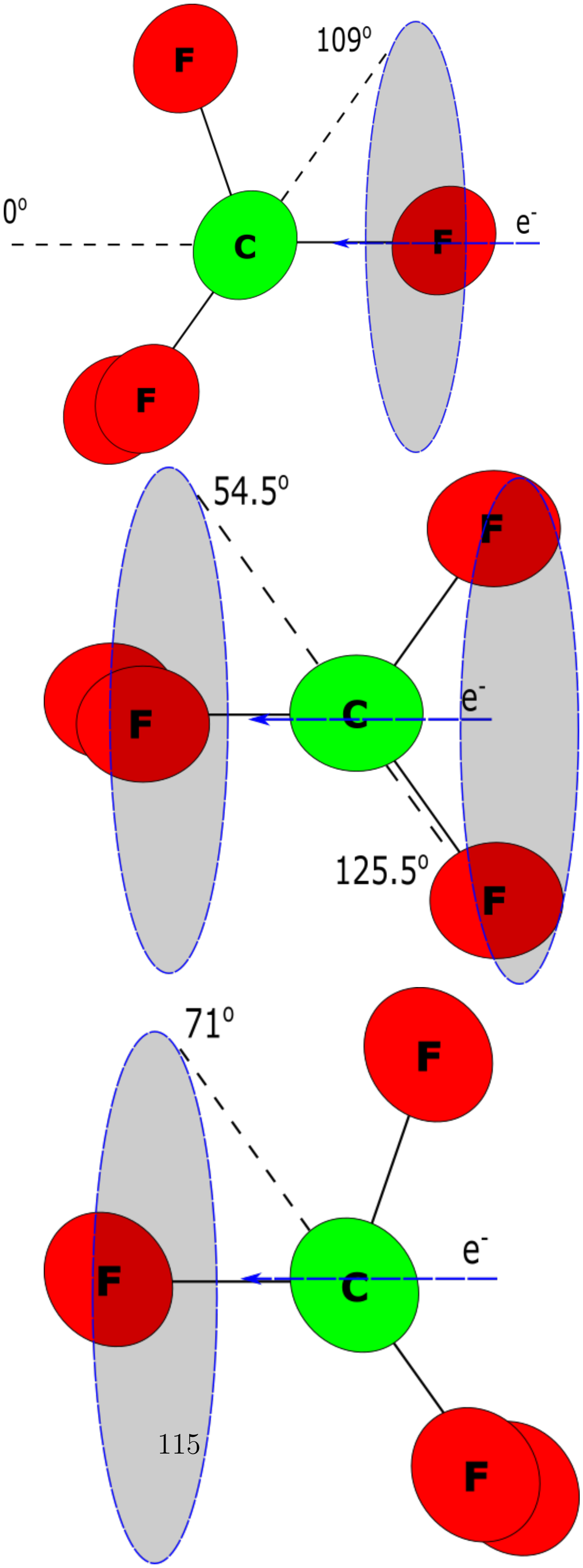

Figure 4.11: Qualitative diagram showing the orientation of the molecule for cylindrically symmetric attachment orientations. Attachment along a $C-F$ bond (left), between adjacent $C-F$ bonds (center), and opposite a $C-F$ bond (right).

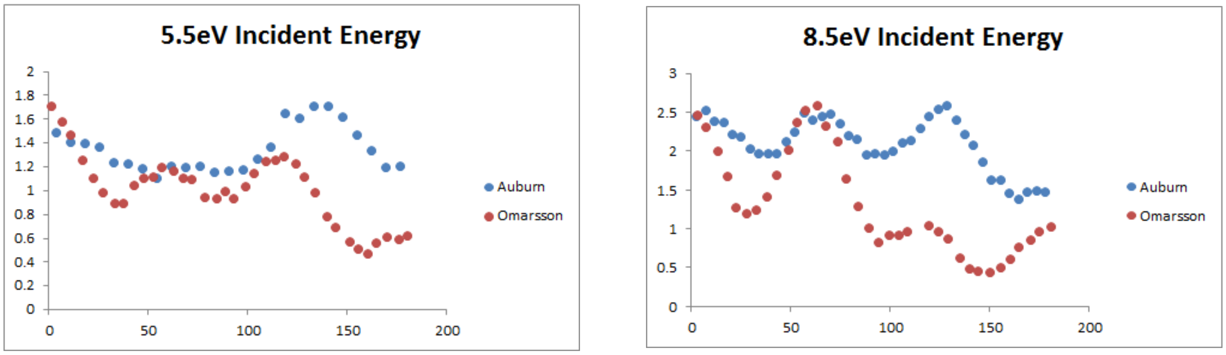

Figure 4.12: Distribution comparisons for 5.5 eV (left) and 8.5 eV (right) incident electron energies.

Both the relative peak heights and the angular values of the maxima differ. Figures 4.13 show the density plots for 5.5 and 8.5 eV momentum distributions.

In making an effort to repeat the results from Ómarsson, attachment amplitudes for the Auburn data were fit using the T_2 and C_{3v} basis functions that Ómarsson used. The fits for Auburn's data (figure 4.14) are excellent, as was the case for Ómarsson. Figure 4.12 shows that the distributions are quite different in character, yet the fitting procedure was highly successful for both distributions.

It is well within the realm of possibility that the expansion of the basis functions, i.e., inclusion of the C_{3v} basis functions, has caused the partial wave analysis to over fit the system. Any overly specified basis can fit a data set perfectly, without bringing any predictive power to the physical system. As an egregious example, fitting an angular distribution with fifty polynomial terms would match extremely well, but would give the physicist no insights into the mechanics at work.

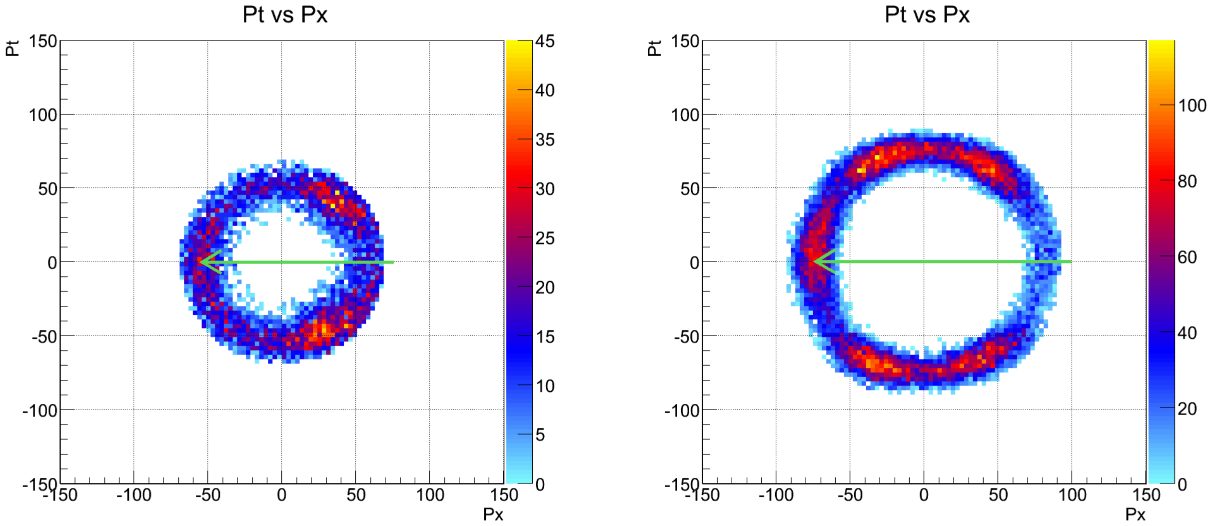

Figure 4.13: CF_3^- momentum density plots for 5.5 eV (left) and 8.5 eV (right) incident electron energies.

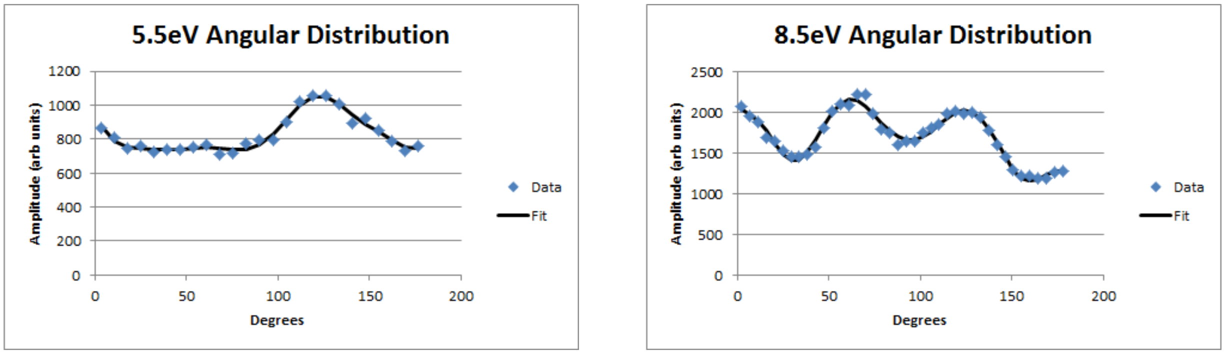

Figure 4.14: CF_3^- attachment amplitude fits using T_2 and C_{3v} basis functions in partial wave analysis.

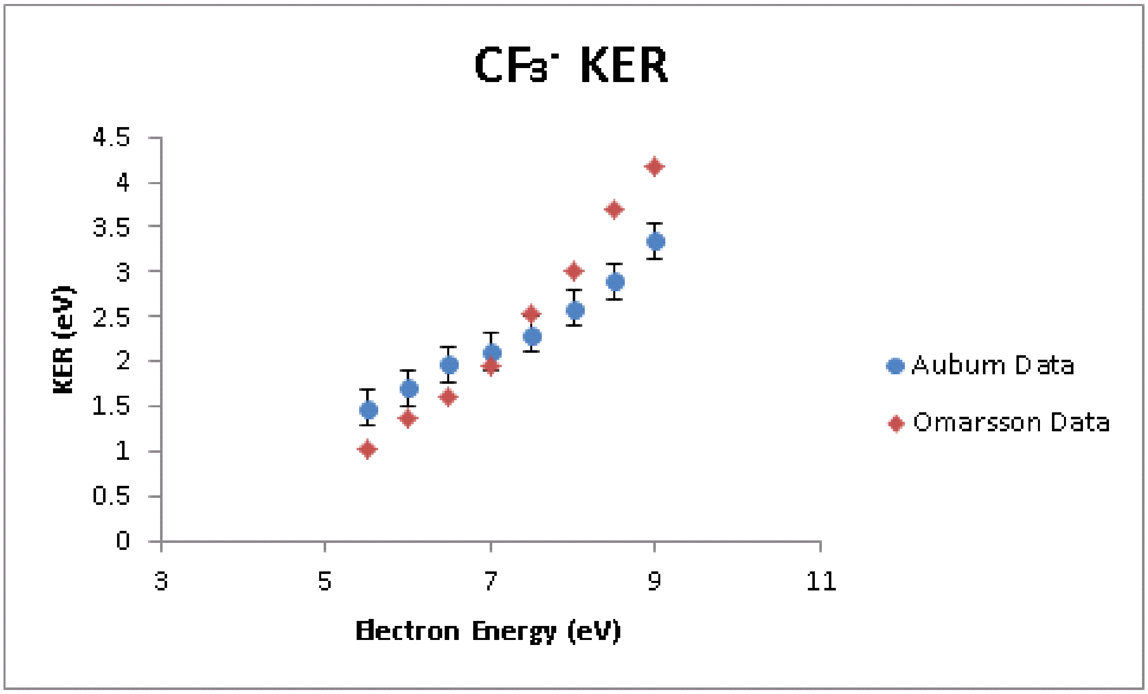

Figure 4.15: KER as a function of incident electron energy for both the experiments at Auburn and from Ómarsson *et al.*

4.3.2 Kinetic Energy Release

The final step in the comparative analysis for DEA to CF_4 was to consider the KER generated by DEA for different electron energies. These data, along with those of Ómarsson, are shown in figure 4.15.

The unique signature of the Ómarsson data, the abrupt slope change near 7 eV electron energy, is not apparent in Auburn's KER values. This supports the conclusion that mixing C_{3v} basis functions for the partial wave analysis as a way to explain the KER slope change may be erroneous. The Auburn group chooses not to speculate about the cause of the abrupt slope change in Ómarsson's data.

4.4 Analysis Summary

Among the tasks of the modern scientific endeavor, the primacy of reproducibility of results cannot be denied. As exciting as new data can be in driving scientists curiosity and capacity to predict the behavior of natural systems, those data must be reproducible to be valid. Otherwise, any model based on such data will fail and, as an obvious consequence, will be unusable. The Auburn DEA lab attempted to reproduce exotic data on dissociative electron attachment to CF_4, with mixed results. The angular distributions appear similar in density plots, though the relative peak heights and locations do not match well. The fitting procedure explaining these distributions may well be over-specified. Finally, the kinetic energy distributions of the challenged experiment and those of Auburn's data do not agree. Further research with ever-more refined techniques should continue to scrutinize this highly complex system to improve understanding.

Chapter 5

Summary

5.1 Water Experiment

Research into the dissociation dynamics of the water molecule has steadily moved forward over the last 40+ years. Early efforts using PIPICO-TOF spectrometry found the direct threshold to be very nearly 39 eV. Several experiments revealed that indirect, adiabatic double photoionization was possible well below the vertical limit of 39 eV. Beyond the vertical threshold, however, this indirect process does not take place. Several low lying excited dication curves were found above the vertical threshold, and repeated *ab initio* calculations performed by numerous research groups found curves extending above the vertical threshold to nearly 50 eV above the water neutral ground state.

As experimental and theoretical techniques progressed, these excited dication potentials were calculated and measured with increasing precision. Repulsive potential curves have been calculated for both the two- and three-body reaction pathways, as well as the angular character of the three-body channel. For the first time in this thesis, the decay of the dication has been measured with three dimensional momentum spectroscopy using the COLTRIMS technique. Capturing two charged recoil ion particles, in either the two- or three-body channels, leads to a complete measurement of the system via conservation of momentum. Measurement of the complete kinetic energy release, the electron energy plus recoil ion kinetic energy, identified the asymptotic final states of the three-body breakup as the ^3P, ^1D, and ^1S terms of the Oxygen neutral fragment and of course, in each case, two free protons.

Using the final oxygen states as a coarse gate to limit the number of initial dication states, investigation of the individual KERs and bond angles allowed eight of the nine energetically available dication states to be identified in the data. The ninth state, the lowest lying $^1A_1$, was not observed in the three-body channel.

Investigation of the two-body channel was unable to clearly resolve dication states; this is due to the final state energy partitioning being obfuscated within the OH^+ molecule. Investigation of the electron energy partitioning found that in the asymmetric stretching regime that leads to the two-body breakup follows both the "knock-out" and "shake-out" pictures of double photoionization. Certain as yet unidentified dication states lead to highly asymmetric electron energy sharing, while others lead to symmetric energy sharing. Further investigation of the electron angular correlations, with perhaps fewer accessible dication curves available, is in order.

5.2 CF$_4$ Experiment

The primary motivation of the CF_4 DEA experiment was to perform a check on exotic results offered by another research group. In particular, the shift in the KER vs electron energy measured by Ómarsson *et al* near 7 eV electron energy. Ómarsson attributed this shift to a mixing of T_d and C_{3v} symmetries in the transient CF_4^- ion, motivated by the presence of the JTE. While the explanation offered by Ómarsson was compelling, the results were not replicated in the Auburn data. Auburn's angular distributions for the CF_3^- channel differed from those of Ómarsson in relative peak height and, perhaps, in peak location. Despite these differences, both data were well fit using a mixture of symmetry states for partial wave analysis. It is possible that the mixing of these many basis functions does not serve any predictive function but, instead, merely serves to over fit the data, producing a reliable fit regardless of the physical mechanisms causing the distribution. The Auburn data did not find any significant change in the KER response to incident electron energy either, instead finding agreement with previous experiments measuring the DEA process. There is no compelling evidence in the Auburn data for such a curve change to be considered a new normal, but neither is there a clear explanation that would dismiss the results of Ómarsson as a non-physical error.

Appendix A

Appendix A - Quantum Chemistry and Group Theory

A.1 Molecular Orbitals and Symmetry

In this section, a brief description of Molecular Orbitals and symmetry will be given. Molecular orbitals form the electronic structure of molecules. This structure is the primary physical property probed by incident particles: photons in the water experiment, and electrons in the CF_4 experiment. Significant insight into these topics was given by conversations by the Berkeley theory group and the excellent text by Haken and Wolf, *Molecular Physics and Elements of Quantum Chemistry* [20]

A.1.1 Molecular Orbitals

In general, the orbitals of molecular systems are more complex than their atomic cousins. The entirely non-Coulombic potential created by multiple nuclei and th eir electrons requires its own treatment in understanding the electronic structure of molecules. In a simple picture, the molecular electron save functions are constructed by a linear combination of atomic orbitals (LCAO):

$$\Psi = \sum_j c_j \phi_j \tag{A.1}$$

Here, Ψ represent molecular orbital wave functions, ϕ_j the atomic wavefunctions, and coefficients c_j that are determined via the variational principle:

$$Minimize: \; frac\int \Psi^* H \Psi dV \int \Psi^* \Psi dV \tag{A.2}$$

Under the assumption that phi_j are orthogonal, the combination of these equations yields:

$$\sum_j (H_{ij} - E_\alpha \delta_{ij}) C_j^{(\alpha)} \;=\; 0 \tag{A.3}$$

Where α is the parameter to be varied in minimizing the variational integral A.2. These equations are, in general, complex. The problem can be simplified greatly by employing **group theory** to reduce the number of atomic orbitals considered in construction of the molecular orbitals A.1.

A.1.2 Group Theory

Symmetry Group theory is, in the simplest of terms, the mathematics of symmetry. Any collection of objects can be classified by their symmetry operations. As an example, consider an equilateral triangle:

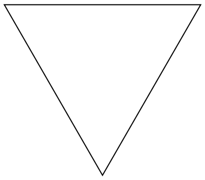

A counterclockwise rotation of such an objection around its center point by 120^o leaves it unchanged, that is:

$$R_{120^o} A = A \tag{A.4}$$

Likewise for integer multiples of R, as well as reversing the direction of the rotation. The triangle also has mirror planes, about which reflections yield no change in the object. A symmetry operation *not* possessed by the equilateral triangle is, e.g., the inversion operation, which maps coordinates through the origin:

$$I\ F(x, y, z) \ = \ F(-x, -y, -z) \tag{A.5}$$

A fully rigorous and in depth discussion is well beyond the scope of this appendix. It should suffice to say, however, that geometrical objects possess inherent symmetries, and these symmetries are described by symmetry operations.

Application to Molecular Physics Group theory helps determine the coefficients used in LCAO construction of molecular orbitals A.1 by significantly reducing the number of terms, or by outright prescribing their forms. If a molecule possesses a rotational symmetry, the electronic wave functions must also possess this rotational symmetry. In order to proceed to a relevant example, the follow terms are defined:

- Symmetry Group: A symmetry group describes which symmetry operations an object has. For example, the NH_3 molecule possesses C_{3v} symmetry. The notation C_{nv} describes an object with an n-fold rotational axis and n mirror planes that contain the C_n axis. Rotations of $\frac{360^o}{n}$ leave the object unchanged.

- Symmetry element: The operations contained in a symmetry group are referred to as *elements*. Examples of elements are inversion centers, reflection planes, rotation axis, etc.

- Group Multiplication Table: The list of symmetry elements, and how they interact, are summarized in a group multiplication table:

Table A.1: Group Multiplication Table for C_{3v}

C_{3v}	E	C_3^+	C_3^-	σ_v	$\sigma_v^{'}$	$\sigma_v^{''}$
E	E	C_3^+	C_3^-	σ_v	$\sigma_v^{'}$	$\sigma_v^{''}$
C_3^+	C_3^+	C_3^-	E	$\sigma_v^{'}$	$\sigma_v^{''}$	σ_v
C_3^-	C_3^-	E	C_3^+	$\sigma_v^{''}$	σ_v	$\sigma_v^{'}$
σ_v	σ_v	$\sigma_v^{''}$	$\sigma_v^{'}$	E	C_3^-	C_3^+
$\sigma_v^{'}$	$\sigma_v^{'}$	σ_v	$\sigma_v^{''}$	C_3^+	E	C_3^-
$\sigma_v^{''}$	$\sigma_v^{''}$	$\sigma_v^{'}$	σ_v	C_3^-	C_3^+	E

where $C_3^{\pm}$ corresponds to CCW/CW rotations and σ_v^a to mirror planes, while E is the identity operator, which leaves all objects unchanged.

- Class: Two elements in a group are called conjugates of one another if there exists an element C within the group such that:

$$B = CAC^{-1} \tag{A.6}$$

This relationship, in terms of matrices, is a similarity transformation. A class is all elements in a group which are conjugate with each other. For the C_{3v} example, consider the element σ_v. Checking the multiplication table to procede:

$$C_3^{-1}\sigma_v C_3 \;=\; C_3^{-1}\sigma_v^{'} \;=\; C_3^2\sigma_v^{'} \;=\; \sigma_v^{''} \qquad \text{(A.7)}$$

Repeating this process for all the elements in the group shows that $(\sigma_v, \sigma_v^{'}, \sigma_v^{''})$ and (C_c^+, C_c^-) belong to classes. The number of elements in a class is called its order.

- Character: The character of a representation is the trace of its matrix form. The characters of different symmetry elements form a character table, which summarizes the elements behavior within the group. The character table representing all elements is, in general, reducible; that is, it contains redundant information. Reduction of a character table to an irreducible representation involves grouping together elements in classes. These classes, then, form a basis set that define group symmetry operations. For C_{3v}, the table appears as:

Table A.2: Character Table for C_{3v}

C_{3v}	E	$2C_3$	$3\sigma_v$	Operation	
A_1	1	1	1	z	x^2+y^2, z^2
A_2	1	1	-1	R_z	
E	2	-1	0	$(x,y)(R_x,R_y)$	$(x^2-y^2,xy)(xz,yz)$

This character table includes conventions introduced by Robert Mullikan. The first column after the classes lists the coordinates that display a particular symmetry behavior. For example, the z position coordinate is said to possess A_1 symmetry, or z "transforms as" A_1. The last column gives quadratic terms that follow a given symmetry behavior.

Example: Determining Molecular Orbitals for Water Water possesses C_{2v} symmetry. It's character table is:

Table A.3: Character Table for C_{2v}

C_{2v}	E	C_2	σ_v	$\sigma_v^{'}$	Operation	
A_1	1	1	1	1	z	x^2, y^2, z^2
A_2	1	1	-1	-1	R_z	xy
B_1	1	-1	1	-1	x, R_y	yz
B_2	1	-1	-1	1	y, R_x	xz

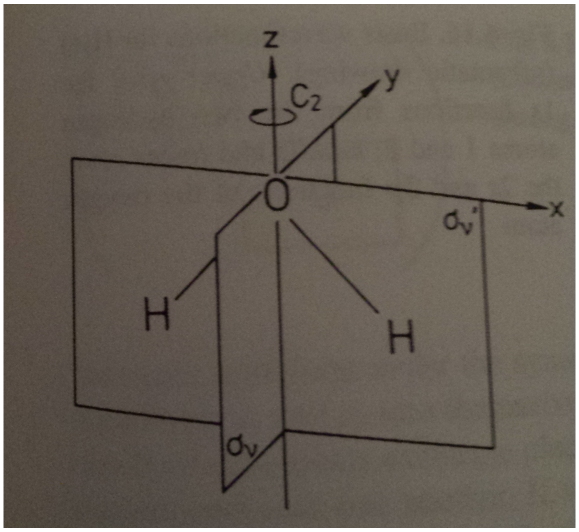

Figure A.1: C_{2v} coordinate system with the symmetry elements. Image borrowed from [20]

The $\sigma_v^{'}$ mirror plane is coplanar with the molecule. As an example of the use of the table, an x coordinate changes signs in the following way:

$$Ex \ = x \ , \ C_2 x \ = \ -x \ , \ \sigma_v x \ = \ x \ , \ \sigma_v^{'} x \ = \ -x \qquad (A.8)$$

x therefor transforms as B_1, as seen in the character table.

Returning to the problem at hand, the next step is to determine the atomic orbitals that should be used as a basis for the molecular orbitals in equation A.1. Only valence electrons contribute in a significant way to bonding, so core electrons are excluded from consideration. The hydrogen atoms each contribute 1s electrons. The valence shell of oxygen contributes two 2s electrons and four 2p electrons. The basis, then, is:

$$\phi_j = (s_1, s_2, 2s, 2px, 2py, 2pz) \tag{A.9}$$

Where $s_{1,2}$ represent the two individual hydrogen electrons. How do the hydrogen wavefunctions respond to the symmetry operations of C_{2v}?

$$E \begin{pmatrix} s_1 \\ s_2 \end{pmatrix} = \begin{pmatrix} 1 & 0 \\ 0 & 1 \end{pmatrix} \begin{pmatrix} s_1 \\ s_2 \end{pmatrix} = \begin{pmatrix} s_1 \\ s_2 \end{pmatrix} \tag{A.10}$$

$$C_2 \begin{pmatrix} s_1 \\ s_2 \end{pmatrix} = \begin{pmatrix} 0 & 1 \\ 1 & 0 \end{pmatrix} \begin{pmatrix} s_1 \\ s_2 \end{pmatrix} = \begin{pmatrix} s_2 \\ s_1 \end{pmatrix} \tag{A.11}$$

$$\sigma_v \begin{pmatrix} s_1 \\ s_2 \end{pmatrix} = \begin{pmatrix} 0 & 1 \\ 1 & 0 \end{pmatrix} \begin{pmatrix} s_1 \\ s_2 \end{pmatrix} = \begin{pmatrix} s_2 \\ s_1 \end{pmatrix} \tag{A.12}$$

$$\sigma_v^{'} \begin{pmatrix} s_1 \\ s_2 \end{pmatrix} = \begin{pmatrix} 1 & 0 \\ 0 & 1 \end{pmatrix} \begin{pmatrix} s_1 \\ s_2 \end{pmatrix} = \begin{pmatrix} s_1 \\ s_2 \end{pmatrix} \tag{A.13}$$

The characters of these operations, i.e. their traces, are:

Table A.4: Character Table for C_{3v} Trace

C_{2v}	E	C_2	σ_v	σ_v
$2H(1s)$	2	0	0	2

Consulting the irreducible representations of C_{2v} in A.3, it is clear that the 2H(1s) orbitals correspond to $A_1 + B_2$:

Table A.5: Representations of 2H(1s)

A_1	1	1	1	1
B_2	1	-1	-1	1
$2H(1s)$	2	0	0	2

The next task is to project the 2H(1s) wave functions onto the irreducible representations of the group. This is done with a projection operator P:

$$P_i \;=\; \frac{1}{h}\sum_R \chi_i(R^{-1})\hat{R} \tag{A.14}$$

where h denotes the order of the group, R are the operations, χ_i is the character of the ith representation of the group, and $\hat{R}$ is the matrix corresponding to the group operation. For example, the projection operator P_{A_1} is given by:

$$P_{A_1} \;= \frac{1}{4}(1 \cdot E \;+\; 1 \cdot C_2 \;+\; 1 \cdot \sigma_v \;+\; 1 \cdot \sigma_v^{'}) \;=\; \frac{1}{2}\begin{pmatrix} 1 & 1 \\ 1 & 1 \end{pmatrix} \tag{A.15}$$

For B_2, the projection yields:

$$P_{B_2} = \frac{1}{2}\begin{pmatrix} 1 & -1 \\ -1 & 1 \end{pmatrix} \tag{A.16}$$

Applying each operator to the original basis $\begin{pmatrix} s_1 \\ s_2 \end{pmatrix}$ yields:

$$P_{A_1}\begin{pmatrix} s_1 \\ s_2 \end{pmatrix} = \frac{1}{2}\begin{pmatrix} 1 & 1 \\ 1 & 1 \end{pmatrix}\begin{pmatrix} s_1 \\ s_2 \end{pmatrix} = \frac{1}{2}(s_1 + s_2) \tag{A.17}$$

$$P_{B_2}\begin{pmatrix} s_1 \\ s_2 \end{pmatrix} = \frac{1}{2}\begin{pmatrix} 1 & -1 \\ -1 & 1 \end{pmatrix}\begin{pmatrix} s_1 \\ s_2 \end{pmatrix} = \frac{1}{2}(s_1 - s_2) \tag{A.18}$$

Next, the atomic orbitals of water are given a similar treatment. The projection process is identical to that of the 2H(1s) orbitals, and is skipped for brevity. The resulting categorization of each orbital in the irreducible representations is:

Table A.6: Atomic Orbitals in Irreducible Representations

	O Orbitals	H Orbitals
A_1	2s,$2p_z$	$\frac{1}{2}(s_1 + s_2)$
A_2	–	–
B_1	$2p_y$	–
B_2	$2p_x$	$\frac{1}{2}(s_1 - s_2)$

From the original atomic orbital basis $(s_1, s_2, 2s, 2p_x, 2p_y, 2p_z)$, the new atomic orbital basis $(\frac{1}{2}(s_1+s_2), \frac{1}{2}(s_1-s_2), 2s, 2p_x, 2p_y, 2p_z)$ is formed. Now the LCAO process of equation A.1 can be approached using the confined parameter space of group theory. For example, the B_1 irreducible representation suggests that the molecular wavefunction is:

$$\Psi \;=\; c\, p_y \tag{A.19}$$

Such an orbital is clearly non-bonding, as it excludes the hydrogen electrons entirely. For B_2, there is:

$$\Psi \;=\; c_1 p_x \;+\; c_2 \frac{1}{2}(s_1 - s_2) \tag{A.20}$$

In both cases, group theory has significantly reduced the complexity of determining the molecular orbitals. Once they are found, their coefficients are produced by solving equation A.2. The eigenenergies can then be calculated, informing which molecular orbitals are bonding, non-bonding, and antibonding. An energy diagram summarizing the molecular orbital construction concludes the appendix:

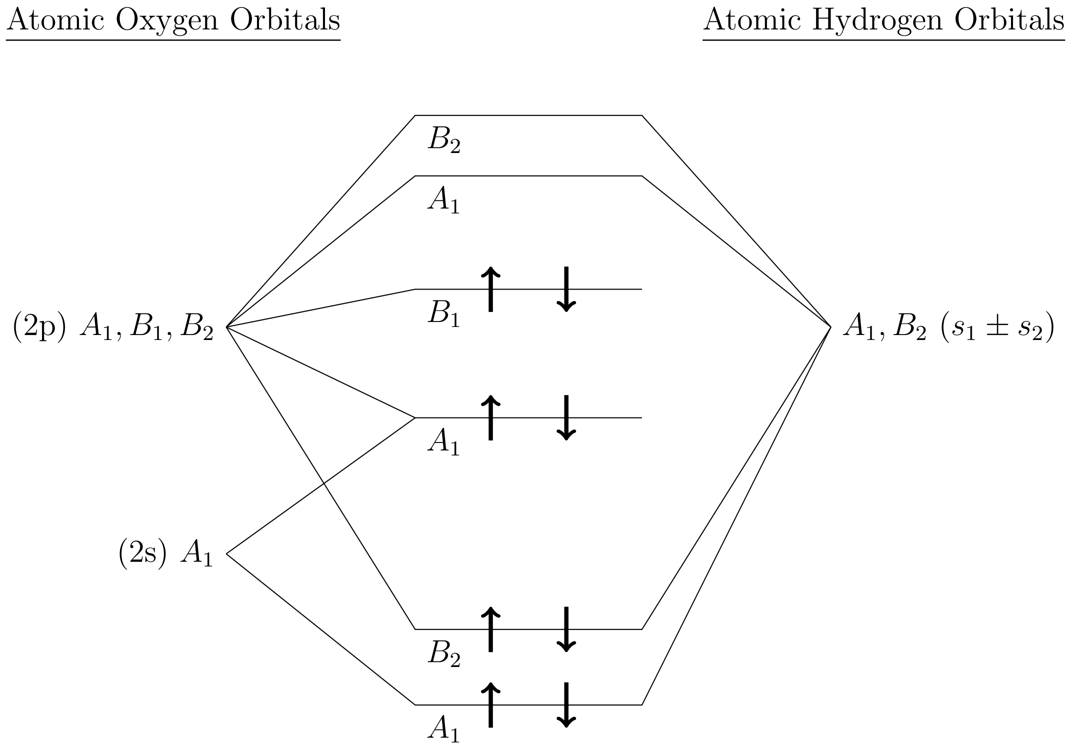
Atomic Oxygen Orbitals
Atomic Hydrogen Orbitals
B_2
A_1
B_1
(2p) A_1, B_1, B_2
A_1, B_2 $(s_1 \pm s_2)$
A_1
(2s) A_1
B_2
A_1

Appendix B

Appendix B - Code Samples

B.1 Molecular Frame Definition

The LMF2ROOT analysis framework contains super objects called, appropriately, Ueberstructs. These super objects contain all of the relevant information for a given event - times, spectrometer settings, positions, and so on. Contained within the Ueberstructs is 3D vector used to store vector information, called CH_Vector (ColaHell Vector). The CH_Vector objects can be used to define anything, including randomizing the first and second hits to eliminate experimental bias or definition of the molecular frame.

```

bool random_particle = rand()%2;
bool random_pol = rand()%2;

CH_vector a_ion;
CH_vector b_ion;
CH_vector pol;

//randomize ions for creation of molecular frame
if(random_particle){
        a_ion= CH_vector(r[0]->phy->mom.x, r[0]->phy->mom.y, r[0]->phy->mom.z);
        b_ion= CH_vector(r[1]->phy->mom.x, r[1]->phy->mom.y, r[1]->phy->mom.z);
}else{
        a_ion= CH_vector(r[1]->phy->mom.x, r[1]->phy->mom.y, r[1]->phy->mom.z);
        b_ion= CH_vector(r[0]->phy->mom.x, r[0]->phy->mom.y, r[0]->phy->mom.z);
}

if(random_pol){
        pol=CH_vector(0,0,1);
}else{
```

```
        pol=CH_vector(0,0,-1);
}

CH_vector sumab=(a_ion.Norm()+b_ion.Norm()).Norm();

//molecular frame coordinate system
Coordinate_System mf = Coordinate_System(a_ion.Norm()+b_ion.Norm(), a_ion.Norm()-b_ion.Norm());

bool random_electron = rand()%2;

CH_vector e1p_mf;
CH_vector e2p_mf;

//randomize electrons for projection into molecular frame
if(random_electron){
        e1p_mf=mf.project_vector(e[0]->phy->mom);
        e2p_mf=mf.project_vector(e[1]->phy->mom);
        }
else{
        e1p_mf=mf.project_vector(e[1]->phy->mom);
        e2p_mf=mf.project_vector(e[0]->phy->mom);
        }

//project ions and polarization axis into molecular frame
CH_vector r1p_mf=mf.project_vector(a_ion);
CH_vector r2p_mf=mf.project_vector(b_ion);
CH_vector pol_molframe = mf.project_vector(pol);

CH_vector oxygenInMolFrame(-(r1p_mf.x + r2p_mf.x),-(r1p_mf.y + r2p_mf.y),-(r1p_mf.z + r2p_mf.z));

double oxygen_px = -(r[0]->phy->mom.x + r[1]->phy->mom.x);
double oxygen_py = -(r[0]->phy->mom.y + r[1]->phy->mom.y);
double oxygen_pz = -(r[0]->phy->mom.z + r[1]->phy->mom.z);

double oxygen_E = (oxygenInMolFrame.Mag()*oxygenInMolFrame.Mag())/(1836.15*32*r[0]->raw->m)*27.212;

r[0]->phy->energy *= 1.17;
r[1]->phy->energy *= 1.17;
oxygen_E *= 1.17;
double KER = (r[0]->phy->energy + r[1]->phy->energy + oxygen_E);
r[0]->phy->energy *= 1.17;
r[1]->phy->energy *= 1.17;
e[0]->phy->energy *= 1.11;
e[1]->phy->energy *= 1.11;
double e_energy_total = (e[0]->phy->energy + e[1]->phy->energy);

double ratio = e[random_electron]->phy->energy/e_energy_total;
```

```
double bondAngle = r1p_mf.Angle_deg(r2p_mf);
double totalE = e_energy_total + KER;

double distance = sqrt((e[1]->raw->data.x - e[0]->raw->data.x)*(e[1]->raw->data.x - e[0]->raw->data.x) +
        (e[1]->raw->data.y - e[0]->raw->data.y)*(e[1]->raw->data.y - e[0]->raw->data.y));
```

B.2 Water Gating

All of the gates used to isolate different initial dication states are logical boolean gates based on some measureable quantity such as energy or angle. Some examples are given below.

Uneven energy sharing between electrons for the two body breakup:

```
if ((e[!random_electron]->phy->energy/e_energy_total < .05)
```

Separating three body breakup data by the final total energy

```
double TEGate[3] = {false, false, false};

if ((totalE < 21.)
        && (totalE > 20.)){
        TEGate[0] = true;} // 3P State

if ((totalE < 19.)
        && (totalE > 18.)){
        TEGate[1] = true;} // 1D State

if ((totalE < 17.)
        && (totalE > 16.)){
        TEGate[2] = true;} // 1S State
```

Further separation of three body breakup data by total KER

```
double dicationGate[8] = {false,false,false,false,false,false,false,false};
        //Approximately Ascending Energy, but grouped by oxygen term
        //1D from 1B1
        if(TEGate[1]
        &&(KER > 3.0)
        &&(KER < 5.0))
        {dicationGate[0] = true;}

        //1D from 1A2
        if(TEGate[1]
        &&(KER > 6.5)
        &&(KER < 8.5))
        {dicationGate[1] = true;}

        //1D from 1A1
        if(TEGate[1]
        &&(KER > 6.8)
        &&(KER < 8.8))
        {dicationGate[2] = true;}

        //1D from 1B2
        if(TEGate[1]
        &&(KER > 8.7)
        &&(KER < 10.7))
        {dicationGate[3] = true;}

        //3P from 3B1
        if(TEGate[0]
        &&(KER > 3.0)
        &&(KER < 5.0))
        {dicationGate[4] = true;}

        //3P from 3A2
        if(TEGate[0]
        &&(KER > 7.0)
        &&(KER < 9.0))
        {dicationGate[5] = true;}

        //3P from 3B2
        if(TEGate[0]
        &&(KER > 8.5)
        &&(KER < 10.5))
        {dicationGate[6] = true;}

        //1S from 1A1
        if(TEGate[2]
        &&(KER > 11.0)
```

```
        &&(KER < 13.0))
        {dicationGate[7] = true;}
```

B.3 CF_3^- Analysis

The CF_3^- analysis consists of defining physical quantities of interest, such as energy and momentum, and calculating those values either via basic physical equations or via simulation fits. Those data are then gated using boolean logic to produce the desired plots.

```
        double tofF[2] = {4300, 5600};
        bool fragmentF = ((r1tof < tofF[1]) && (r1tof > tofF[0]));
        double tofCF3[2] = {17000,25000};
        bool fragmentCF3 = ((r1tof < tofCF3[1]) && (r1tof > tofCF3[0]));
        int mass[2] = {19,69};
        double massRatio = 69./19.;
        double tofOffset = 0;
        r1tof = r1tof + tofOffset;

        int index = 2;  //used to label fragments.  value[0] is F-, value[1] is CF3-

        if(fragmentF){
                index = 0;
px[index] = (mass[index]*amu*r1x*(0.001)/(r1tof*pow(10.0,-9.0)))/SItoAUmom;
py[index] = (mass[index]*amu*r1y*(0.001)/(r1tof*pow(10.0,-9.0)))/SItoAUmom;
pt[index] = 1376.486220403173 - 0.5001535796096956*r1tof + 0.000056998175850975*Power(r1tof,2) -
2.4891900890560533e-9*Power(r1tof,3);
KE[index] = (px[index]*px[index] + py[index]*py[index] + pt[index]*pt[index])*27.211/(2*mass[index]*1836.152672);
KER[index] = KE[index] *(1 + (1/massRatio));
pmag[index] = sqrt(px[index]*px[index]+ py[index]*py[index] + pt[index]*pt[index]);
pr[index] = pmag[index];
pphi[index] = atan2(pt[index], px[index]);
ptheta[index] = acos(py[index]/pr[index]);
        }

        if(fragmentCF3){
                index = 1;
px[index] = (mass[index]*amu*r1x*(0.001)/(r1tof*pow(10.0,-9.0)))/SItoAUmom;
py[index] = (mass[index]*amu*r1y*(0.001)/(r1tof*pow(10.0,-9.0)))/SItoAUmom;
pt[index] = 1669.6323230326143 - 0.15983516732773959*r1tof + 5.040328389257488e-6*Power(r1tof,2) -
5.947963164635438e-11*Power(r1tof,3);
KE[index] = (px[index]*px[index] + py[index]*py[index] + pt[index]*pt[index])*27.211/(2*mass[index]*1836.152672);
```

```
KER[index] = KE[index] *(1 + massRatio);
pmag[index] = sqrt(px[index]*px[index]+ py[index]*py[index] + pt[index]*pt[index]);
pr[index] = pmag[index];
pphi[index] = atan2(pt[index], px[index]);
ptheta[index] = acos(py[index]/pr[index]);
                }
```

An example boolean logic gate follows:

```
bool yCollarSmall[2] = {((asin(py[0]/pmag[0])*180./pi < halfAngleSmall) && (asin(py[0]/pmag[0])*180./pi > -halfAngleSm
```

Bibliography

[1] P. J. Richardson, J. H. D. Eland, P.G. Fournier, D. L. Cooper. Spectrum and decay of the doubly charged water ion. *Journal of Chemical Physics*, (84):3189, 1986.

[2] D.M. Curtis, J.H.D. Eland. Coincidence studies of doubly charged ions formed by 30.4 nm photoionization. *International Journal of Mass Spectrometry and Ion Processes*, (63):241–264, 1984.

[3] D. Winkoun, G. Dujardin, L. Hellner, M. J. Besnard. One- and two-step double photoionisation processes in valence shells of H_2O. *J. Phys B: Atomic, Molecular, Optical Physics*, (21):1385, 1988.

[4] J.C. Severs, F.M. Harris, S.R. Andrews, D.E. Parry. Triplet-state energies of H_2O^{2+}: a combined experimental and theoretical study. *Chemical Physics*, (175):467–473, 1993.

[5] Timothy J. Van Huis, Steven S. Wesolowski, Yukio Yamaguchi, Henry F. Schaefer III. Scratching the surface of the water dication. *Journal of Chemical Physics*, 110(24), 1999.

[6] J.H.D. Eland. Double photoionisation spectrea of methane, ammonia and water. *Chemical Physics*, (323):391–396, 2006.

[7] B. Gervais, E. Giglio, L. Adoui, A. Cassimi, D. Duflot, and M.E. Galassi. The H_2O^{2+} potential energy surfaces dissociating into H^+/OH^+: Theoretical analysis of the isotopic effect. *Journal of Chemical Physics*, 131(024302), 2009.

[8] S.Y. Truong, A.J. Yencha, A.M. Juarez, S.J. Cavanagh, P. Bolognesi, G.C. King. Photo-double ionization of water studied by threshold photoelectrons coincidence spectroscopy. *Chemical Physics Letters*, (474):41–44, 2009.

[9] R. Dörner, V. Mergel, O. Jagutzki, L. Spielberger, J. Ullrich, R. Moshammer, H. Schmidt-Böcking. Cold target recoil ion momentum spectroscopy: a 'momentum microscope' to view atomic collision dynamics. *Physics Reports*, (330):95–192, 2000.

[10] W.C. Wiley, I.H. McLaren. Time-of-flight mass spectrometer with improved resolution. *Review of Scientific Instruments*, (26):1150, 1955.

[11] Charles F. Jackels. An ab initio potential-energy surface study of several states of the water cation. *Journal of Chemical Physics*, (72):4873, 1980.

[12] J. Colgan and M. S. Pindzola. Total and differential cross-section calculations for the double photoionization of the helium 1s2s $^{1,3}s$ states. *Physical Review A*, (67):012711, 2003.

[13] Tobias Schneider, Peter Lesnek Chocian, Jan-Michael Rost. Separation and identification of dominant mechanisms in double photoionization. *Physical Review Letters*, (89):7, 2002.

[14] P.W. Harland, J.L. Franklin. Partitioning of excess energy in dissociative resonance capture processes. *Journal of Chemical Physics*, (61):1621, 1974.

[15] G.J. Verhaart, W.J. Van Der Hart, H.H. Brongersma. Low energy electron impact on chlorofluoromethanes and cf_4: Resonances, dissociative attachment and excitation. *Chemical Physics*, (34):161–167, 1978.

[16] E. Illenberger. Measurement of the translation excess energy in dissociative electron attachment processes. *Chemical Physics Letters*, (80):1, 1980.

[17] Yvonnick Le Coat, Jean-Pierre Ziesel, Jean-Pierre Guillotin. Negative ion resonances in cf_4 probed by dissociative electron attachment. *J. Phys B: Atomic molecular Optical Physics*, (27):965, 1994.

[18] Frímann H. Ómarsson, Ewelina Szymanska, Nigel J. Mason, E. Krishnakumar, Oddur Ingólfsson. Quantum superposition of target and product states in reactive electron scattering from cf_4 revealed through velocity slice imaging. *Physical Review Letters*, (111):063201, 2013.

[19] Frímann H. Ómarsson, Ewelina Szymanska, Nigel J. Mason, E. Krishnakumar, Oddur Ingólfsson. Velocity slice imagining study on dissociative electron attachment to cf_4. *European Physical Journal D*, (68):101, 2014.

[20] H. Haken, H.C. Wolf. *Molecular Physics and Elements of Quantum Chemistry: Introduction to Experiments and Theory.* Springer, 2 edition, 2004.